BRIDGING FIELDS AND FLOODPLAINS: HYDROLOGIC CONNECTION, NITRATE REDUCTION, AND WATER STORAGE ACROSS LANDSCAPES MANAGED FOR DRYLAND CEREAL PRODUCTION IN CENTRAL MONTANA

by

Jack Willsey Poole

A thesis submitted in partial fulfillment
of the requirements for the degree

of

Master of Science

in

Land Resources and Environmental Science

MONTANA STATE UNIVERSITY
Bozeman, Montana

August 2025

©COPYRIGHT

by

Jack Willsey Poole

2025

All Rights Reserve

ACKNOWLEDGEMENTS

This research would not have been possible without funding from the USDA-ARS Agreement 58-3032-005, the Consortium for Research on Environmental Water Systems (NSF EPSCoR Cooperative Agreement OIA-1757351), the NSF Signals in the Soil Award 2034430, the Montana State University Nielson Pedology Graduate Research Fellowship (2024), the Montana Agricultural Experiment Station (Project number MONB00364), the Montana Wheat and Barley Committee, the Bayard Taylor Fellowship, and the Montana State University Environmental Analytical Lab. Any opinions, findings, conclusions or recommendations expressed in this material are those of the authors and do not necessarily reflect the views of the funding agencies.

I would like to thank my committee for their individual contributions to these projects and helping me along each step of the scientific journey. I would like to thank my advisor Stephanie A. Ewing for her overall mentorship and guidance in all aspects of this thesis including field work, laboratory work, data analysis, and writing. Robert A. Payn provided invaluable help regarding coding, scientific logic and reasoning, and edits. Trevor P. Irons provided critical expertise in geophysical measurements, field work, and writing, all instrumental skills for bridging the worlds of biogeochemistry and geophysics.

I would like to thank Caitlin Mayernik for initial data collection and laying the foundation for the work presented here. I would like to express my sincere gratitude to the participating agricultural producers who graciously permitted field sampling on their property; without their collaboration this work would not have been possible. Thanks also to Dr. Perry R. Miller for insightful agronomic perspectives and connections, critical to the formation of chapter

three presented in this thesis, and for all guidance hunting related; and thanks to Dr. Miller and Ryan Barnes for their help establishing field site selections and contributing to data collection. We thank Dr. Eric A. Sproles and the entire GEOSWIRL lab for graciously lending their drone equipment and expertise for successful remote sensing of snowpack dynamics. Additionally, I would like to thank Dr. Toby Koffman, Dr. Jane Klassen, Aneliya Cox, Skye I. Keeshin, Carl Krause, Wyatt Kray, Simon Fordyce, Emma Tate, Niko Hinz, and Madisan Chavez for their help with data analysis, sample collection, and instrumentation. A special thanks to Kieran Tharp for continued help in the lab and field during my time at MSU and for braving trench foot while in the field. I thank Cole Edwards, Wally Tonks, Chris Barnes, and Maggie Druckenmiller for laboratory assistance throughout my three years at MSU. A special thank you to my family for encouraging me to pursue higher education in a field that genuinely inspired curiosity. Finally, I would like to thank my girlfriend Darylann Aragon for her unrelenting love and encouragement throughout this experience. Without her support none of this work would have been possible.

TABLE OF CONTENTS

1. GENERAL INTRODUCTION 1

2. UNDERSTANDING NITRATE PROCESSING IN AGRICULTURAL STREAM CORRIDORS USING ELECTRICAL RESISTIVITY TOMOGRAPHY AND A SALT TRACER EXPERIMENT IN AN UNCONFINED RIPARIAN AQUIFER 6

Contribution of Authors and Co-Authors 6
Manuscript Information 7
Abstract 8
2.1 Introduction 9
2.2. Data and Methods 15
2.2.1 Study Area 15
2.2.2 Sampling Well Installation and Groundwater Chemical Analysis 18
2.2.3 Saturated Hydraulic Conductivity Values for Sampling Wells 20
2.2.4 Characterizing Riparian Substrate Architecture 21
2.2.5 Tracer Experiment 23
2.2.6 Evaluating the Influence of Substrate 26
Texture on Tracer Plume Dynamics 26
2.2.6.1 Model Design 26
2.2.6.2 Converting ERT Images and Observation Well Specific Conductivities to Average Concentrations 29
2.2.6.3 Model Uncertainty and Sensitivity Analysis 30
2.2.6.4 Simulating Nitrate Attenuation 32
2.3. Results 33
2.3.1 Saturated Hydraulic Conductivities 33
and Nitrate Concentrations in Riparian Wells 33
2.3.2 Electrical Resistivity Tomography 37
(ERT) of Riparian Substrate 37
2.3.4 Tracer Test 39
2.3.5 Simulating the Tracer Response 43
2.3.5.1 Model sensitivity analysis and best-fit response 43
2.3.5.2 Nitrate Attenuation 45
2.4. Discussion 48
2.4.1 Substrate Architecture 48
Regulates Nitrate Concentrations 48
2.4.2 Groundwater Movement Encompasses 50
Variable Substrate, Suggesting Hydrologic Exchange 50
of Biogeochemically Distinct Waters 50
2.4.3 Flow Dynamics Dictate Nitrate Attenuation Patterns 52
2.5. Conclusions 55

TABLE OF CONTENTS CONTINUED

Acknowledgements 55

3. STUBBLE MANAGEMENT AND ASSOCIATED SOIL MOISTURE DELIVERY IN CULTIVATED SOILS OF DRYLAND CEREAL PRODUCTION SYSTEMS IN CENTRAL AND SOUTHWEST MONTANA, USA 57

Contribution of Authors and Co-Authors 57
Manuscript Information 59
Abstract 60
3.1 Introduction 61
3.2 Data and Methods 65
3.2.1 Study areas 65
3.2.2 Meteorological data, Bozeman and Moccasin MT 71
3.2.3 Snowpack observations, Bozeman and Moccasin MT 71
3.2.4 Soil sample collection and handling, Moccasin MT 74
3.2.5 Soil water content, Bozeman and Moccasin MT 74
3.2.6 Soil water extractions, Moccasin MT 77
3.2.6.1 Soil texture classification, Moccasin MT 78
3.2.7 Analysis of isotopic ratios, Moccasin MT 79
3.2.7.1 Assessing evaporative effects on soil water, Moccasin MT 81
3.3 Results 82
3.3.1 Meteorological data, Bozeman and Moccasin MT 82
3.3.2 Snow depth and water content, ... 85
Bozeman and Moccasin MT 85
3.3.3 Seasonal variation in soil water 91
content, Bozeman and Moccasin MT 91
3.3.4 Soil water isotopic composition, Moccasin MT 98
3.4 Discussion 104
3.4.1 Precipitation delivery dictated by crop stubble height 104
3.4.2 Soil water evaporative signal trends and 108
stubble management microclimate influence on 108
soil water isotopic composition and content 108
3.5 Conclusion 111
Acknowledgements 112

4. GENERAL CONCLUSION 114

CUMULATIVE REFERENCES CITED 117

APPENDICES 142

TABLE OF CONTENTS CONTINUED

CHAPTER TWO: PHYSICAL PARAMETERS OF RIPARIAN WELLS 143

CHAPTER TWO: RIPARIAN WELL SUBSURFACE RESISTIVITY VALUES AND K-MEANS CLUSTERING 145

CHAPTER TWO: RIPARIAN WELLS NITRATE VALUES 152

CHAPTER TWO: CONVERTING ERT IMAGES TO NACL CONCENTRATIONS 158

CHAPTER THREE: ASSESSMENT OF LIDAR DERIVED SNOW DEPTH COMPARED TO MANUALLY OBSERVED MEASUREMENTS 162

CHAPTER THREE: SPATIAL DISTRIBUTION OF LIDAR DERIVED SNOW DEPTH AND SWE OBSERVATIONS 165

CHAPTER THREE: MOCCASIN SOIL TEXTURE 167

CHAPTER THREE: EXPERIMENTAL ANALYSIS OF CRYOGENIC EXTRACTION EFFICIENCIES 169

CHAPTER THREE: COMPARISON OF SOIL WATER LC EXCESS VALUES BETWEEN SHORT AND TALL STUBBLE AT THE END OF JUNE 171

CHAPTER THREE: SUMMARY STATISTICS OF SOIL WATER ISOTOPE VALUES 173

STATEMENT OF DATA AVAILABILITY 177

LIST OF TABLES

Table Page

1. Table 2.1: Saturated hydraulic conductivity (K_{sat}, m d^{-1}), bulk electrical resistivity (Ω m) of ERT image cells overlapping the well screening, and nitrate concentration (NO_3-N mg L^{-1}) in 16 riparian well locations within the Louse Creek stream corridor. K_{sat} values were assessed with well recovery tests during June of 2022 (RW01-RW10) and May of 2024 (RW11-RW16). Data for ERT images were collected in June of 2022 and 2024. Samples for nitrate analysis were collected during March-December, 2021-2024. Nitrate concentrations include results for wells RW01-RW10 reported in Mayernik et al., 2025. Wells RW11-RW16 were installed and sampled in June of 2024. 36

2. Table 2.2: Summary statistics of electrical resistivity categories resulting from a K-means sorting into four clusters. Source data for the analysis were from ERT transects collected at riparian wells RW01, RW02, RW03, RW04, RW06, RW08, RW09, and RW10. 38

3. Table 3.1: Synthesis of sampling type by date for each location throughout our sampling campaigns of 2022-2023 (Bozeman) and 2023-2024 (Moccasin). 70

4. Table 3.2: Summary statistics of manually measured snow depth (cm) and SWE (cm) values sampled in Bozeman (2022-2023) and Moccasin (2023-2024). 86

5. Table 3.3: Total height of water across the sampled soil profile. Total height of water calculated by adding the height of water from 0-10, 10-20, and 20-30 cm on each date for each stubble height treatment. Difference calculated tall minus short, where negative values indicate less water in tall. The three largest absolute differences in soil water storage are bolded. 93

6. Table 3.4: Summary statistics of soil water height by depth collection interval and stubble treatment type, on each collection date. Difference calculated tall minus short, where negative values indicate less water in tall. The three largest absolute differences in soil water storage are bolded. Low confidence that mean values were different between short and tall stubble at any individual depth on any day. 97

7. Table 2.S1: Physical well parameters and locations for all riparian well sites within the Louse Creek stream corridor. 144

LIST OF TABLES CONTINUED

Table Page

8. Table 2.S2: All individual nitrate values (NO_3-N mg L^{-1}) and associated uncertainty (NO_3-N mg L^{-1}) presented in chapter two of this thesis. 153

9. Table 3.S1: Particle size percentages of clay, silt, and sand at each soil depth interval. Total percentages may not add up to 100% due to small number of particles not being classified by the machine. Soil texture class based on USDA standard practices(USDA NRCS, n.d.). 168

10. Table 3.S2: Summary statistics of soil water δ^2H, $\delta^{18}O$, and lc excess values. Summary statistics is grouped by collection date, then treatment type, and soil collection date. 174

LIST OF FIGURES

Figure Page

1. Figure 1.1: Combined study area of both chapters presented in this thesis. The Moccasin study site is the green circle, within the Northern Great Plains ecoregion (Padbury et al., 2002), where one of the two agricultural producers' sites are located for assessing stubble height management (yellow polygon) and the Louse Creek stream corridor site (blue circle) are located. The orange point is the location of the Bozeman agricultural study site, the second stubble height management research location. 5

2. Figure 2.1: Maps and aerial imagery of the study area. (A) Location of the Judith River Watershed within the state of Montana and Northern Great Plains (NGP). (B) The Moccasin Terrace located in the lowlands of the JRW; (C) The Louse Creek stream corridor study site (blue circle) with a color map of terrace land use cover by major crop cultivation in 2022 (United States Department of Agriculture (USDA) National Agricultural Statistics Service (NASS), 2023). 11

3. Figure 2.2: Nitrogen movement and processing from uplands to stream corridors in dryland wheat production systems. The diagram depicts mixing and nitrate processing within the stream corridor as water moves through the riparian aquifer. Nitrate concentrations averaging 22.1 NO_3-N mg L^{-1} were observed in the terrace groundwater, 7.32 NO_3-N mg L^{-1} in the stream water, and 1.14 NO_3-N mg L^{-1} in the riparian (Mayernik et al., 2025; Sigler et al., 2018). 14

4. Figure 2.3: Maps and aerial imagery of the study area. (A) Aerial image cropped to the outline of the Moccasin Terrace (strath terrace landform) in the Judith River watershed, including the location of the study site in the headwaters of the Louse Creek drainage (blue circle). (B) Aerial image of the Louse Creek study reach indicating locations of riparian wells (white pentagons with labels), direction of stream flow (blue arrows), tracer experiment area (red box), and initial ERT surveys (black lines, with the black arrows depicting survey direction). (C) Map of the additional wells and electrical resistivity tomography (ERT) transect used for the tracer experiment, where tracer fluid was injected into RW11 (red pentagon), continuously monitored with specific conductivity probes at RW13 (green pentagon), adjacent downgradient monitoring wells RW12 and RW14 (blue pentagon), and further downgradient wells monitored with point measurements of specific conductivity in RW15 and RW16 (white pentagons). 18

LIST OF FIGURES CONTINUED

Figure Page

5. Figure 2.4: Hydraulic conductivity values (log scale) estimated from aquifer recovery tests in riparian wells in the Louse Creek stream corridor. Colored bars indicate wells used for the tracer injection (red, RW11), the central observation of the tracer plume (green, RW13), and lateral positions on the tracer plume (blue, RW12 and RW14). K_{sat} values of wells are categorized as "higher" and "lower" values, separated at 1 m d^{-1} (dashed line). Error bars represent uncertainty in the predicted saturated hydraulic conductivity value based on the modeling fitting process. 34

6. Figure 2.5: Nitrate concentrations in Louse Creek riparian wells categorized by higher K_{sat} (>1 m d^{-1}; blue points) and lower K_{sat} (<1 m d^{-1}; brown points) values. The saturation of the point color indicates a sample from a given riparian well. The internal black box is bounded vertically by the first and third quartile values, while the white dot represents the median value, and the plot width indicates frequency of observations. RW15 and RW16 were excluded from analysis due to no assessed K_{sat} value..... 37

7. Figure 2.6: Subsurface resistivity values (left) and zones with common resistivity values based on K-means clusters of ERT data (right) at transects intersecting four different riparian well locations within the Louse Creek stream corridor. Each transect includes the location of a well (black vertical bar; (A) RW04, (B) RW08, (C) RW03, and (D) RW10), with the well screen presented as a grey vertical bar. Clustering thresholds are provided in Table 2.1..... 39

8. Figure 2.7: Specific conductivities observed at individual wells during the tracer experiment. Discontinuities in the recession of the breakthrough curve are the result of removing probes during the experiment to download data. Symbols indicate point measurements collected using a single conductivity probe in wells lacking continuous logging. Data were collected at 60-second intervals for 27.75 hrs, and subsequently at 15-minute intervals until the end of the injection period (11.3 days). Vertical dashed grey lines indicate the beginning and the end of the period over which 13-time lapse ERT images of the tracer plume were collected. 40

LIST OF FIGURES CONTINUED

Figure Page

9. Figure 2.8: ERT images at the RW14 transect over 24 hrs following initiation of the tracer injection. The ERT transect intersecting wells RW12-14 is located 0.5 m downgradient from the injection well (RW11). The left column displays the cross-sectional distribution of electrical resistivity and the right column depicts the percent change in resistivity from the cross-sectional distribution not influenced by the tracer test (panel A). The brown polygon outline represents the extent of the fourth K-means cluster, based on the baseline image using thresholds documented in Table 2.1. Well casings are indicated by black bars and well screens are indicated by grey bars. The time at the top left of each panel is the time after the initiation of the 6.5-hr injection. 42

10. Figure 2.9: (A-B) Parameter values for the 2,500 of the 5,000 realizations that were most likely to be within the range of uncertainty in the observed breakthrough curve (grey points). Dark blue points are simulations in the 2.5th percentile of the best-fits to the normalized breakthrough curve, and the gold point is the best fit to the normalized breakthrough curve. (A) KC vs. fC and (B) KF vs fC. (C) Simulated concentration responses. The green points reflect our estimate of the breakthrough curve for the average concentration across the plume. The red lines indicate all 5,000 simulations, grey lines represent the 2,500 simulations that are most likely to be within the uncertainty window, dark blue lines indicate simulations within the 2.5th percentile of the best-fit to the normalized breakthrough curve, and the gold line is the best-fit to the to the normalized breakthrough curve (K_C = 8.3m d^{-1}, K_F = 0.895m d^{-1}, f_C = 57%). The vertical dashed black line indicates when the hydraulic head at the injection well returned to ambient conditions. (D) Normalized simulation results that fit our uncertainty window, with repeated color patterns. 44

LIST OF FIGURES CONTINUED

Figure Page

11. Figure 2.10: Simulated mass fraction of nitrate (NO_3-N mg L^{-1}) remaining in the aquifer (fN, out) corresponding to flow simulations and the assumption of solute reaction occurring in the fine texture component. Results are based on a first-order nitrate reaction rate constant in the fine textured sediment (k_F = 1.39×10−5 $s - 1$) (Marzadri et al., 2012; Ocampo et al., 2006; Reinhold et al., 2025). The dashed black line denotes the observed fN, out value between RW11 (one observation) and an average of two concentration values obtained for RW12-RW13 (Table 2.S2), with propagated analytical uncertainty indicated with a grey box. The size of the points corresponds with the simulated K_C value (2.5-35 by 0.1), with larger points reflecting higher K_C values. Our best fit simulation is marked in gold (no point scaling for visualization purposes), the 2.5th percentile of closest fit simulations to the normalized breakthrough curve in dark blue (no point scaling), 50% of simulations most likely matching our uncertainty window in grey, and the remaining simulations in red. Error bars associated with the plotted 2.5th percentile best fit simulations reflect the range of fN, out values obtained by varying k_F an order of magnitude above and below the literature-based estimate. 47

12. Figure 3.1: Study sites. (A) The location of the two study site locations, Bozeman (red) and Moccasin (green) which is within the Northern Great Plains ecoregion and the state of Montana. (B) Bozeman study site at the Arthur H. Post research farm, within ongoing crop rotation study plots (CARB). Red polygons indicate short stubble locations (<15 cm), and blue indicate tall stubble (>45 cm). Orange circles indicate locations of Hydra Probe soil moisture sensors. (C) Moccasin study site on private agricultural land showing stubble height distribution. Red polygons indicate short stubble (<20 cm), and blue polygons indicate tall stubble (>60 cm). Soil collection locations documented by labeled brown circles and Sentek moisture probe locations indicated by purple points. 66

13. Figure 3.2: (A) Spatial patterns in 30-year (1991-2020) mean annual precipitation (cm) observed in Montana, including study sites at Bozeman and Moccasin, Montana. (B) Monthly precipitation patterns at Bozeman and Moccasin, Montana. Data represents average over 30-year period (1991-2020), Data from the Oregon State PRISM network (PRISM Climate Group, 2023). 68

LIST OF FIGURES CONTINUED

Figure Page

14. Figure 3.3: Precipitation and soil meteorological data during soil collection period, from September 2022 through July 2023, at the Bozeman Horticulture (Hort) Farm Mesonet site (Montana Climate Office, 2025). (A) Hourly snow depth and precipitation as snow or rain based on temperature. Precipitation data are dark blue to represent rainfall, when air temperature is >0 °C, and pink for snow, when air temperature is <0 °C. Vertical dashed lines represent sampling events, with grey lines indicating manual snow sampling and black indicating associated LiDAR drone flights. Triangles represent manual observations of snow depth (light blue) and snow water equivalent (navy), respectively, adjacent to the meteorological station. (B) Soil temperature at the depths of 10, 20, and 50 cm. (C) Soil volumetric water content at 10, 20, and 50 cm depths. Red (short stubble) and blue (tall stubble) indicate average measured volumetric water content, from 10-20 cm, in the two plots at the CARB study site. 83

15. Figure 3.4: Precipitation and soil meteorological data during soil collection period, from September 2023 through June 2024, at the Central Agricultural Research Center (CARC) Mesonet site (Montana Climate Office, 2025). (A) Hourly snow depth, snow water equivalent (SWE) measured with a snow scale, and precipitation as snow or rain based on temperature. Precipitation data is blue to represent rainfall, when air temperature is >0 °C, and pink for snow, when air temperature is <0 °C. Grey vertical dashed lines reflect combined snow and soil sampling events, brown only soil sampling, and green indicated field pea sampling date. (B) Soil temperature at the depths of 10, 20, and 50 cm. These depths were chosen to reflect general sampling depths of soil collection protocol. (C) Soil volumetric water content at 10, 20, and 50 cm depths. Red (short stubble) and blue (tall stubble) indicate average measured volumetric water content, from 0-35 cm, within the Moccasin producers' field. Points reflect average volumetric water content, based on total water from 0-30 cm, averaged across three bulk soil samples collected in the field, in the short (red) and tall (blue) stubble. 84

LIST OF FIGURES CONTINUED

Figure Page

16. Figure 3.5: Snowpack information collected at the Bozeman and Moccasin study sites. Reported p-value reflects confidence from either t-test, assuming normality, or Wilcoxon rank sum test, when normality is violated. (A) Snow depths (cm) and SWE (cm) in short and tall stubble at the Bozeman field site 17 February 2023. (B) Snow depths (cm) and SWE (cm) in short and tall stubble at the Bozeman field site 2 March 2023. (C) Snow depths (cm) and SWE (cm) in short and tall stubble at the Bozeman field site 29 March 2023. (D) Snow depths (cm) and SWE (cm) in short and tall stubble at the Moccasin producers' field site 16 February 2024. Observed SWE (cumulative mean = 1.70cm) is slightly larger than the snow scale reading (~1.23 cm) on this date in Figure 4C. 87

17. Figure 3.6: LiDAR derived distribution of snow depth (cm) and SWE (cm) values witin short (red) and tall (blue) stubble at the Bozeman study site. Observtion frequency represents number of LiDAR derived point estimates. Solid line depicts LiDAR derived mean snow depth and SWE values while the dashed line indicates manually measured mean snow depth and SWE values. Mean values for each group reflected on the top of each graph alomg with associated uncertainty (one standard deviation). (A) Snow pack analysis 17 February 2023. (B) 2 March 2023. 89

18. Figure 3.7: Snow cover across Moccasin producers' field 23 January 2024. (A) Orthomosaic RGB image of producer's field, captured via drone. (B) Radom forest model assessment of snow-covered area (white) and bare soil (red) based on orthomosaic image. Tall and short stubble divides marked as S and T lettering at top of image. 90

19. Figure 3.8: Field pea crop growing conditions. (A) Crop growth on 11 June 2024. Picture captures crop growth, prior to flowering, in short stubble at the Moccasin field site. Plant height was roughly 10-20 cm during this time. (B) Crop growth on 26 June 2024. Picture captures crop growth in tall stubble at the Moccasin field site. Plant height was roughly 50-60 cm on this date (Visual estimate). 95

LIST OF FIGURES CONTINUED

Figure Page

20. Figure 3.9: Soil water within the top 30 cm of the soil profile, by sample collection date. Samples at each depth interval (0-10, 10-20, 20-30 cm) reflect an average value from three different locations in tall stubble (S1, S2, and S3) and short stubble (S4, S5, S6). Error bars indicate propagated uncertainty associated with calculating the total height of water by summing the three depth intervals. Field pea planting indicated by vertical green dotted line (2 May 2024)..... 96

21. Figure 3.10: Seasonal trends (January through June 2024) of terrace soil water δ^2H values. (A) All soil water δ^2H values samples during sampling period. Soil samples from short stubble indicated as open circles and tall stubble as open triangles. Precipitation values marked as crosses in dark blue for monthly precipitation sampler collected at the Central Agricultural Research Center and as snow in light blue. (B) Soil water δ^2H values at a collection depth of 0-10 cm. Black line represents best fit trend line of soil water values. (C) Soil water δ^2H values at a collection depth of 10-20 cm. (D) Soil water δ^2H values at a collection depth of 20-30 cm. 99

22. Figure 3.11: Soil water isotopic composition with depth trends. Groups that share the same lower-case letter represent a lack in confidence that the distributions have different means. (A) δ^2H values for each depth interval at 0-10, 10-20, and 20-30 cm depths. The solid black line represents the multi-year (2012-2022) volume-weighted mean (VWAM) δ^2H precipitation value with uncertainty reflecting variance in precipitation at the CARC (Mayernik, et al., 2024). Color corresponds to collection date and the symbol corresponds to stubble treatment, with open circles as shorter stubble and open triangles as tall stubble. (B) Lc excess values of soil water at each depth interval. The solid black line represents the LMWL and the dashed lines reflect the 95% confidence interval around this established LMWL (Mayernik, et al., 2024). (C) δ^2H values grouped by stubble height, including VWAM line indicated in black. (D) Lc excess values grouped by stubble height. 101

23. Figure 3.12: Dual-isotope plot of all water isotope samples collected during sampling period. (A) Soil water samples color coded by soil collection depth and (B) soil water samples color coded by sample collection date relative to the local meteoric water line (solid black line) and 95% confidence interval (dashed black lines) (Mayernik, Ewing, Sigler, et al., 2024). Open circles represent soil samples from short stubble and open triangles reflect samples from tall stubble. 102

LIST OF FIGURES CONTINUED

Figure Page

24. Figure 3.13: Seasonal trends of line excess (lc excess) values across all sampling days. (A) Values for soils sampled from 0-10 cm; (B) 10-20 cm; and (C) 20-30 cm. The solid black line indicates the local meteoric water line, with the dashed lines reflecting the 95% confidence interval (Mayernik, Ewing, Sigler, et al., 2024). Open circles represent soil samples from short stubble and open triangles reflect samples from tall stubble. The size of the symbol corresponds to the volumetric water content at that specific soil depth and location, with bigger symbols reflecting higher water content. 103

25. Figure 2.S1: Raw subsurface resistivity values (bottom) and K-means clustering results (top) at riparian well RW01 within the Louse Creek stream corridor. Image traverses a well (black vertical bar), with the well screen presented (grey vertical bar). 146

26. Figure 2.S2: Raw subsurface resistivity values (bottom) and K-means clustering results (top) at riparian well RW02 within the Louse Creek stream corridor. Image traverses a well (black vertical bar), with the well screen presented (grey vertical bar). 147

27. Figure 2.S3: Raw subsurface resistivity values (bottom) and K-means clustering results (top) at riparian well RW03 within the Louse Creek stream corridor. Image traverses a well (black vertical bar), with the well screen presented (grey vertical bar). 148

28. Figure 2.S4: Raw subsurface resistivity values (bottom) and K-means clustering results (top) at riparian well RW04 within the Louse Creek stream corridor. Image traverses a well (black vertical bar), with the well screen presented (grey vertical bar). 149

29. Figure 2.S5: Raw subsurface resistivity values (bottom) and K-means clustering results (top) at riparian well RW08 within the Louse Creek stream corridor. Image traverses a well (black vertical bar), with the well screen presented (grey vertical bar). 150

30. Figure 2.S6: Raw subsurface resistivity values (bottom) and K-means clustering results (top) at riparian well RW10 within the Louse Creek stream corridor. Image traverses a well (black vertical bar), with the well screen presented (grey vertical bar). 151

LIST OF FIGURES CONTINUED

Figure Page

31. Figure 2.S7: Piecewise segmented relationship between bulk resistivity percent change and specific conductivity (µS cm^{-1}), measured at RW13 and RW14. Resistivity change values are presented in absolute value and are the average value from ERT cells along the well screen (RW13, RW14), and the specific conductivity (µS cm^{-1}) value is the average value, at each well, during the ERT collection period. The piecewise relationship breakpoint occurs at 33.6 average resistivity change (purple dashed line)..... 159

32. Figure 2.S8: Linear relationship between specific conductivity (µS cm^{-1}) and NaCl concentration (mg L^{-1}). One calibration point was removed due to inaccurate NaCl concentration recording. 160

33. Figure 2.S9: Linear relationship between average aquifer NaCl concentration, derived from ERT images, and the NaCl observed from the specific conductivity recording at RW13. This relationship is used to convert our continuous specific conductivity (µS cm^{-1}) readings at RW13 to an average aquifer concentration. 95% confidence interval encompasses the propagated uncertainty associated with converting from percent change in resistivity, from ERT images (Figure 2.S7) to a specific conductivity (µS cm^{-1}), and then from a specific conductivity (µS cm^{-1}) to a NaCl concentration (mg L^{-1}) (Figure 2.S8). Confidence interval derived using Monte Carlo uncertainty propagation. 161

34. Figure 3.S1: Assessment of corrected LiDAR derived snow depth to on ground measured values, on 17 February 2023. Average difference between the observed snow depth samples and LiDAR derived snow depth was 4.6 cm, favoring higher snow depths in the manually observed points. This correction value was applied to all LiDAR derived snow depths. Red points indicate snow depth in short stubble plots and blue in tall stubble. Black line represents best fit and green line is 1:1..... 163

35. Figure 3.S2: Assessment of corrected LiDAR derived snow depth to on ground measured values, on 2 March 2023. Average difference between the observed snow depth samples and LiDAR derived snow depth was 8.8 cm, favoring higher snow depths in the manually observed points. This correction value was applied to all LiDAR derived snow depths. Red points indicate snow depth in short stubble plots and blue in tall stubble. Black line represents best fit and green line is 1:1..... 164

LIST OF FIGURES CONTINUED

Figure Page

36. Figure 3.S3: Spatial distribution of LiDAR derived snow depth and SWE values, recorded at the Bozeman study site, during the winter of 2022-2023. Red polygons indicate short stubble and blue tall stubble plots. Yellow points in snow depth plots reflect manual observations of snow depth, recorded within 24-hr of flights. 166

37. Figure 3.S4: Soil particle size analysis of soils at depth interval of 10, 20, and 30cm at the study site. Each line represents an average of six different samples collected at each depth, plotted as transparent background lines. We classify clay as particles between the size of 0-6 μm, silt as 6-50 μm, and sand as 50-200 μm (Schaetzl & Thomson, 2015). 168

38. Figure 3.S5: Experimental analysis of spiked soil water. Black points reflect extracted soil water δ2H values (mean = -130.22) and the associated standard deviation (±6.60) (black shading). The red line represents the spiked soil waters known value (-130.15) and its associated analytical uncertainty (±1.12) (red shading). The known value of the spiked water was established over 31 observations, from 9 March 2024 to 7 March 2025, run amongst reported isotope values in this paper. Previously extracted waters isotopic composition for each soil sample is plotted in orange. 170

39. Figure 3.S6: Differences in lc excess values between short and tall stubble at all depth increments on 26 June 2024. We report high confidence that the mean lc excess value is different between short and tall stubble (t-test, p-value < 0.05). This is the only date with differences in lc excess values between the short and tall stubble across all depth increments. 172

ABSTRACT

In the Judith River Watershed of Central Montana, chronically high and increasing nitrate concentrations in shallow groundwater have motivated decades of research. This work has quantified nitrate leaching from dryland agricultural soils into adjacent uncultivated stream corridors. In this thesis I investigated both the influence of riparian substrate on nitrate attenuation patterns within these stream corridors and soil water storage patterns as a function of crop residue management, a control on nitrate leaching into the groundwaters. High-nitrate terrace groundwaters flowing into stream corridors are subject to nitrate attenuation, as abundant organic matter and hydric soils support anaerobic biogeochemical activity. We hypothesized that variation in the sedimentary substrate hosting riparian aquifers controlled these biogeochemical conditions and flow dynamics, with finer textured substrate increasing nitrate transformation. We tested this hypothesis in a 700-m reach of a stream corridor draining the Moccasin Terrace (near Moccasin, Montana USA), simulating groundwater dynamics, constrained by geophysical surveys, to assess how substrate interactions control nitrate attenuation. We explored how the observed plume and associated nitrate concentrations were consistent with finer textured substrate regulating nitrate attenuation, and coarser textured substrate regulating water movement. In the upland agricultural soils that supply nitrate to stream corridors, management practices that promote water use efficiency, such as increasing the height of the standing crop stubble following harvest, support continuous cropping rotations which limits nitrate leaching loss. We hypothesized that increased stubble height would entrap more snow during the winter, providing additional soil moisture during spring melt, and reduce evaporative losses of shallow soil water. We used a time series of soil water isotope measurements to quantify soil water storage and loss processes relative to seasonal temperature, snow retention and melt, and pulse crop growth. Our observations suggest that tall stubble enhances snow entrapment and limits evaporative soil water losses, but the magnitude of the effect depends on meteorological conditions of the water year. Taken as a whole, my work demonstrates how distinct controls on water balance and flux in these agricultural landscapes dictate outcomes of nutrient use inefficiencies enhanced or imparted by both landscape character and human management.

CHAPTER ONE

GENERAL INTRODUCTION

In the United States, agricultural systems are the leading source of stream and river pollution (Evans et al., 2019), caused by an increase in nitrogen fertilizer inputs for improved crop yields (Tilman, 1998). While nitrogen fertilizer use has helped feed a continually growing world population, it has also resulted in unintended consequences for environmental water quality. High rates of fertilizer application, exacerbated by other soil management practices (Custer, 1976; John et al., 2017; Sigler et al., 2020), have led to leaching of nitrate (NO_3^-) from soils to groundwater and surface water, reflecting hydrologic connection between terrestrial uplands and adjacent riparian areas (Houlton et al., 2013; Ranalli & Macalady, 2010; Tesoriero et al., 2013). The resulting excess nitrate in environmental waters has impaired natural ecological functions and raised human health concerns (Bouchard et al., 1992; Heisler et al., 2008; Melillo, 2021; Smith et al., 1999).

This research is organized into two elements examining hydrological and biogeochemical interactions in soils and shallow groundwater in an agricultural landscape, and suggest how management decisions directly and indirectly limit or exacerbate excess nutrients in environmental waters. The first research element investigated how the physical structure of riparian substrate within stream corridors affects subsurface flow patterns, with implications for its influence on the reduction of nitrate before export in the stream channel. The second research element investigated how wheat stubble height management in dryland agricultural systems influences soil water inputs, facilitating conditions favorable to subsequent pulse crop growth, and potentially minimizing nitrate transport due to maintained roots in the soils.

Both research elements were conducted in a semi-arid agricultural region in central Montana, USA (Figure 1.1). Dryland small-grain agricultural systems in this region are limited by water availability and require management practices that result in water use efficiency for maximum crop productivity (Nielsen et al., 2005). The practice of summer fallow is a common rotational strategy in these systems, used to maximize soil water storage for the benefit of future crop rotations, with the application of herbicides to inhibit plant growth throughout an entire growing season (Lawrence et al., 2018; Nielsen et al., 2005; Tanaka et al., 2010). Despite the perceived benefits to soil water management, summer fallow has the potential to influence soil nutrient dynamics, including increased leaching of soil nitrate, derived from nitrogen amendments and mineralization of soil organic matter (Custer, 1976; John et al., 2017), into hydrologically connected stream corridors (C. Miller et al., 2013, M.S. Thesis; Sigler et al., 2018), degrading water quality. However, within the agriculturally intensive Judith River watershed, summer chemical fallow area in this watershed has declined by 248.14 km² (3.46% of total area) from 2014 to 2023, likely replaced by pulse crop adaptions (e.g., lentil, chickpea, field pea), though it remains a part of producers' rotations (USDA, 2025).

Within agricultural landscapes, riparian areas that receive nutrient-laden groundwater from overlying agricultural systems have potential to slow water and solute movement, creating a groundwater buffering zone that facilitates the reduction of nitrate and other solutes before export in the stream channel (Hanson et al., 1994; Hill, 1996; Rivett et al., 2008; P. G. Vidon & Hill, 2006; Warwick & Hill, 1988; Willems et al., 1997). The physical structure of sedimentary substrate within these saturated zones brings high-nitrate groundwater into contact with organic matter (supplying organic carbon) and anoxic zones that facilitate reducing processes. Among

these processes, heterotrophic denitrification is thought to be the leading mechanism in nitrate removal within stream corridors (Cooper, 1990; Haycock & Pinay, 1993; Hill et al., 2000; Verchot et al., 1997; P. G. F. Vidon & Hill, 2004). Finer textured and less transmissive materials, particularly surficial soils, supply organic carbon derived from plant productivity, promote oxygen consumption, and facilitate transformation of solutes like nitrate that can serve as a preferred terminal electron acceptor in the absence of oxygen. More transmissive substrate shortens residence times and limits anoxia, facilitating transport of solutes like nitrate with less loss to chemically reductive metabolism (Shabaga & Hill, 2010; P. G. F. Vidon & Hill, 2004; P. G. Vidon & Hill, 2006). Thus, the amount of hydrologic exchange between coarse textured aquifer material and fine textured riparian soils and substrate should dictate the extent of solute reduction processes within riparian areas (Devito et al., 2000; Hill, 2019; Ranalli & Macalady, 2010; P. Vidon et al., 2010).

To reduce nitrate leaching from agricultural systems upstream of riparian areas, management practices that enhance soil water retention – beyond traditional summer fallow – are needed to support conditions promoting continuous cropping. Stubble height management has shown promise for both increased soil water retention and beneficial microclimate conditions for crop growth. Increased stubble height has been linked with increased snow retention during winter precipitation events, adding additional soil moisture upon thaw (Aase & Siddoway, 1980; Black & Siddoway, 1977; Campbell et al., 1992; Schillinger & Wuest, 2021). In addition, tall stubble provides increased shading of the soil surface that prevents soil heating and promotes boundary layer conditions that reduce evaporation from the soil surface (Campbell et al., 1992; H. W. Cutforth & McConkey, 1997), and decreased surface wind velocities that increase

favorable growing conditions and reduce soil erosion (Aase & Siddoway, 1980; Ann McCauley & Clain Jones, 2005; McMaster et al., 2000). Increased soil moisture storage under taller stubble allows for increases in water use efficiency for subsequent crops, with soil texture dictating the magnitude of retention, and generally results in improved crop yields and economic returns for producers (Campbell et al., 1992; H. Cutforth et al., 2011; H. W. Cutforth et al., 1997). Although the benefits of taller stubble are generally known in a dryland agricultural context, additional research is needed as producers' preferences change (Schillinger & Wuest, 2021), as climate impacts dryland agriculture regionally (Whitlock et al., 2017), and for specific conditions within the Northern Great Plains ecoregion (Padbury et al., 2002).

In this thesis I examined riparian groundwater flow as a function of substrate composition within an agriculturally influenced stream corridor, and soil moisture storage benefits of taller stubble in hydrologically connected terrace soils. These investigations provide case studies of natural processes interacting with human land management to dictate water quality within agriculturally influenced aquifers and stream corridors. Deep percolation of nitrate into groundwater can be limited by dryland agricultural management practices that facilitate adequate soil water storage to support a pulse crop in place of summer fallow. Attenuation of leached agricultural nitrate in riparian areas can be enhanced by substrate configurations that slow water movement in conjunction with supply of organic carbon. With these studies I pose a general question: *How do management practices interact with soil and substrate character to influence the storage of water and the transport of nutrients in agricultural landscapes?* These connections are of the utmost importance in Montana as we face an uncertain future regarding water availability and water quality with a changing climate (Whitlock et al., 2017).

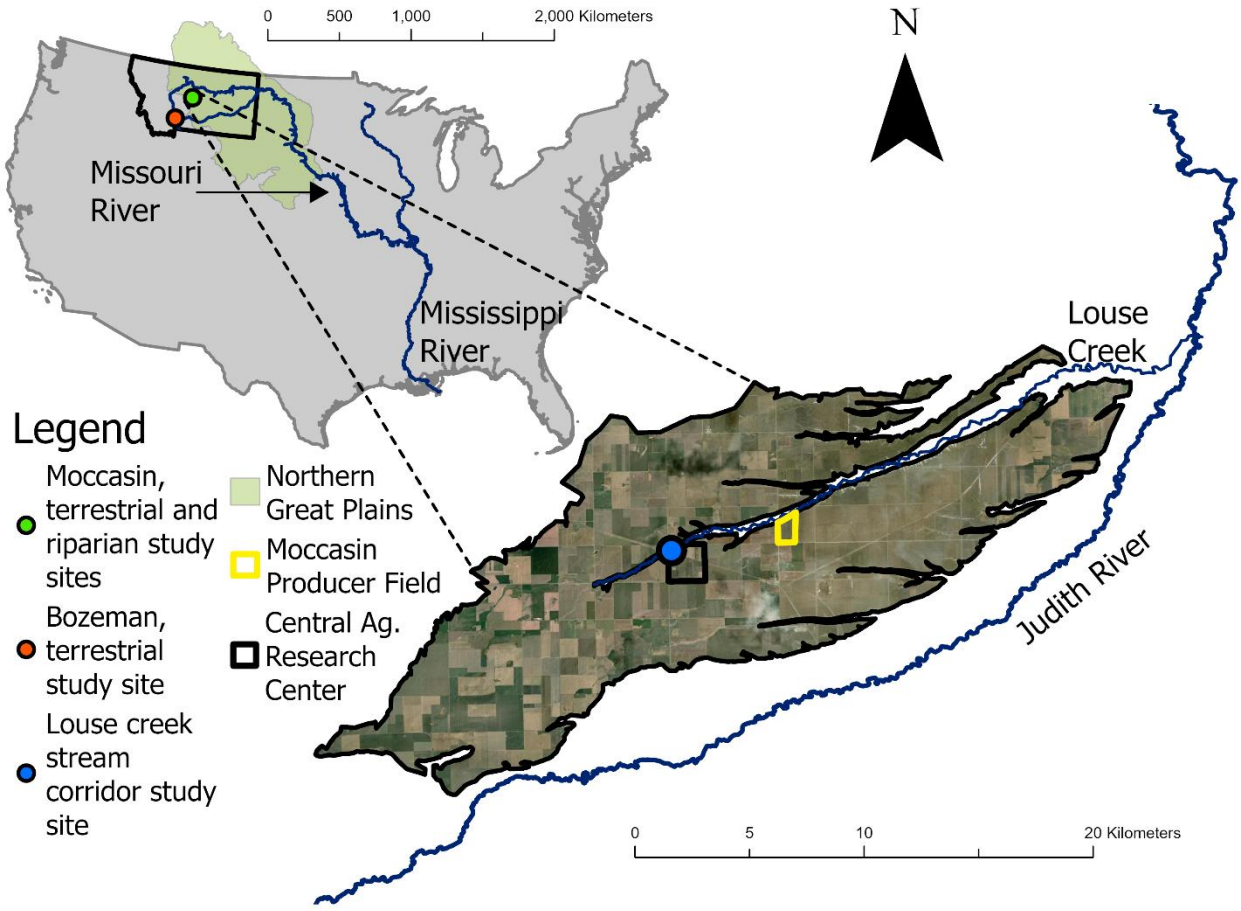


Figure 1.1: Combined study area of both chapters presented in this thesis. The Moccasin study site is the green circle, within the Northern Great Plains ecoregion (Padbury et al., 2002), where one of the two agricultural producers' sites are located for assessing stubble height management (yellow polygon) and the Louse Creek stream corridor site (blue circle) are located. The orange point is the location of the Bozeman agricultural study site, the second stubble height management research location.

CHAPTER TWO

UNDERSTANDING NITRATE PROCESSING IN AGRICULTURAL STREAM CORRIDORS USING ELECTRICAL RESISTIVITY TOMOGRAPHY AND A SALT TRACER EXPERIMENT IN AN UNCONFINED RIPARIAN AQUIFER

Contribution of Authors and Co-Authors

Manuscript in Chapter 2

Author: Jack W. Poole

Contributions: Collected field data, developed ideas and methodologies, and compiled manuscript.

Co-Author: Stephanie A. Ewing

Contributions: Developed research questions and goals, lead investigator on project, contributed to methodology creation, guidance on data analysis and extensive feedback on the manuscript.

Co-Author: Robert A. Payn

Contributions: Provided extensive guidance on analysis and feedback on the manuscript.

Co-Author: Trevor P. Irons

Contributions: Provided guidance on analysis and visualizations, contributed to field work, and provided feedback on the manuscript.

Manuscript Information

Jack W. Poole, Stephanie A. Ewing, Robert A. Payn, Trevor P. Irons

Journal of Hydrological Processes

Status of Manuscript:
☒ Prepared for submission to a peer-reviewed journal
☐ Officially submitted to a peer-reviewed journal
☐ Accepted by a peer-reviewed journal
☐ Published in a peer-reviewed journal

Abstract

Extensive application of nitrogen fertilizer to increase crop yields can combine with mineralized soil organic matter to contribute excess nitrate loading to groundwater and surface water, raising concerns for human health and ecosystem integrity that depend on the quality of these water resources. In semi-arid regions of the Judith River Watershed (JRW) of central Montana, chronically high and increasing upland groundwater nitrate concentrations (~20 NO_3-N mg L^{-1}) reflect leaching from non-irrigated cultivated soils with limited water holding capacity that ultimately drain to adjacent stream corridors. In these stream corridors, high nitrate concentrations may be attenuated as a function of the hydrologic connections among the uplands, stream channels, and riparian zones, where abundant organic matter and hydric soils support anaerobic biogeochemical activity in riparian aquifers. Here, we assess the structure of sedimentary substrate thought to control these hydrologic connections and biogeochemical conditions across a 700-m reach of a stream corridor draining the Moccasin Terrace (near Moccasin, Montana USA). We hypothesize that the spatial distribution of metabolically important solute concentrations is controlled by the localized conditions of the aquifer as determined by the hydraulic conductivity and biological activity that tend to covary with sediment texture. Coarse-textured sediments facilitate advective transport of solute and exchange water with fine-textured sediments that slow water movement and facilitate solute reduction processes. We test these hypotheses using spatiotemporal patterns in groundwater chemistry and hydraulic characteristics at 16 shallow (< 1.5 m) wells, cross-sectional variation in electrical resistivity tomography (ERT) surveys of the shallow riparian aquifer, and time-lapse ERT imaging of a tracer plume induced by a conductive salt solution injected into the riparian aquifer.

We use our observations to constrain the size, character, and connectivity of the riparian aquifer, using simple mixing models in comparisons with tracer experiments to explore the interplay of transport and reaction dynamics that attenuate nitrate loading from agricultural management practices to improve water quality. We observe that flow dynamics are intimately connected with nitrate concentrations, with riparian wells completed in coarser substrate having higher nitrate concentrations compared to wells completed in finer substrate. Additionally, our simulation results suggest that the proportion of coarse textured material dictates the total amount of flow while the proportion of flow through the finer textured material may dictate nitrate reduction processes.

2.1 Introduction

Modern agriculture has used extensive application of nitrogen fertilizers to increase crop yields (Tilman, 1998). This practice has helped feed a continually growing world population, but application of nitrogen-based fertilizers in excess of plant use has led to leaching of dissolved nutrients such as nitrate (NO_3^-) to groundwater and surface water (Houlton et al., 2013). The resulting effects on the quality of water resources have raised concerns for human health and ecosystem integrity (Bouchard et al., 1992; Heisler et al., 2008; Melillo, 2021; Smith et al., 1999). Riparian areas that receive these waters have potential to act as buffers that slow water movement, facilitating the reduction of nitrate and other solutes (Hanson et al., 1994; Hill, 1996; Rivett et al., 2008; P. G. Vidon & Hill, 2006; Warwick & Hill, 1988; Willems et al., 1997). Regions with relatively shallow and slow-moving groundwater in riparian zones support productive, water-loving vegetation, and thus soils in these regions accumulate organic matter that provides the energy for the transformation of metabolically important solutes by the

heterotrophic microbial community. We suggest that understanding the biogeochemical potential of flow through riparian aquifers requires an understanding of the covariance between the rate of water movement through varying soil textures and the resulting variation in the biogeochemical potential of the microbial community. Here, we use physicochemical surveys and geophysical observations of a groundwater tracer experiment in the riparian zone to evaluate how heterogeneity in sediment textures influences solute residence times in subsurface flow paths. We then use this hydrological insight to explore the implications for nitrate attenuation in a stream corridor heavily influenced by nitrate leached from agricultural soils (Figure 2.1).

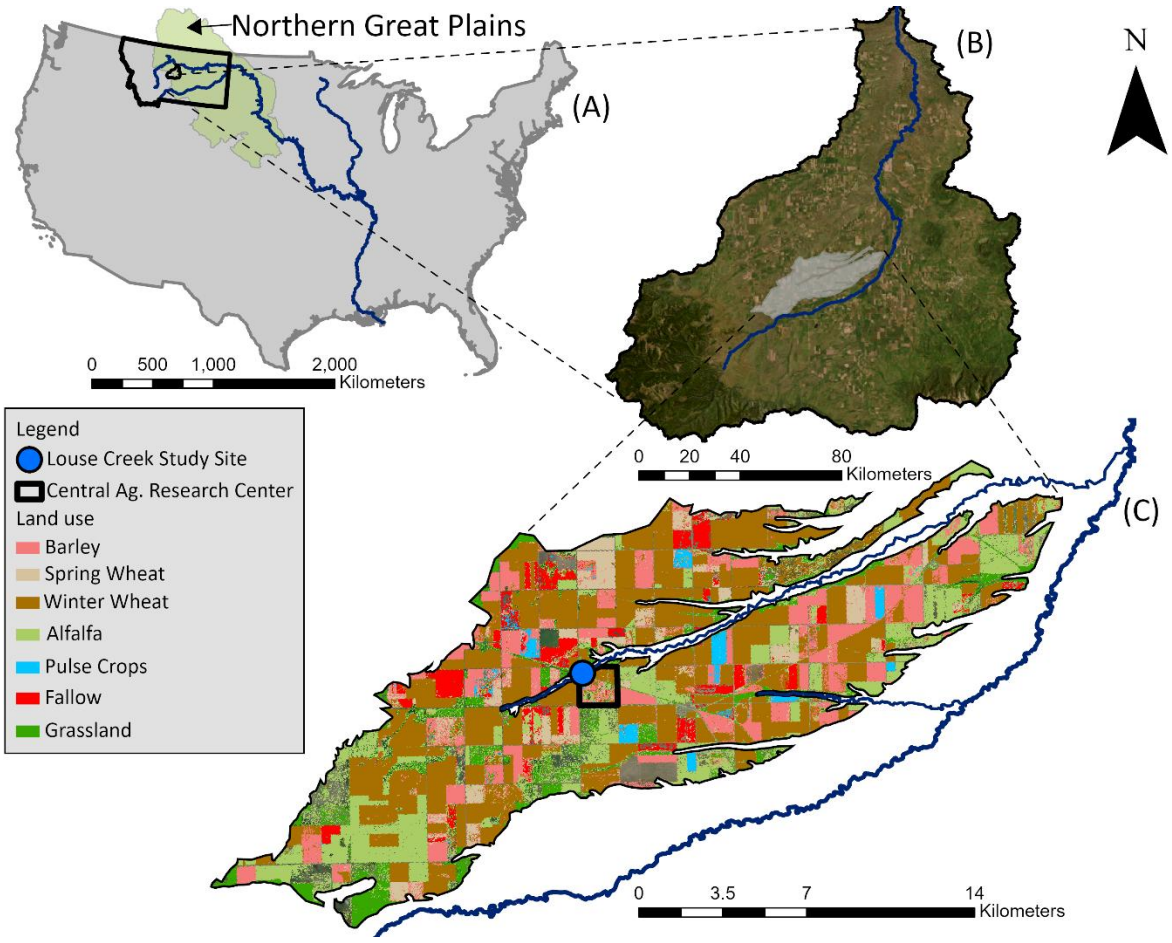


Figure 2.1: Maps and aerial imagery of the study area. (A) Location of the Judith River Watershed within the state of Montana and Northern Great Plains (NGP). (B) The Moccasin Terrace located in the lowlands of the JRW; (C) The Louse Creek stream corridor study site (blue circle) with a color map of terrace land use cover by major crop cultivation in 2022 (United States Department of Agriculture (USDA) National Agricultural Statistics Service (NASS), 2023).

Variation in the stratigraphy of sediment and soils within the shallow riparian aquifers of stream corridors creates a mosaic of hotspots that either promote transport or reducing conditions that facilitate processing of oxidized solutes (Groffman et al., 2009; Naiman & Décamps, 1997; Roley et al., 2012). Zones of transmissive, coarse-textured substrate (sand, gravel, and cobble sized material), provide flow paths for preferential transmission of groundwater through stream

corridors, while fine-textured substrate slows groundwater movement (Angier et al., 2005; Burt et al., 1999). Less transmissive regions, such as natural wetland ecosystems associated with fine-texture materials located closer to the surface (Fisher & Acreman, 2004) tend to supply organic carbon derived from plant productivity, promote oxygen consumption, and facilitate transformation of solutes like nitrate that can serve as terminal electron acceptors for anaerobic microbial respiration. More transmissive regions likely associated with alluvial deposition of coarser substrate (e.g., relict channels) shorten residence times and reduce the potential for long-term anoxia, facilitating more conservative and rapid transport of oxidized solutes like nitrate (Shabaga & Hill, 2010; P. G. F. Vidon & Hill, 2004; P. G. Vidon & Hill, 2006). Thus, hydrologic exchange between coarse-textured aquifer material and fine-textured riparian substrate dictates the extent to which anaerobic processes in the fine sediments determine the bulk biogeochemical behavior of riparian groundwater flow paths (Devito et al., 2000; Hill, 2019; Ranalli & Macalady, 2010; P. Vidon et al., 2010).

Controls on the spatiotemporal distribution of microbially-driven nitrate removal processes in riparian zones are not fully understood due to the complexity of hydrologic exchange processes that may dictate strong gradients in redox couplings. Heterotrophic denitrification is the anaerobic respiration of organic carbon through reduction of nitrate or other oxidized nitrogen species and is thought to be the leading mechanism of irreversible nitrate removal in stream corridors (Cooper, 1990; Haycock & Pinay, 1993; Hill et al., 2000; Verchot et al., 1997; P. G. F. Vidon & Hill, 2004). Other processes that may contribute to nitrate transformation and loss in these environments include non-heterotrophic pathways such as fermentation or chemoautotrophy (Rivett et al., 2008). The source and transport dynamics of

solutes in riparian groundwaters are a strong control on the diversity of microbial communities that ultimately determine the capacity to alter water quality in subsurface flow paths.

Stream corridors draining agricultural areas commonly receive elevated nutrient loading from contaminated upland groundwaters (Tesoreiro et al. 2013). In central Montana, non-irrigated wheat cultivation in the uplands surrounding stream corridors provide an opportunity to study the fate of excess soil nitrate transmitted to riparian groundwaters (Mayernik et al., 2025; Sigler et al., 2018). In this region, nitrate loading to riparian systems from uplands originates from the leaching of mobile solutes from cultivated soils with limited water storage. Nitrate leaching from soils is likely to be exacerbated by the practice of summer fallow, which uses application of herbicides to terminate plant growth over a growing season (Tanaka et al., 2010). This practice simultaneously promotes drainage by gravity under wetter soil conditions and increases soil nitrate abundance by eliminating plant uptake and increasing nitrate mineralization rates (Custer, 1976; John et al., 2017; Sigler et al., 2018). As a result, high nitrate concentration waters accumulated in upland terrace aquifers (~20 NO_3-N mg L^{-1}) ultimately drain to stream corridors, where nitrate concentrations are lowered to varying degrees as determined by varying hydrologic connections among the stream channel, uplands, and riparian subsurface flow paths that promote reducing processes (Mayernik et al., 2025; Sigler et al., 2022) (Figure 2.2). These effects help inform understanding of how human modifications to riparian areas influence nutrient attenuation processes.

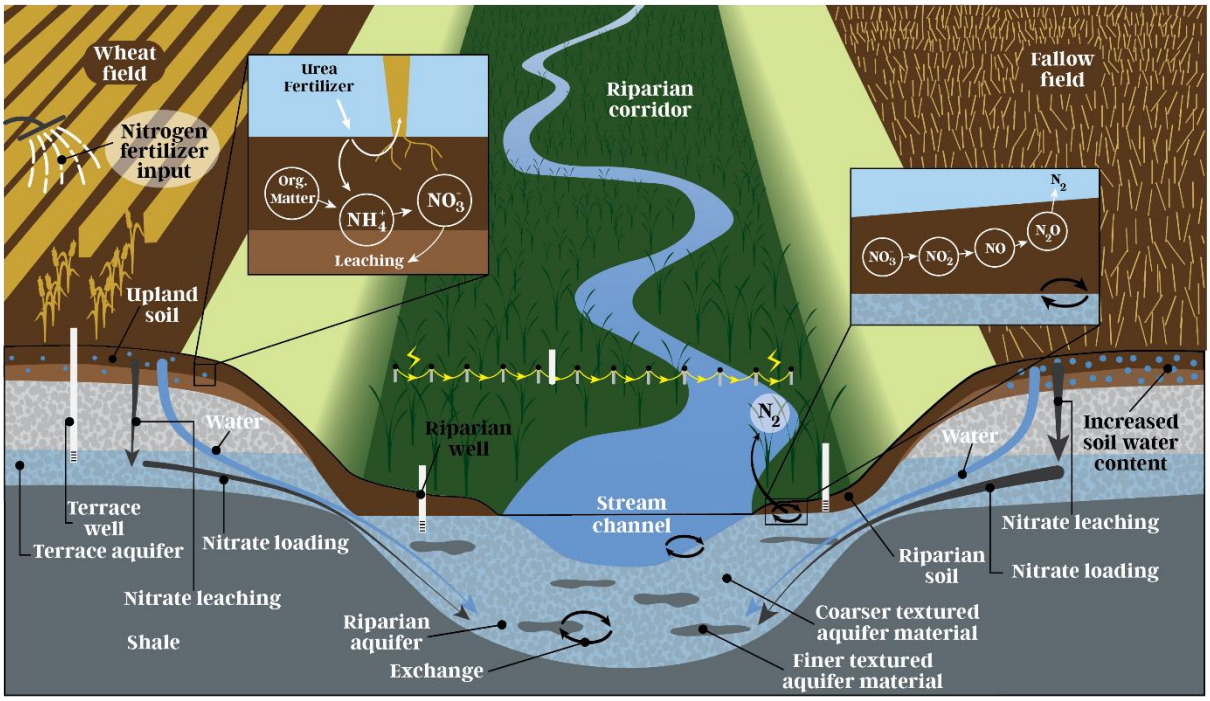


Figure 2.2: Nitrogen movement and processing from uplands to stream corridors in dryland wheat production systems. The diagram depicts mixing and nitrate processing within the stream corridor as water moves through the riparian aquifer. Nitrate concentrations averaging 22.1 NO_3-N mg L^{-1} were observed in the terrace groundwater, 7.32 NO_3-N mg L^{-1} in the stream water, and 1.14 NO_3-N mg L^{-1} in the riparian (Mayernik et al., 2025; Sigler et al., 2018).

This research investigated how the riparian substrate architecture of an unconfined riparian aquifer controls the residence times of advected solutes and thus influences the capacity of riparian flow paths to alter groundwater quality. We used geophysical resistivity surveys and geophysical observations of a salt tracer injection into riparian groundwaters, within a heavily studied stream corridor loaded by chronic nitrate leaching from an agricultural landscape. We define riparian substrate architecture as the physical organization of soil and sediments with varying textures across an unconfined riparian aquifer influencing groundwater movement in these stream corridors. We hypothesize that the extent of coarser riparian substrate controls the

magnitude of groundwater flow through riparian substrate, while the extent of finer textured substrate and its exchange with flow through coarser substrate dictate nitrate attenuation processes along riparian groundwater flow paths (Figure 2.2). We test this hypothesis with three research objectives:

1. Determine the typical variations in hydraulic conductivities, electrical resistivities, and nitrate concentrations of saturated riparian substrates in our study system.
2. Use electrical resistivity tomography (ERT) to characterize the relationship between riparian substrate distribution and the residence time of an introduced conservative and conductive hydrologic tracer.
3. Use numerical experimentation with simple mixing model simulations to explore how variation in substrate texture influences water movement and nitrate attenuation.

The outcomes of these objectives provide insight about the influence of substrate architecture on the fate and transport of nitrate in a riparian aquifer.

2.2. Data and Methods

2.2.1 Study Area

Our study area lies within the Judith River watershed of central Montana, located within a semi-arid agricultural landscape of the Northern Great Plains ecoregion (Figure 2.1A) (P. R. Miller et al., 2002; Padbury et al., 2002). Mean annual precipitation is 391 mm (1991-2020), with the highest monthly precipitation occurring in May and June (totaling 36% of annual) (PRISM Climate Group, 2023). The watershed is a headwater tributary of the Missouri River, with relatively low-relief and low-elevation terrace landforms cultivated primarily for dryland cereal crop production (Figure 2.1C) and with stream corridors draining the terraces used as pasture for beef cattle. Our research is focused on the Moccasin terrace (Figure 2.1C), where 89% of soils are clay loam textures with shallow (20-100 cm) transitions to alluvial gravels with little water storage capacity (Sigler et al., 2018; USDA NRCS, 2021). This landform is

hydrologically isolated from the adjacent little belt mountains, with recharge of the shallow terrace aquifer only from infiltration of precipitation on terrace soils. The annual distribution of precipitation on this cultivated soil combined with fertilizer applications and the practice of summer fallow tend to drive deep percolation of nitrate into the shallow unconsolidated terrace aquifer in the alluvial gravels (1-10m depth to water table) (Figure 2.2) (Sigler et al., 2018; Tanaka et al., 2010). As a result, terrace aquifer nitrate concentrations often exceed 20 NO_3-N mg L^{-1} (Sigler et al. 2018), twice the US EPA regulated maximum for public drinking water sources. High-nitrate terrace groundwater ultimately drains to stream corridors, where nitrate concentrations can be rapidly attenuated by nitrate reduction in riparian groundwater. This attenuation of nitrate tends to result in lower concentrations in stream channels relative to uplands, depending on corridor structure and the fraction of upland water passing through the riparian subsurface before export in the stream (Mayernik et al., 2025; Sigler et al., 2018).

Our study site was a 700-m reach of the stream corridor in the headwaters of Louse Creek, which drains the largest fraction of the Moccasin Terrace surface area before its confluence with the Judith River. Past measurements of stream channel nitrate concentrations at the study site have ranged from 0.69 to 10.47 NO_3-N mg L^{-1} and riparian groundwater nitrate concentrations have ranged from 0.00 to 8.66 NO_3-N mg L^{-1} (Mayernik et al., 2025). Riparian soils in the Louse Creek stream corridor (Figure 2.3B) are poorly-drained, typically hydric, and classified as Aquic Haplocryolls or Cumulic Endoaquolls of the Gallatin and Lamoure series (United States Department of Agriculture, 1953; USDA NRCS, 2021). These soils demonstrate redox conditions associated with persistent saturation from shallow water tables, including sulfur and iron mobilization, and are common throughout the corridors of streams draining the

Moccasin terrace landform (United States Department of Agriculture, 1953; USDA NRCS, 2021). The Louse Creek stream corridor has incised through unconsolidated alluvium on the terrace surface into the bedrock calcareous shales of the Marias River Formation originating from marine sediment deposition during the Cretaceous period (Vuke et al., 2002). Riparian substrate is partially composed of gravels and cobbles originating as alluvium deposited on the terrace and redistributed to serve as the riparian aquifer. Some of the fine-textured soils within the stream corridor likely originate from weathering of shale-derived alluvium generated by stream incision. Fine-textured riparian soils have also likely been augmented by the accumulation of aeolian or alluvial erosion of upland terrace soils, which has likely been magnified by cultivation practices over the last century. This study site allows for assessment of nitrate reduction processes in stream corridor setting influenced by human activities.

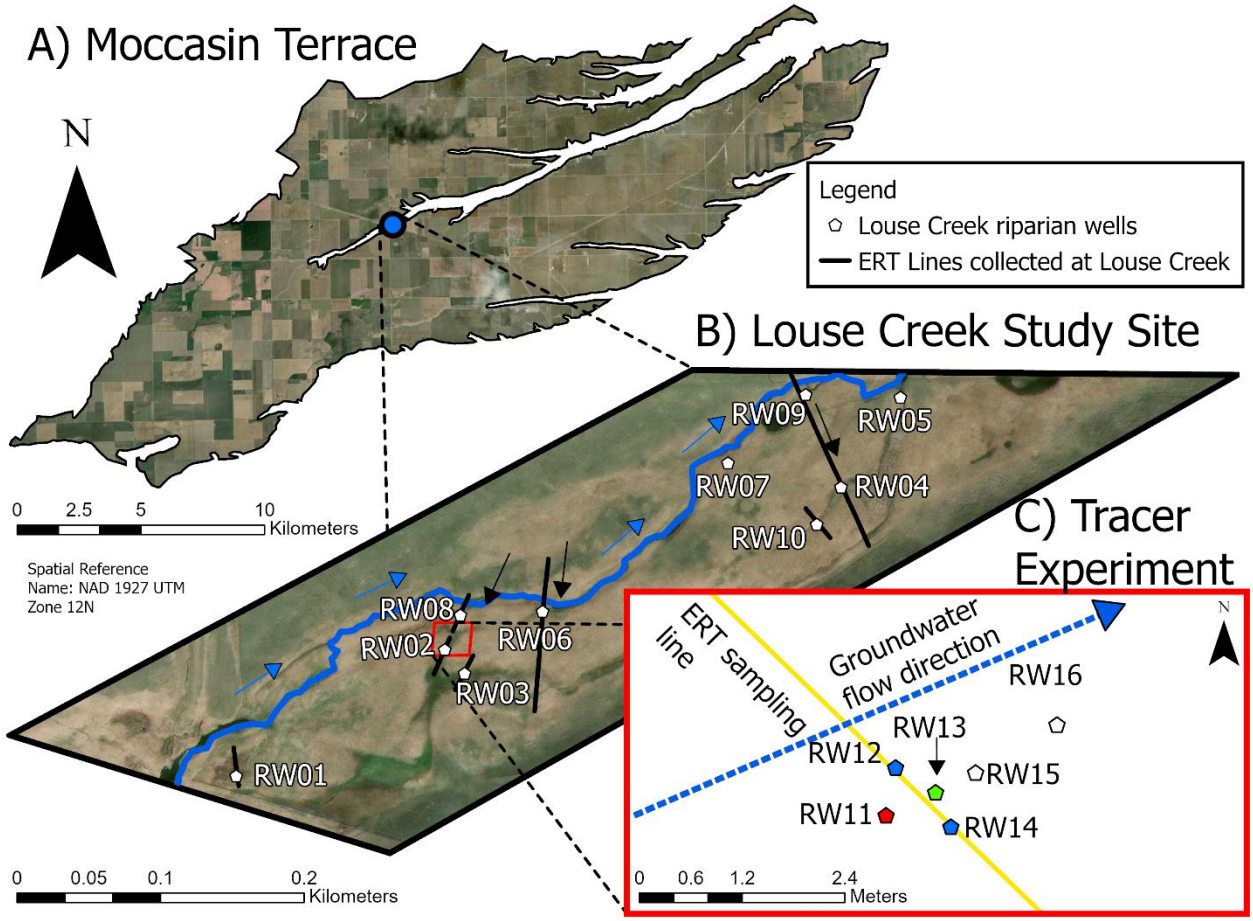


Figure 2.3: Maps and aerial imagery of the study area. (A) Aerial image cropped to the outline of the Moccasin Terrace (strath terrace landform) in the Judith River watershed, including the location of the study site in the headwaters of the Louse Creek drainage (blue circle). (B) Aerial image of the Louse Creek study reach indicating locations of riparian wells (white pentagons with labels), direction of stream flow (blue arrows), tracer experiment area (red box), and initial ERT surveys (black lines, with the black arrows depicting survey direction). (C) Map of the additional wells and electrical resistivity tomography (ERT) transect used for the tracer experiment, where tracer fluid was injected into RW11 (red pentagon), continuously monitored with specific conductivity probes at RW13 (green pentagon), adjacent downgradient monitoring wells RW12 and RW14 (blue pentagon), and further downgradient wells monitored with point measurements of specific conductivity in RW15 and RW16 (white pentagons).

2.2.2 Sampling Well Installation and Groundwater Chemical Analysis

Nitrate concentrations were measured repeatedly (7-24 times from 2021 to 2024) in samples collected from ten shallow riparian wells (<1.55 m, RW01-RW10) distributed

throughout the Louse Creek stream corridor (Mayernik et al., 2025) (Figure 2.3B). We installed six additional wells (RW11-RW16) for this study (Figure 2.3C) and sampled them for water chemistry one to two times during May 2024 in association with the tracer experiment described below. Wells were screened with narrow slots cut through the casing over 30.0 to 53.0 cm from the bottom and were installed at various depths into the riparian substrate using a post pounder applied to a steel drive point bar inserted through the PVC casing (total depth range of 53.8 - 111.5 cm). Wells depths were generally determined by the point of refusal for further insertion of the drive point into the riparian substrate (Table 2.S1).

During well sample collection, dissolved oxygen (DO), temperature, specific conductance, and pH were measured using a Professional Plus Quatro multiparameter probe (YSI Incorporated, Yellow Springs, Ohio). Each sensor was calibrated according to user manual specifications prior to each sampling campaign. Groundwater samples were collected using a peristaltic pump (Geotech Environmental Equipment, Denver, Colorado) and field filtered through a pre-rinsed 0.45-µm capsule filter. Three well volumes of water were purged from the well casings prior to sample collection.

Samples for nitrate analysis were collected into 60-mL HDPE vials, which were rinsed three times with sample water prior to collection and capped with headspace. Samples were kept on ice during transport from the field to the lab and stored in a refrigerator between 2 °C and 4 °C prior to analysis. Nitrate concentrations of samples were analyzed at the Montana State University Environmental Analytical Laboratory (EAL), Bozeman, Montana, on a Lachat QuickChem 8500, within one week of sample collection. Analytical uncertainty ranged from 0.00 to 0.43 NO_3-N mg L^{-1} for individual samples (Table 2.S2).

2.2.3 Saturated Hydraulic Conductivity Values for Sampling Wells

Where possible, saturated hydraulic conductivity values (K_{sat}) were estimated from the rate of recovery of head in the sampling wells described above, reflecting the ability of the substrate surrounding the well screen to transmit water (Amoozegar & Warrick, 2018; Sanchez-Vila et al., 2006). Values were assessed at individual well locations, either through rising-head tests following rapid pumping of water out of the well casing, or through falling-head tests following rapid addition of water to the well casing. Water level was monitored continuously in select wells with pressure transducers (Soloist Levelogger 5LT/5LTC or In Situ Level Troll 200/400). Multiple tests (1-3) were conducted at each well and an average value is reported in Table 2.2. Slug test results were interpreted using the Hvorslev method (Hvorslev, 1951), estimating K_{sat} using a nonlinear least squares model fit to the head recovery curve (NLS). The model assumes that the recovery of water level following an instantaneous displacement will follow an exponential decay curve.

$$H(t) = \exp\left[-\frac{K_{sat}F}{A}\right]t \quad (1)$$

where $H(t)$ is the absolute difference between the head at time t and the static water level, K_{sat} is the hydraulic conductivity (estimated via NLS), F is the shape factor (Cedergren, 1977), A is the cross- sectional area of the well, and t is the time. In these numerical experiments the initial K_{sat} value is set at 0.864 m d^{-1}, and an optimization routine iteratively adjusts K within a bounded range (0.00864 to 86.4 m d^{-1}) using the Horslev model (F = 3), minimizing the residual sum of squares between observed and modeled drawdown until convergence is achieved and further iterations no longer reduce the residual meaningfully. Uncertainty in the estimated hydraulic conductivity was determined from the quality of fit based on the residual variance and sensitivity

of the model to changes of K_{sat}, quantified using a Jacobian matrix, and is reported as a 95% confidence interval.

2.2.4 Characterizing Riparian Substrate Architecture

We used a survey of electrical resistivity tomography (ERT) transects to provide a less invasive and more extensive assessment of the variation in soil textures making up the riparian substrate architecture intersecting select sampling wells. Coarse-textured material with higher hydraulic conductivity and generally higher electrical resistivities may dictate preferential groundwater flow paths (Hester & Fox, 2020; R. B. Miller et al., 2014; Robinson et al., 2008; Rosenberry et al., 2016) and fine-textured material with lower hydraulic conductivity and generally lower electrical resistivity may dictate zones of reducing conditions. We compared the results of ERT surveys with previous groundwater chemistry analyses of well samples and hydraulic conductivities measured in individual wells to extend understanding of the distribution of riparian soil structure and hydraulic properties to the larger spatial scale that determines the overall behavior of the riparian aquifer in modifying water quality (Coscia et al., 2011; Crook et al., 2008; Doughty et al., 2020; Singha et al., 2008).

ERT is a geophysical technique that involves passing a known low frequency alternating current through successive pairs of electrodes that are typically inserted into the ground surface along a transect or grid. While the known current is being applied to a given pair of electrodes, the instrument measures and records the resulting differences in electrical potential (i.e., voltages) in the sediment between other pairs of electrodes in the array. These detailed responses of the sediment to electrical stimulation ultimately provide spatially extensive data sensitive to substrate composition, water content of pore space, total dissolved solids in pore water, and

temperature (Cardenas & Markowski, 2011; Coscia et al., 2011; Rein et al., 2004; Robinson et al., 2008; Singha et al., 2008; L. D. Slater et al., 2010). However, spatially explicit perspectives on subsurface electrical resistivity require further analysis of current and voltage data using model inversions.

ERT data were recorded using a SuperSting R8 meter, during June 2022 and June 2024. ERT surveys across the study site were conducted at seven different locations across the Louse Creek stream corridor, targeting cross sections of presumed groundwater flow paths through an area with a riparian well location (Figure 2.3B). All measurements were recorded using a dipole-dipole array geometry and 28 electrodes per line at 1-m and 2-m spacing. Individual surveys lasted roughly 20 minutes, with inverse reciprocal measurements recorded during each run. The locations of ERT instrument electrodes were geo-referenced using the Reach RS2+ multiband RTK GNSS receiver. All electrode positions were recorded with this instrument to allow inferred ERT images to be mapped and interpreted in the context of well locations and study site features.

The raw current and voltage data measured by the ERT instrument were fit with an inversion of a 2-dimensional electrical current model based on Ohm's Law to infer a continuous 2-dimensional profile of electrical resistivity along a given transect. Inference of each ERT profile image is thus based on a deterministic Tikhonov inversion algorithm (G. Blanchy et al., 2020) conducted using ResIPy software (Binley & Kemna, 2005; G. Blanchy et al., 2020) based on the R2 (v4.10) model that accounts for two-dimensional electrical current flow in a triangular mesh. All datasets were filtered to remove measurements with an associated reciprocal error value >4% using an alpha weight of 0.01 and a beta weight of 0.02 during their processing. ERT

profile images were corrected for surface topography based on the locations and elevations of electrodes.

Inverted ERT images were sub-categorized into four different classes using a K-means clustering algorithm applied to inverted resistivity values. Four groups were decided for this clustering analysis to encompass our presumed geologic units of intact shale bedrock / shale derived alluvium, two groups of transitional aquifer material, and coarse textured aquifer material. This algorithm categorizes individual inverted ERT cells into one of four clusters such that differences between the resistivity values of cells in each cluster are minimized. The optimal clusters are identified by initializing random centroid values for each cluster, categorizing all data points to fit into each group, and iterating recategorization of the data relative to the means calculated from the previous realization of the clusters until the means remain relatively consistent between successive iterations (within some defined tolerance of convergence). Datasets from seven separate ERT surveys (Figure 2.3, 2.S1-2.S6) were assessed together to determine the best-fit clusters, from a count of 5,928 inverted cells. Figure 2.S1-2.S6 display six of the seven surveys used for the clustering analysis, with figures 2.S2 and 2.S5 representing sections of an individual line used in this process.

2.2.5 Tracer Experiment

An area of increased subsurface resistivity values, suggesting generally coarser substrate, was targeted for a riparian aquifer tracer experiment. The experiment was intended to capture the nature of solute dynamics in a higher conductivity flow path, presumed to be influenced by exchange with zones of lower connectivity sediments. Injectate for the experiment was prepared by dissolving 24.19 kg of NaCl in 302 liters of water. The injectate was them pumped into

riparian well RW11 at a rate of 1.24×10^{-5} m^3 s^{-1} over 6.8 hrs on 30 May 2024 (Figure 2.3C). A relatively steady load of 3.56 kg NaCl h^{-1} was thus introduced to the riparian aquifer over the period of the injection.

The response of the groundwater flow path to the tracer injection was continuously monitored in four wells (RW02, RW11, RW13, RW14) using specific conductivity and water level measurements from Solinst Levelogger 5 LTC and In-Situ Level Troll 200 data loggers (Solinst, Georegetown, Ontario CA and In-situ, Fort Collins, Colorado). All loggers were calibrated according to owner manual specifications prior to installation. RW11 was the injection well, RW13 was the primary observation well presumed to be closest to the center of the flow path, and RW14 was a secondary observation well apparently further from the center of the flow path. RW02 was a control well not influenced by the injection, and was monitored to identify any changes in aquifer conditions that may confound interpretation of the tracer data. Loggers recorded measurements at a one-minute interval during the first 24 hrs of the tracer experiment and then recorded measurements every 15 minutes until monitoring ended on 10 June 2024. Additional point measurements of specific conductivity were recorded at wells RW12, RW15, and RW16 using a handheld YSI Professional Plus Quatro multiparameter probe, which was calibrated the morning of the experiment. The tracer injection resulted in specific conductivities and associated probe uncertainty (± 0.5% of reading + 1 μS cm^{-1}) up to 69,427 ± 348 μS cm^{-1} at the primary observation well, which was dramatically higher than the riparian groundwater level measured before the tracer test (ca. 994 μS cm^{-1}) and indicated an influence on groundwater conductivity, increasing the groundwater ion content, which was easily detectable with the ERT device. Conductivity in the tail of the breakthrough curve at the downstream well appeared to

return to a stable level of 1,201 ± 7 μS cm^{-1} after 11.3 days (271.2 h). This value was still higher than observations at RW02 (1,148 ± 7 μS cm^{-1}), suggesting residual tracer or enhanced release of solutes due to the experiment.

Additionally, the tracer plume was observed using repeated ERT time-lapse images at an experimental transect, to track the residence time of the highly conductivity groundwater plume introduced to the riparian flow paths. The tracer plume was observed using ERT at a location 0.5 meters downgradient from the injection well. The electrode transect was laid out along a 14-meter survey line intersecting wells RW12-RW14 (Figure 2.3C), presumed to be approximately perpendicular to the direction of groundwater flow. The injection of the high-conductivity NaCl solution increased the bulk conductivity of the subsurface along the flow and thus the residence time of the tracer at a cross-section in the flow path could be observed using time-lapse ERT imagery (Doughty et al., 2020; Ward et al., 2010b, 2010a). Time-lapse resistivity provided useful spatial context for the position of the plume relative to point observations (Doughty et al., 2020; Ward et al., 2010a, 2010b). ERT data were recorded using a dipole-dipole array geometry at 0.5 m spacing. A total of 13 ERT images were collected over a 26 hr-window following the beginning of the tracer experiment, including a baseline image collected one hr prior to the start of the injection. All model inversions for ERT imagery followed the same protocols as described above for ERT surveys. Differences between each ERT image collected throughout the tracer experiment and the baseline conductivity before the injection were calculated using time-lapse survey methods within the ResIPy software.

The head monitored by the pressure transducer in the injection well increased while the tracer fluid was injected and rapidly returned to static water level pre-injection conditions after

the pump was deactivated. The change in hydraulic head was incorporated into calculated rates of Darcian water movement during the experiment, based on the average head gradient imposed during the injection period. This approach presumes that the water level in the well casing reflected the influence of the injection on the hydraulic head in the aquifer. The ambient head gradient was used for Darcy flow calculations during the post-injection period. The difference in elevation between the tops of the risers for the injection well (RW11) and the central monitoring well (RW13) was measured with a spectra precision LL1505C laser level, allowing calculation of head gradients from depth to groundwater measurements relative to the top of the riser.

Mean residence time (τ_{TF}) of the tracer fluid was calculated from an approximation of the probability density function of the residence time distribution.

$$\tau_{TF} = \int t \cdot \left(\frac{SC(t)}{\int SC(t)dt} \right) \cdot dt \qquad (2)$$

where $SC(t)$ is specific conductivity at a given time during the breakthrough curve (presumed to be conservative and linear with NaCl concentration) (Figure 2.S8), t is the time of a given specific conductivity measurement. Specific conductivity values were corrected to remove baseline groundwater conductivity before calculation. We assume this approximates the mean residence time in the groundwater flow path because the tracer injection was short relative to the total duration of the breakthrough curve.

2.2.6 Evaluating the Influence of Substrate Texture on Tracer Plume Dynamics

2.2.6.1 Model Design We simulated the fundamental nature of groundwater solute residence time in heterogeneous media using a simple two-component mixed reservoir model to assess the potential influence of bimodal substrate texture on observed tracer behavior. These

simulations were based on a simplification that the observed breakthrough curve of specific conductivity (μS cm^{-1}) observed at well RW13 was indicative of a mixture of water and tracer that spent time in distinct volumes of coarser and finer sediments. The specific conductivity response at RW13 was chosen for comparison to the model because it has continuous data that apparently falls near the center of the plume, based on comparisons with ERT data and observations at RW12 and RW14.

The model conceptualizes the substrate between the injection well RW11 and monitoring well RW13 as being composed of two distinct regions of differing texture, where the cross-sectional area or volume of the associated flow path is divided between a fraction of fine material (f_F) and a fraction of coarse material (f_C). Each of these coarse and fine regions are receiving water influenced by the injection according to the magnitude of flow through that region, and water measured at RW13 is assumed to represent a mixture of flows that are output from these regions. For the simple thought exercise within the scope of this effort, each region is represented as a contiguous well-mixed volume. The model assumes steady state flow for a given head gradient and calculates a Darcy flux through finer (J_F) and coarser (J_C) regions of the substrate.

$$J_C = K_C \cdot \frac{\Delta H}{\Delta L} \tag{3a}$$

$$J_F = K_F \cdot \frac{\Delta H}{\Delta L} \tag{3b}$$

where K_C and K_F are the hydraulic conductivity of coarser and finer sediments[L T^{-1}], ΔH is the change in head between the injection and observation wells in[L], and ΔL is the distance between the two wells (0.52m) [L]. The simulation assumes a higher average head gradient during the injection based on the measured water levels in the injection and observation wells and then

assumes the ambient head gradient after the termination of the injection. Flow (Q,[L^3 T^{-1}]) through the mixed volume of a given texture is based on its relative contribution to the total cross-sectional area (19.95m^2) ($f_C = A_C/A_T$, $f_F = A_F/A_T$, $f_C + f_F = 1$).

$$Q_C = J_C \cdot f_C A_T = J_C \cdot A_C \tag{4a}$$

$$Q_F = J_F \cdot f_F A_T = J_F \cdot A_F \tag{4b}$$

Assuming the total mass of tracer injected (M_I) was relatively evenly distributed over the injection time (t_I), the tracer concentration input to the model is the ratio of the tracer load to the total flow through the coarse and fine substrate ($Q_T = Q_F + Q_C$).

$$C_I = \frac{\left[\frac{M_I}{t_I}\right]}{Q_T} \tag{5}$$

The effective mass (M_C, M_F) and concentration (C_C, C_F) of NaCl in the volume associated with each substrate texture is calculated at a given time (t) using a mixing model.

$$C_C(t) = \frac{M_C(t)}{V_C} = \frac{\left(C_C[t-1]V_C + (C_I\, Q_C \Delta t) - (C_C[t-1]Q_C \Delta t)\right)}{V_C} \tag{6a}$$

$$C_F(t) = \frac{M_F(t)}{V_F} = \frac{\left(C_F[t-1]V_F + (C_I\, Q_F \Delta t) - (C_F[t-1]Q_F \Delta t)\right)}{V_F} \tag{6b}$$

where V_C and V_F are the volume of pore water in the coarse and fine textured volumes. Another mixing model can then be used to calculate the concentration in the mixture of flows output from the coarse- and fine-textured volumes (C_A).

$$C_A[t] = f_{QC} C_C[t] + f_{QF} C_F[t] \tag{7}$$

where $f_{QC} = Q_C/Q_T$ and $f_{QF} = Q_F/Q_T$ represent the fraction of flow through the coarse and fine textured material.

2.2.6.2 Converting ERT Images and Observation Well Specific Conductivities to Average Concentrations We recognize that our simplified model is not likely to directly represent the observed concentrations in the RW13 well, because the tracer is not truly fully mixed with the aquifer volume and thus not distributed evenly across the plume. To estimate an observed tracer breakthrough curve more comparable to our model, we calibrated changes in ERT near the well to changes in concentration observed in the well, then used that calibration with the average change in ERT across the full extent of the plume to estimate the average change in concentration across the plume that is more conceptually comparable to our fully mixed model output. This strategy was inspired by previous efforts to use ERT images to calculate NaCl concentrations for the purposes of comparisons with solute transport models (Wagner et al., 2013).

First, we used a segmented regression to empirically characterize the relationship between the increase in conductivity measured in RW13 and RW14 wells and the corresponding average change in resistivity of the ERT imagery pixels overlapping the well screens (Figure 2.S7). This model allowed conversion of the change in resistivity from the differenced ERT to estimates of the change in specific conductivity of the pore water across the imaged plume. We used the linear relationship between specific conductivity and NaCl concentration (Figure 2.S8) to convert the distribution of pore water specific conductivity to a distribution of tracer concentrations. This calibration was developed by measuring a wide range of known NaCl concentrations with the Level Troll 200 data logger used during the tracer test. Finally, area-

weighted average tracer concentrations derived from each of the ERT images of the plume were regressed against the corresponding tracer concentrations in the well (Figure 2.S9). This linear regression was used to convert the high-frequency specific conductivity measurements from RW13 into an approximate high-frequency breakthrough curve of the plume-averaged tracer concentrations, which is more likely to be comparable to breakthrough curves predicted by our simplified model.

2.2.6.3 Model Uncertainty and Sensitivity Analysis We used a Monte Carlo approach to assess the propagation of uncertainty from the conversion of ERT images to a breakthrough curve of average concentration. First, an ensemble of 1,000 realizations of the average concentration across the plume were created based on the uncertainty in the standard error values for the segments of the segmented regression (Figure 2.S7). Then, a second ensemble of 1,000 realizations of the conversion from specific conductivity to a NaCl concentration were created, incorporating the standard error from their linear fit (Figure 2.S8). We randomly sampled from each of these ensembles to create 1,000 realizations representing the compounded uncertainty in the conversion from continuously measured specific conductivity values at the downgradient observational well to an average aquifer NaCl concentration. The 2.5% and 97.5% quantile of the Monte Carlo ensemble of regression slopes were used as bounding boxes constraining 95% confidence intervals on our plume-average breakthrough curve (Figure 2.S9).

We conducted a sensitivity analysis to evaluate the influence of the hydraulic conductivity of the coarse and fine substrates (K_C, K_F) and relative abundance of each substrate (f_C, f_F) on the model responses. The analysis used the range of observed hydraulic conductivity values based on slug tests in the 13 riparian wells to constrain K_C and K_F values. We conducted

5,000 simulations, randomly sampling values from uniform distributions acro**ss** defined parameter ranges: K_F (0.085–0.90 m d^{-1}, step = 0.005), K_C (2.5–35 m d^{-1}, step = 0.1), and f_C (0.01–0.99 m^3 m^{-3}, step = 0.01). We selected 2,500 of the simulations that were more similar to our observed data based on an aggregated log-likelihood (Figure 2.9C). The total log-likelihood ($logL_T$) score for a given simulation was calculated using a sum of logged probability densities determined by the model fit relative to the uncertainty in the data.

$$L_{log,T} = \sum_{t=1}^{n} log\left[\frac{1}{\sqrt{2\pi}\sigma_t} exp\left(-\frac{\left(C_{O,t} - C_{S,t}\right)^2}{2\sigma_t^2}\right)\right] \quad (8)$$

where C_O is the concentration value of the observed response curve at RW13, C_S is the concentration value of the simulated response, and t is the timestep. The standard deviation for the likelihood calculation was aligned with the uncertainty in the observed breakthrough curve, such that the 95% confidence corresponded to 2σ around the mean.

$$\sigma_t = \frac{C_{HU,t} - C_{LU,t}}{4} \quad (9)$$

where $C_{HU,t}$ and $C_{LU,t}$ represent the bounds of the 95% confidence in concentration at a given time of measurement.

Selection of a given combination of parameters influenced the total simulated volumetric flow and thus the overall dilution effect on the breakthrough curve concentrations of introduced tracer. To focus on comparisons of relative residence times, independent of dilution effect, we compare simulated and observed breakthrough curves normalized to their peak concentration ($C_{,norm,t} = \frac{C_t}{\max(C_t)}$), for the 2,500 simulations in agreement with the observed average response curve uncertainty window. This allows for comparison of the shape of the normalized simulated responses ($C_{S,norm,t}$), that fit our uncertainty window, with the shape of the normalized observed

breakthrough curve at RW13 ($C_{O,norm,t}$), by calculating the residual sums of squares between the two. From this analysis, we identified the simulation that best matched the normalized breakthrough curve, as well as the 2.5th percentile of the closest fits (n = 63), based on the smallest residual sum of squares.

2.2.6.4 Simulating Nitrate Attenuation Previous work on streams draining the Moccasin Terrace has provided evidence that nitrate attenuation is higher and more consistent in substrates where sampling wells were completed in lower conductivity and presumably finer textured materials (Mayernik et al., 2025). We therefore explore the biogeochemical consequences of the hydrologic models described above based on nitrate removal occurring exclusively within fine textured substrate. The fraction of nitrate remaining after passing through the fine-textured substrate was assumed to be a function of a first-order rate constant k_F applied to a well-mixed volume of pore water with turnover time $\tau_F = V_F/Q_F$.

$$f_{N,F,ss} = \frac{1}{k_F \tau_F + 1} \tag{10}$$

We used a range of values for k_F based on published nitrate consumption values (Marzadri et al., 2012; Ocampo et al., 2006; Reinhold et al., 2025), a baseline scenario of ($k_F = 1.39\times10^{-5}\,s^{-1}$), as well as values one order of magnitude lower ($1.39\times10^{-6}\,s^{-1}$) and higher ($1.39\times10^{-4}\,s^{-1}$).

Assuming nitrate is processed only in the fines, the fraction of nitrate remaining due to overall processing by aquifer was calculated using a steady-state mixing model based on the fraction of flow moving the fine and coarse substrates. Furthermore, the fraction of nitrate

remaining after passing through the combined aquifer can be related to an effective rate constant k_A and turnover time $\tau_A = V_A/Q_A$ for the whole system.

$$f_{N,out} = f_{QF} f_{N,F,ss} + f_{QC} = \frac{1}{k_A \tau_A + 1} \tag{11}$$

We then rearranged equation 11 to calculate the effective first order rate constant k_A.

$$k_A = \frac{1 - (f_F f_{N,F,ss} + f_{QC})}{(f_F f_{N,F,ss} + f_{QC})\tau_A} \tag{12}$$

To explore the potential role of fine sediments in processing nitrate at our field site, we compare the simulated range of $f_{N,out}$ values for different scenarios of k_F to the apparent nitrate consumption between the upgradient well RW11 and downgradient wells RW12 and RW13. The sample collected at RW14 was omitted from this analysis because it did not fall in the center of the tracer plume.

2.3. Results

2.3.1 Saturated Hydraulic Conductivities and Nitrate Concentrations in Riparian Wells

K_{sat} values varied widely across the stream corridor study wells, ranging from 0.0400 ± 0.0002 m d^{-1} to 34.3 ± 2.8 m d^{-1} (Figure 2.4, Table 2.1). Uncertainty values represent 95% confidence interval established based on the K_{sat} model residual variance and sensitivity. The highest K_{sat} value at the Louse Creek study site (34.3 ± 2.8 m d^{-1}) was observed in aquifer recovery tests at RW01, located in a local topographical depression roughly 35 m from the primary creek channel (Figure 2.3B) at the upstream end of the study reach. The lowest assessed K_{sat} at Louse Creek was at RW07 (0.0400 ± 0.0002 m d^{-1}), located in a remnant stream channel, roughly seven

meters on the shortest path to the primary creek channel (Figure 2.3B). All observed K_{sat} values were grouped into high and low categories, with a threshold at 1.0 m d^{-1}, as this number signified the transition between fast (unable to drain well at maximum pumping rate of geopump) and slow (can drain) production riparian wells observed while in the field. The injection and observation wells fell within the "higher" grouped values (>1.0 m d^{-1}) (Figure 2.4), consistent with the reasoning behind the choice of location of the tracer experiment.

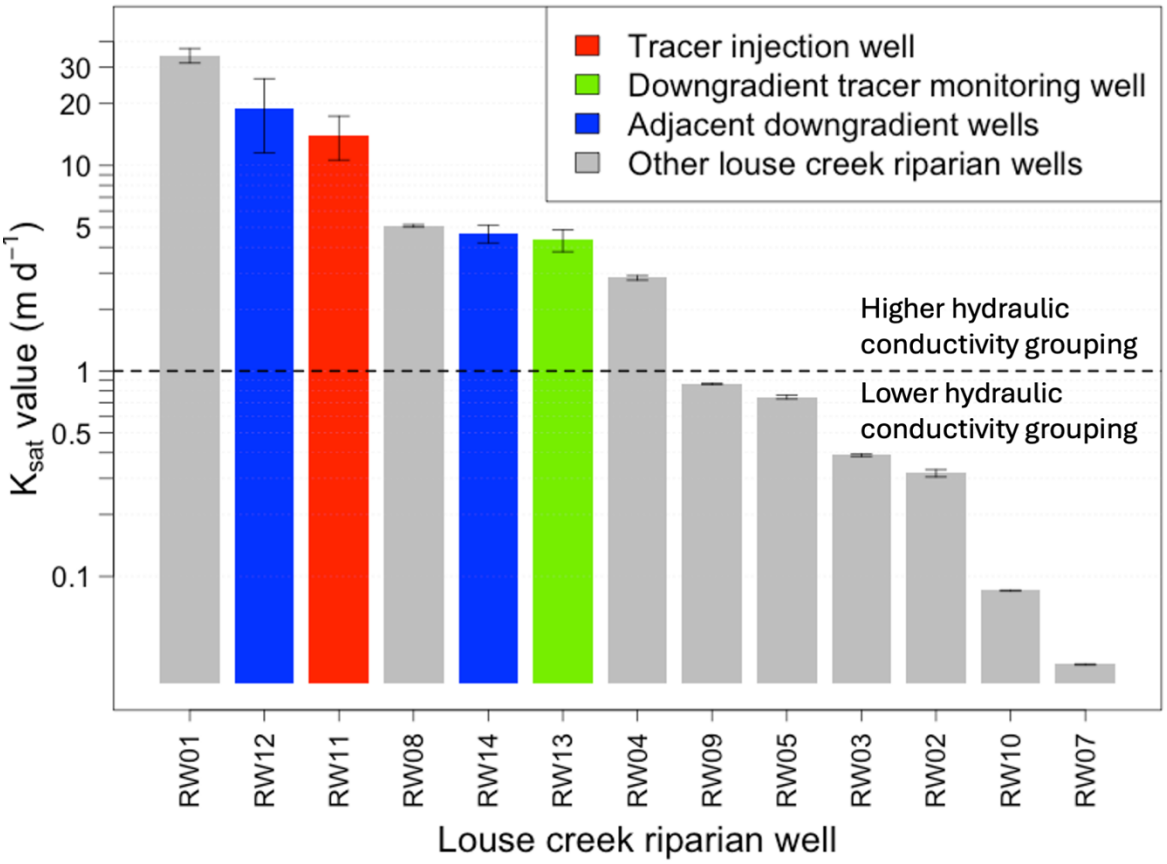


Figure 2.4: Hydraulic conductivity values (log scale) estimated from aquifer recovery tests in riparian wells in the Louse Creek stream corridor. Colored bars indicate wells used for the tracer injection (red, RW11), the central observation of the tracer plume (green, RW13), and lateral positions on the tracer plume (blue, RW12 and RW14). K_{sat} values of wells are categorized as

"higher" and "lower" values, separated at 1 m d^{-1} (dashed line). Error bars represent uncertainty in the predicted saturated hydraulic conductivity value based on the modeling fitting process.

Nitrate concentrations were variable among well locations and sampling dates over five years of monitoring in the Louse Creek stream corridor (Table 2.1, Table 2.S2). Well RW01 consistently showed the highest mean nitrate concentration for an individual riparian well (5.99 ± 0.30 NO_3-N mg L^{-1}, n=14), and well RW02 consistently showed the lowest nitrate concentration (0.003 ± 0.016 NO_3-N mg L^{-1}, n=7). Individual well nitrate uncertainty values (Table 2.1) represent the average analytical uncertainty value of a wells individual samples, with analytical uncertainty estimated as 5% of the reported value for concentrations above quantitation limit (value of lowest standard run on instrument), 10% of the reported value for concentrations below the quantitation limit but above the detection limit (three times the standard deviation of all blank measurements), and for responses below the detection limit, the reported value was set to the detection limit, (Mayernik et al., 2025). All wells except RW01, RW11-RW14, and RW16 had concentrations close to zero (<0.15 NO_3-N mg L^{-1}) on at least one occasion, with wider ranges seen in RW01, RW04 and RW08. These three wells were also sampled more often than the other wells (n=14-24) (Table 2.S2), and include 15 samples collected during months when samples were not collected at the lower-K_{sat} wells (August-December).

Table 2.1: Saturated hydraulic conductivity (K_{sat}, m d^{-1}), bulk electrical resistivity (Ω m) of ERT image cells overlapping the well screening, and nitrate concentration (NO_3-N mg L^{-1}) in 16 riparian well locations within the Louse Creek stream corridor. K_{sat} values were assessed with well recovery tests during June of 2022 (RW01-RW10) and May of 2024 (RW11-RW16). Data for ERT images were collected in June of 2022 and 2024. Samples for nitrate analysis were collected during March-December, 2021-2024. Nitrate concentrations include results for wells RW01-RW10 reported in Mayernik et al., 2025. Wells RW11-RW16 were installed and sampled in June of 2024.

Well	K_{sat} (m d^{-1})		Resistivity (Ω m)			Nitrate (NO_3-N mg L^{-1})					
	Value	Uncert	n	Mean	SD	n	Mean	Uncert	SD	Min	Max
RW01	34.27	2.76	7	36.0	9.1	14	5.990	0.299	2.264	1.787	8.664
RW02	0.32	0.013	6	28.5	7.8	7	0.003	0.016	0.009	0.000	0.023
RW03	0.39	0.005	5	25.2	4.5	4	1.011	0.051	0.924	0.113	2.027
RW04	2.84	0.07	7	47.3	10.3	24	1.566	0.103	1.810	0.000	5.924
RW05	0.75	0.02	NA	NA	NA	4	0.019	0.019	0.030	0.000	0.063
RW06	NA	NA	NA	NA	NA	8	0.401	0.020	0.499	0.026	1.284
RW07	0.04	0.0002	NA	NA	NA	7	0.008	0.019	0.020	0.000	0.054
RW08	5.09	0.07	7	48.1	3.7	23	3.211	0.161	1.579	0.025	6.011
RW09	0.86	0.007	NA	NA	NA	7	0.019	0.016	0.028	0.000	0.071
RW10	0.09	0.0003	6	26.8	5.2	7	0.368	0.035	0.973	0.000	2.574
RW11	13.99	3.37	NA	NA	NA	1	2.737	0.137	NA	NA	NA
RW12	18.94	7.43	19	67.6	30.5	1	2.021	0.101	NA	NA	NA
RW13	4.34	0.54	14	91.2	26.1	1	3.167	0.158	NA	NA	NA
RW14	4.66	0.46	14	88.8	30.0	1	3.619	0.181	NA	NA	NA
RW16	NA	NA	NA	NA	NA	2	2.348	0.117	0.373	2.084	2.612

Nitrate concentrations were more likely to be higher in the wells completed in higher K_{sat} substrates (n=65), with an average concentration and an average analytical uncertainty of 3.18 ± 0.17 NO_3-N mg L^{-1} in the higher conductivity substrate, relative to an average nitrate concentration and average analytical uncertainty of 0.19 ± 0.02 NO_3-N mg L^{-1} in the lower

conductivity substrate (Figure 2.5). A non-parametric Kolmogorov-Smirnov test suggests high confidence (p-value < 0.001) that the samples of nitrate concentrations from the two different categories of substrate hydraulic conductivity were not from the same distribution.

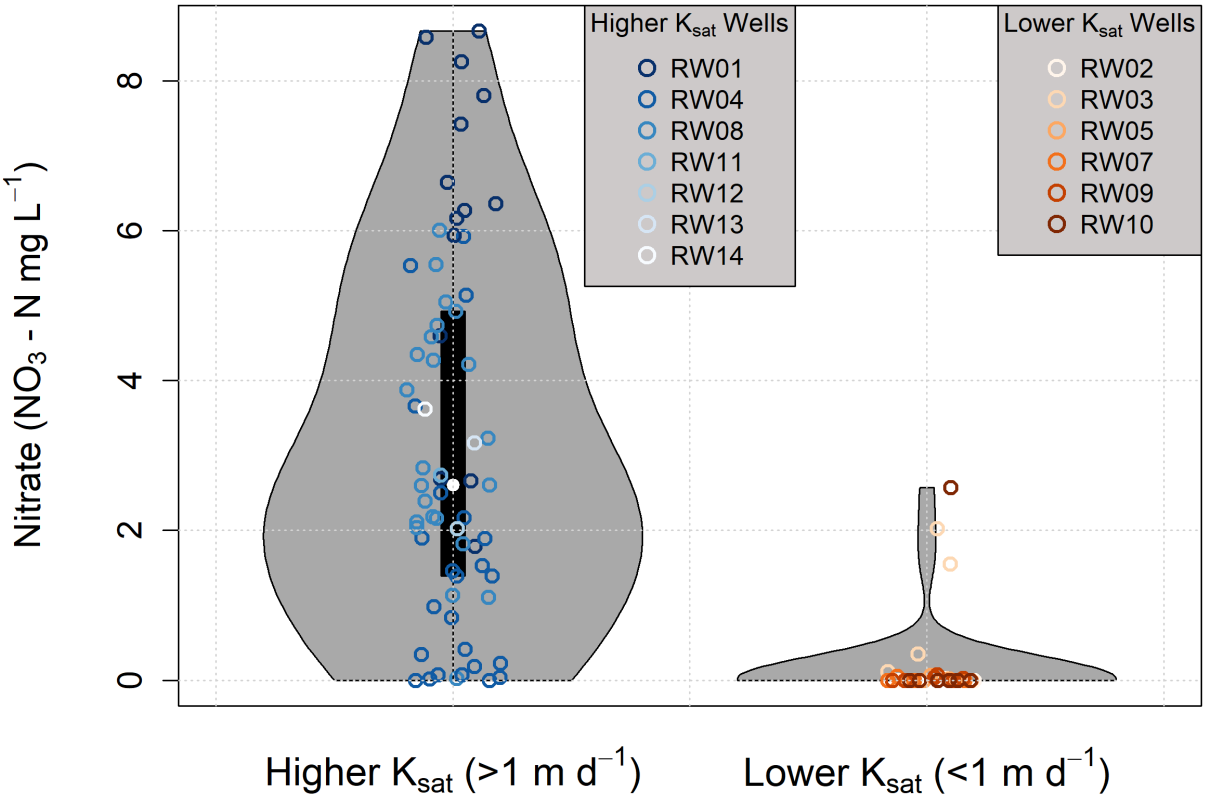


Figure 2.5: Nitrate concentrations in Louse Creek riparian wells categorized by higher K_{sat} (>1 m d^{-1}; blue points) and lower K_{sat} (<1 m d^{-1}; brown points) values. The saturation of the point color indicates a sample from a given riparian well. The internal black box is bounded vertically by the first and third quartile values, while the white dot represents the median value, and the plot width indicates frequency of observations. RW15 and RW16 were excluded from analysis due to no assessed K_{sat} value.

2.3.2 Electrical Resistivity Tomography (ERT) of Riparian Substrate

ERT imaging of subsurface architecture within the stream corridor demonstrated a distribution of resistivity values that suggests different substrate types comprising the substrate

architecture of the riparian area (Figure 2.6). Generally, the spatial distribution of the lowest-resistivity cluster from our analysis suggests areas dominated by fine textured material – either intact shale or shale-derived alluvium (mean resistivity of 23.4 Ω m). The highest-resistivity cluster, suggesting coarse textured aquifer material, also demonstrated the most variability, with a mean resistivity of 66.9 Ω m, a range of 72.9 Ω m, and a max of 130.2 Ω m (Table 2.2, Figure 2.6). The middle clusters with intermediate resistivity (mean resistivity of 35.8 Ω m and mean resistivity of 47.8 Ω m) appeared to be associated with transitional or mixed zones between the highest and lowest resistivities. Resistivity values representative of the cluster with the lowest values found deeper than 2 m in the substrate would be consistent with the shale bedrock into which the stream corridor is incised (Figure 2.6).

Table 2.2: Summary statistics of electrical resistivity categories resulting from a K-means sorting into four clusters. Source data for the analysis were from ERT transects collected at riparian wells RW01, RW02, RW03, RW04, RW06, RW08, RW09, and RW10.

K-means Cluster	**Resistivity (Ω m)**					
	n	**Mean**	**SD**	**Min**	**Max**	**Range**
1	1723	23.4	4.1	10.1	29.6	19.5
2	2119	35.8	3.4	29.6	41.8	12.2
3	1504	47.8	4.4	41.8	57.3	15.5
4	582	66.9	9.3	57.3	130.2	72.9

At riparian well RW04 and RW08 (Figure 2.6A,B), the depth of the well screens aligned with material in K-means clusters 3 and 4, indicating interaction with more electrically resistive substrate that would be consistent with coarser substrate. At RW03 and RW10 (Figure 2.6C,D) the depths of the well screening align with material that cluster with lower resistivities, which would be consistent with interactions with finer textured materials.

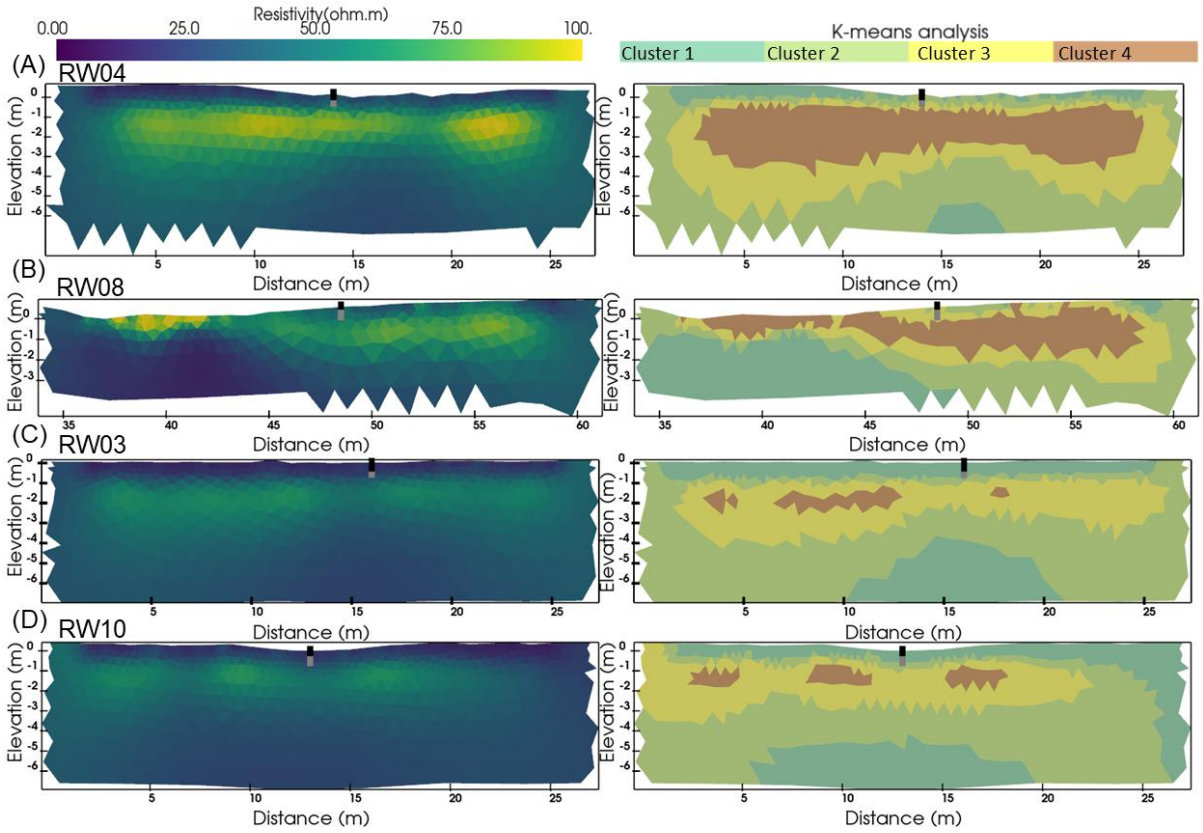


Figure 2.6: Subsurface resistivity values (left) and zones with common resistivity values based on K-means clusters of ERT data (right) at transects intersecting four different riparian well locations within the Louse Creek stream corridor. Each transect includes the location of a well (black vertical bar; (A) RW04, (B) RW08, (C) RW03, and (D) RW10), with the well screen presented as a grey vertical bar. Clustering thresholds are provided in Table 2.1.

2.3.3 Tracer Test

The specific conductivities monitored in downgradient wells (RW12, RW13, RW14, RW15, and RW16) (Figure 2.3C) were clearly influenced by the tracer-induced increase in conductivity in the injection well (RW11, Figure 2.7). Among the downgradient wells, RW13 responded earliest and reached the highest specific conductivity values, with a peak value of 69,427 ± 348 μS cm^{-1}, with uncertainty reflecting probe accuracy. RW14 had a slower and weaker response to the tracer injection, with a maximum specific conductivity of 31,113 ± 157

µS cm^{-1}. Specific conductivity values remained at ambient levels (ca. 800 µS cm^{-1}) in the upgradient monitoring well (RW02), representing relatively static baseline specific conductivity values during the tracer experiment.

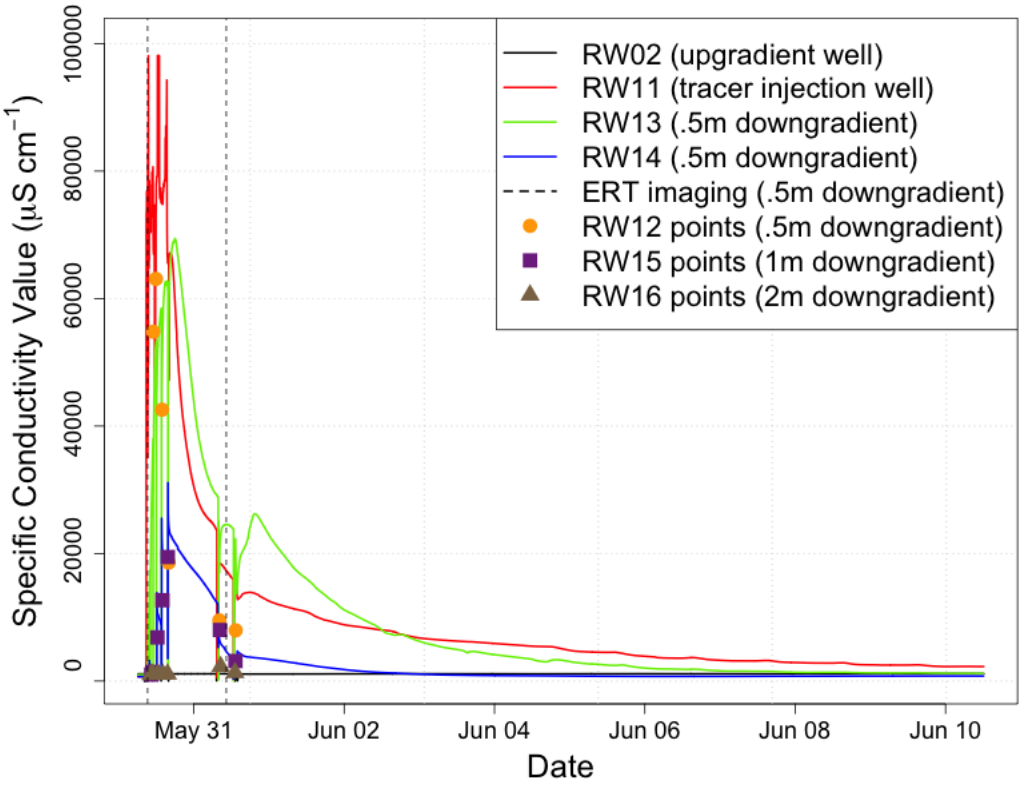


Figure 2.7: Specific conductivities observed at individual wells during the tracer experiment. Discontinuities in the recession of the breakthrough curve are the result of removing probes during the experiment to download data. Symbols indicate point measurements collected using a single conductivity probe in wells lacking continuous logging. Data were collected at 60-second intervals for 27.75 hrs, and subsequently at 15-minute intervals until the end of the injection period (11.3 days). Vertical dashed grey lines indicate the beginning and the end of the period over which 13-time lapse ERT images of the tracer plume were collected.

The tracer plume was first evident in substrate resistivity values at the transect 0.5-m downstream from the injection well within the first hr of the injection (Figure 2.8B), and tracer remained strongly evident in the system 24 hrs after the initiation of the 6.5-hr injection (Figure 2.8F). Resistivity values began to decrease from the peak values at some time between 11 hrs

and 24 hrs after initiation of the injection (Figure 2.8E,F). Comparison of the location of the plume (Figures 2.8B-F) to the ERT image that is not influenced by the plume (Figure 2.8A) indicates that transport of the tracer was primarily in more electrically resistive aquifer material, identified as K-means cluster four, which dictates the majority of the imaged aquifer.

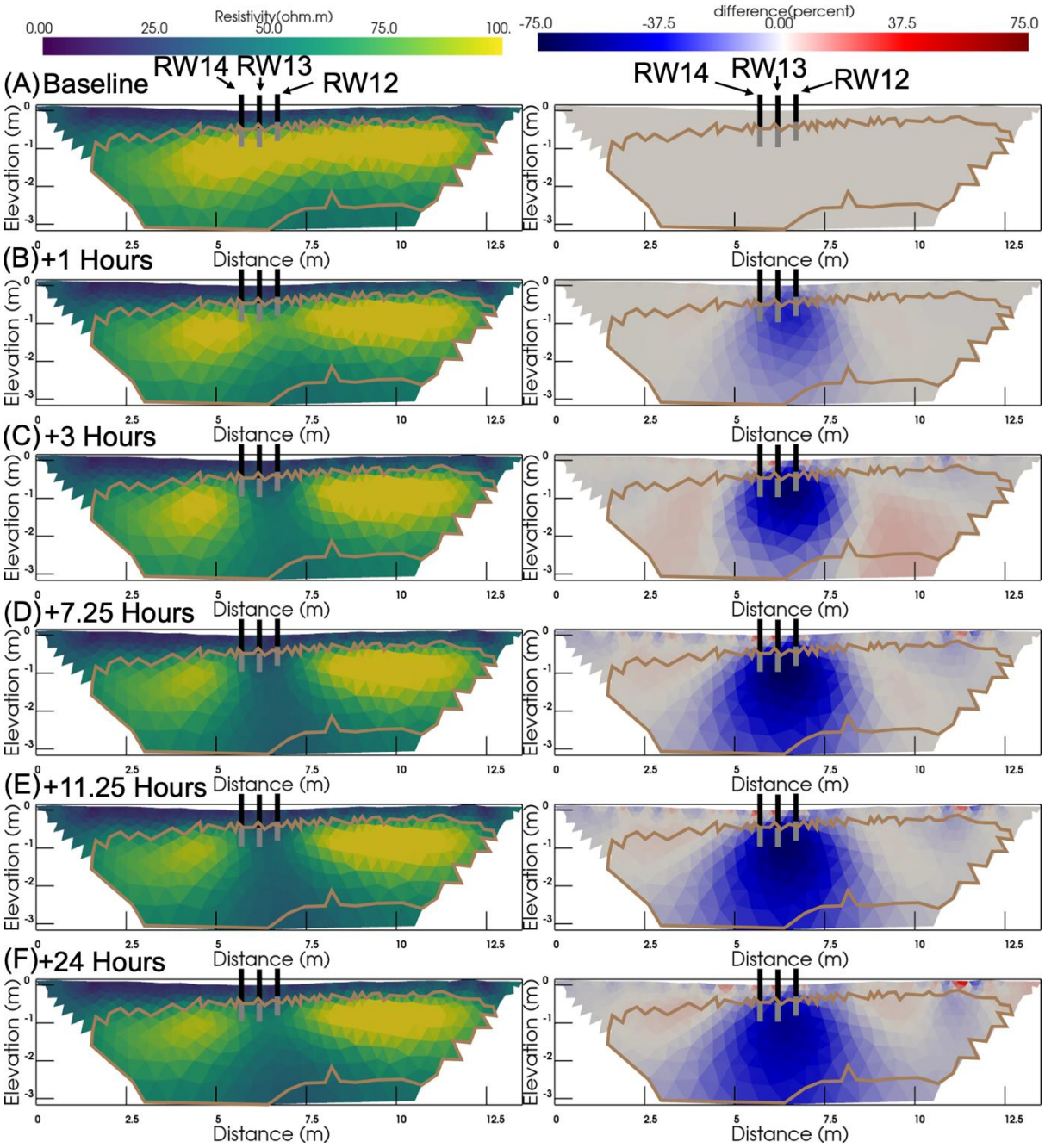


Figure 2.8: ERT images at the RW14 transect over 24 hrs following initiation of the tracer injection. The ERT transect intersecting wells RW12-14 is located 0.5 m downgradient from the injection well (RW11). The left column displays the cross-sectional distribution of electrical resistivity and the right column depicts the percent change in resistivity from the cross-sectional distribution not influenced by the tracer test (panel A). The brown polygon outline represents the extent of the fourth K-means cluster, based on the baseline image using thresholds documented

in Table 2.1. Well casings are indicated by black bars and well screens are indicated by grey bars. The time at the top left of each panel is the time after the initiation of the 6.5-hr injection.

2.3.4 Simulating the Tracer Response

Model simulations and sensitivity analysis provide perspective on the primary mechanisms by which potential bimodal variation in substrate texture influences solute transport. Results from adding hypothetical reactive solute processing to the fine textured component of the model provides further perspective on the implications of solute residence time to overall reactive transport in riparian aquifer flow paths.

2.3.4.1 Model sensitivity analysis and best-fit response When assessing the 5,000 realizations that were most likely to be within the range of uncertainty in the observed breakthrough curve (Figure 2.9C), simulations deemed inadequate to match our uncertainty window (n = 2,500) had a lower log-likelihood value. This was due to either the parametrized K_C and f_C value being too high or too low (Figure 2.9A), which resulted in NaCl concentrations value that were consistently too large or too small considered adequate to match the uncertainty window associated with our observations (Figure 2.9C).

Varying K_C values in the dual textured model had a strong influence on the character of the recession of the simulated breakthrough curve, indicating changes in the residence time distribution. As a result, only K_C values of 7.0-8.8 m d^{-1} fall within the 2.5th percentile of closest fit simulations to the normalized breakthrough curve (n=63) (Figure 2.9A). In comparison, these same simulations were generated by K_F values that spanned nearly the entire range of parameterized K_F values, from 0.090 to 0.895 m d^{-1} (Figure 2.9B). These simulations were also generated by f_C values that ranged from 0.16 to 0.89 (Figure 2.9A), which appeared to be at least

partly a result of covariation with K_F in determining the relative shape of the residence time distribution (Figure 2.9B).

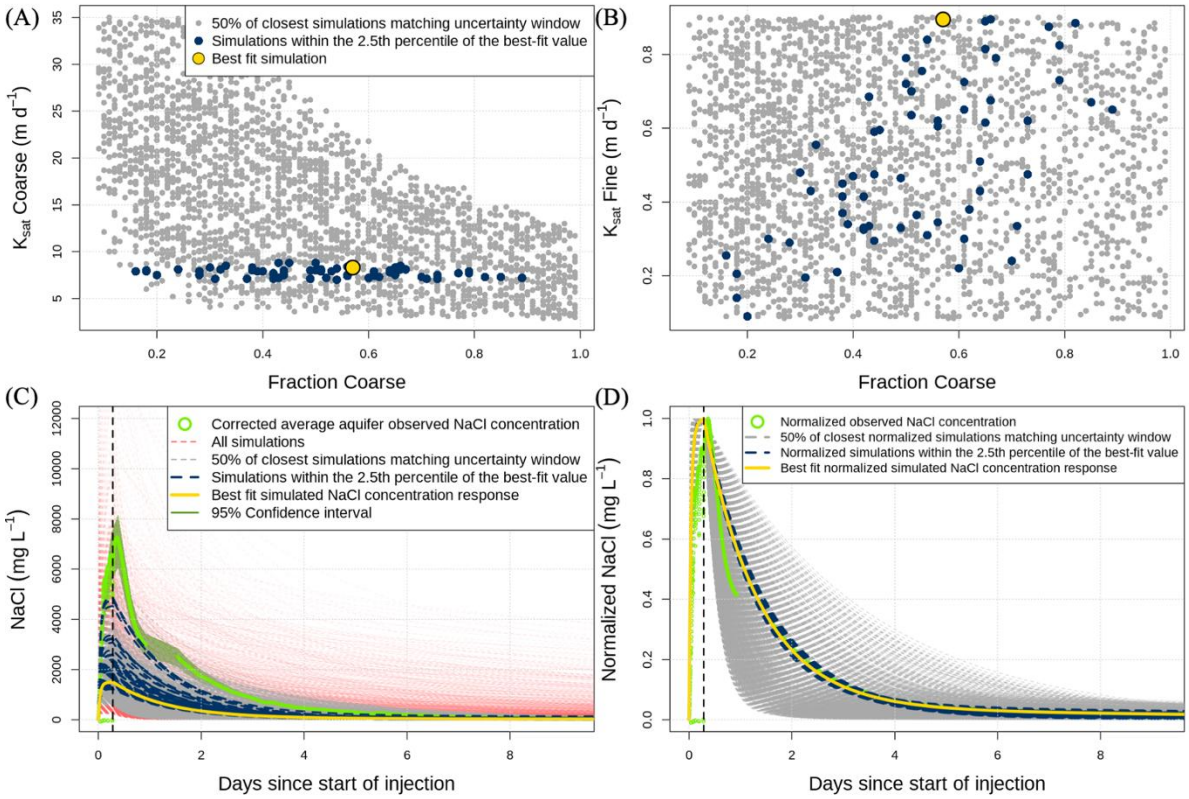


Figure 2.9: (A-B) Parameter values for the 2,500 of the 5,000 realizations that were most likely to be within the range of uncertainty in the observed breakthrough curve (grey points). Dark blue points are simulations in the 2.5th percentile of the best-fits to the normalized breakthrough curve, and the gold point is the best fit to the normalized breakthrough curve. (A) K_C vs. f_C and (B) K_F vs f_C. (C) Simulated concentration responses. The green points reflect our estimate of the breakthrough curve for the average concentration across the plume. The red lines indicate all 5,000 simulations, grey lines represent the 2,500 simulations that are most likely to be within the uncertainty window, dark blue lines indicate simulations within the 2.5th percentile of the best-fit to the normalized breakthrough curve, and the gold line is the best-fit to the to the normalized breakthrough curve (K_C = 8.3m d^{-1}, K_F = 0.895m d^{-1}, f_C = 57%). The vertical dashed black line indicates when the hydraulic head at the injection well returned to ambient conditions. (D) Normalized simulation results that fit our uncertainty window, with repeated color patterns.

A K_C value of 8.3m d^{-1}, a K_F value of 0.895m d^{-1}, and a f_C value of 0.57 produced the simulated normalized break through curve that was the best-fit to the observed normalized

breakthrough curve (Figure 2.9D). The peak NaCl concentration for this best fit to the normalized breakthrough curve was 1,507 mg L^{-1}, which was much lower than the estimated plume-averaged observed peak NaCl concentration of 7,264 mg L^{-1} (Figure 2.9C). Comparatively, the mean of the peak concentrations for the 2.5th percentile of simulations that were most similar to the normalized breakthrough curve is 2,065 mg L^{-1}, suggesting that simulations with relative residence time distributions most similar to that observed were overestimating volumetric flow rates (Figure 2.9C). We suspect that NaCl concentrations, within the 2.5th percentile of best fit values, are lower than our corrected observed concentrations due to small scale heterogeneity in salt distribution that is not resolved by the ERT imaging (Figure 2.9C), potentially reducing the accuracy of the conversion from resistivity values to aquifer wide average NaCl concentrations (Figure 2.S7-2.S9). Additionally, this may be caused by model assuming fully mixed reservoirs, which are not true representations of a system that is not fully mixed.

2.3.4.2 Nitrate Attenuation The observed nitrate concentration and associated analytical uncertainty in the injection well RW11 was 2.74 ± 0.14 NO_3-N mg L^{-1} (n=1), while the downgradient observation wells RW12-RW13 had an average concentration and analytical uncertainty of 2.59 ± 0.13 NO_3-N mg L^{-1} (n=2) (Table 2.1), suggesting a percent of nitrate remaining after passing through the system ($f_{N,out} \cdot 100\%$) of 94.5 ± 7%, when propagating analytical uncertainties. Using the hydraulic parameters estimated from the best-fit normalized breakthrough curve and a first order rate constant for fine textured sediment (k_F) derived from literature, the simulated percent of nitrate remaining was 93.1% (Figure 2.10). For the best fit hydraulic model, changing the nitrate consumption rate constant (k_F) by an order of magnitude

up or down resulted in changes to $f_{N,out}$ value of only 1.79%, indicating limited sensitivity of $f_{N,out}$ to changes in k_F (Figure 2.10).

All but one of the 2.5th percentile of simulations that most closely match the normalized tracer observations produced $f_{N,out}$ values within the uncertainty range of the observed $f_{N,out}$ value of 87.5% to 100%. For these simulations, f_C values varied strongly, ranging from 0.18 to 0.89 (Figure 2.10). Across these simulations, the average fraction of nitrate remaining within the fines compartment ($f_{N,F,ss}$) was 4.51%, and varied from 0.47% to 30.95% as the k_F was adjusted an order of magnitude higher and an order of magnitude lower.

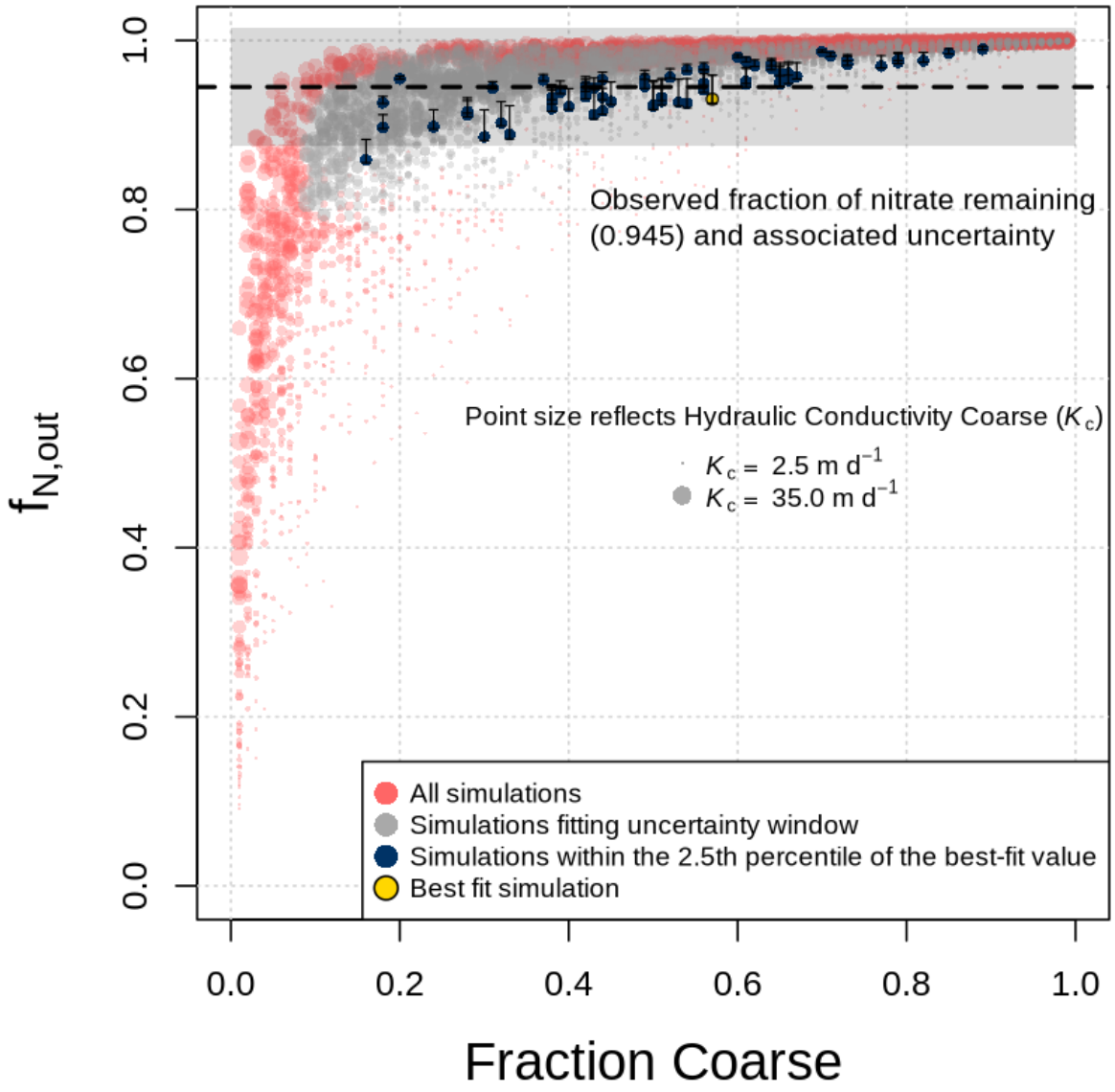


Figure 2.10: Simulated mass fraction of nitrate (NO_3-N mg L^{-1}) remaining in the aquifer ($f_{N,out}$) corresponding to flow simulations and the assumption of solute reaction occurring in the fine texture component. Results are based on a first-order nitrate reaction rate constant in the fine textured sediment (k_F = 1.39×10−5 s^{-1}) (Marzadri et al., 2012; Ocampo et al., 2006; Reinhold et al., 2025). The dashed black line denotes the observed $f_{N,out}$ value between RW11 (one observation) and an average of two concentration values obtained for RW12-RW13 (Table 2.S2), with propagated analytical uncertainty indicated with a grey box. The size of the points corresponds with the simulated K_C value (2.5-35 by 0.1), with larger points reflecting higher K_C values. Our best fit simulation is marked in gold (no point scaling for visualization purposes), the 2.5th percentile of closest fit simulations to the normalized breakthrough curve in dark blue (no point scaling), 50% of simulations most likely matching our uncertainty window in grey, and the

remaining simulations in red. Error bars associated with the plotted 2.5th percentile best fit simulations reflect the range of $f_{N,out}$ values obtained by varying k_F an order of magnitude above and below the literature-based estimate.

2.4. Discussion

Comparisons of characterizations of hydraulic conductivity, nitrate concentrations, and substrate architecture in riparian aquifers provides insight into the spatially complex variation in hydrological and biogeochemical conditions that determine the potential for agricultural stream corridors to mitigate excess nutrient loading. Evidence of stark contrast between hydrological and biogeochemical behavior of finer and coarser textures motivates efforts to understand the influence of this heterogeneity on solute fate and transport. Injection of an artificial tracer, monitored via continuous specific conductivity measurements and time-lapse ERT imagery of the riparian flow path transect, further hones understanding of the role of heterogeneity in substrate structure on solute transport. This bimodal substrate modeling exercise, informed by tracer test results and observations of nitrate concentration, capture key effects of variation in riparian substrate architecture on the reactive transport behavior of riparian aquifer flow paths.

2.4.1 Substrate Architecture Regulates Nitrate Concentrations

Lower bulk resistivity values derived from ERT imaging are associated with the lowest estimated hydraulic conductivities (<1 m d^{-1}) measured at the riparian wells (Table 2.1), while higher resistivity values do not show a coherent pattern with variation in higher hydraulic conductivity values (>1 m d^{-1}). Our observed riparian K_{sat} values (0.0400 m d^{-1} to 34.3 m d^{-1}) are similar to reported values for fine sand and silt material (0.03 m d^{-1}) to well-sorted sand in freshwater aquifer systems (30 m d^{-1}) (Bear, 1975). The lower-K_{sat} values (<1 m d^{-1}) at RW02,

RW03, and RW10 were associated with lower resistivity material (K-means clusters 1-2) in ERT imaging (Figure 2.6C,D, Table 2.1), indicating finer-textured sediments that likely impede flow. In contrast, variation in the hydraulic conductivity in the higher-K_{sat} values (>1 m d^{-1}) observed in riparian wells RW01, RW04 and RW08 were less predictable from the electrical resistivity (Figure 2.6A,B, Table 2.1). ERT imaging indicates that resistivity values adjacent to the well screens for RW01, RW04, and RW08 possess a wider range of resistivity values located along their well screen (K-means clusters 2-4), perhaps confounding the ability to observe a pattern between the resistivity and estimated hydraulic conductivity (Table 2.1). This complexity is captured in RW01 imaging (Figure 2.S1), which had the highest reported K_{sat} value (Table 2.1) but has screening completed across a range of intermediate resistivity values (Table 2.1), indicating mixed substrate. Although the estimated hydraulic conductivity values suggest that RW01, RW04, and RW08 are located within coarser, more permeable sediments that facilitate greater groundwater flow, this assessment is difficult to capture using the ERT data. The resolution of these geophysical measurements is limited in its ability to accurately capture pore space geometry important to these estimated hydraulic properties (L. Slater, 2007). Additionally, at higher resistivities, the relationship between resistivity and hydraulic conductivities can be muted by the errors associated with geophysical data acquisition and inversion techniques. Further fine-scale in-situ lithologic assessment is needed at this site to do determine how riparian substrate K_{sat} relates to local geophysical measurements.

Across sixteen riparian wells, nitrate concentrations in higher-K_{sat} wells (>1 m d^{-1}) were higher on average and much more variable than those in lower-K_{sat} wells (<1 m d^{-1}) (Figure 2.6, Table 2.1). Both ERT and hydraulic conductivity suggest that lower-K_{sat} wells primarily draw

water from finer-textured substrates (K-means clusters 1-2, 10.1-41.8 ohm; Table 2.2), where lower nitrate concentrations (0.00 to 2.57 NO_3-N mg L^{-1}) may be the result of greater reaction rates relative to transport rates associated with reducing conditions (Schaetzl & Thomson, 2015; Wald et al., 2013). Higher-K_{sat} wells are likely to sample water flowing through coarser substrates (K-means clusters 3-4, 41.8-130.2 ohm), where generally higher nitrate concentrations may indicate less probability of reaction in the flow path and more variable nitrate concentrations may indicate variable degrees of connectivity with adjacent finer-textured regions with reducing conditions. These findings support our hypothesis that the distribution of finer substrate is a primary control on nitrate consumption patterns present in this riparian aquifer. Higher-K_{sat} zones increase flow velocity and the amount of time with which nitrate reduction can influence water chemistry. Additionally, coarser substrates typically contain less organic carbon than finer substrates, limiting not just the contact time but the energy needed for nitrate attenuation via denitrification (Beauchamp et al., 1989; Haycock & Pinay, 1993; Hill et al., 2000; McClain et al., 2003; Schultz et al., 2004; Tomasek et al., 2017; Welsh et al., 2017). Taken together, differences in patterns in nitrate concentration between wells completed in fine and coarse substrates support the idea that the spatial distribution of the fine sediments may control the extent and location of nitrate reduction capacity, but water and solute exchange between these fine sediments and flow paths through coarse sediments may determine the overall behavior of the riparian aquifer.

2.4.2 Groundwater Movement Encompasses Variable Substrate, Suggesting Hydrologic Exchange of Biogeochemically Distinct Waters

Breakthrough curves from a conductive tracer plume simultaneously observed with time-lapse ERT imagery suggest that riparian groundwater experiences storage in variable substrate

textures along its flow path. The average residence time in the 0.52 m longitudinal extent of the riparian aquifer subject to the tracer test was 1.8 days, though the initial arrival of tracer at the observation well was observed within 14 minutes of injection. This notable level of apparent advective dispersion over such a short flow path is most likely explained by the combined influence of preferential flow through zones of coarse sediments interacting with longer term storage in zones of finer sediments.

Exploration of the tracer data using a simple dual storage model suggests that hydrological connection between contrasting substrates influences residence time distributions observed in unconfined riparian aquifers. Our simple simulation results provide evidence supporting our hypothesis that coarse substrate dictates the total amount of flow, due to limited variability in coarse substrate hydraulic conductivity (K_C) *v*alues that represent simulation results within the 2.5th percentile of the best-fit to the normalized breakthrough curve (Figure 2.9A). In contrast, a wide variation in the lower hydraulic conductivity values for the fine-textured component had little influence on the magnitude of flow and little apparent independent influence on relative residence times (Figure 2.9B,D). The fraction of coarse material (f_C) also varies across nearly the entire range of predetermined values when assessing these simulations, suggesting a wide range of coarse and fine material proportions can describe the observed behavior if other factors like the hydraulic conductivity of fine sediments are allowed to vary (Figure 2.9A,B).

Monitoring of the tracer plume via ERT imaging demonstrates the spatial extent of the plume within the riparian aquifer. Prior to tracer fluid injection, inverted resistivity values in the baseline image (Figure 2.8A) reveal a relatively uniform lens of high-resistivity material that we

interpret as generally coarser textured material (K-means cluster four) at roughly 0.5-meter depth, with surrounding areas of the imaged subsurface containing low-resistivity values that are likely associated with finer textured materials or shale bedrock. The tracer plume appears to initially move within this more resistive material and the less resistive material near the surface (Figure 2.8B,C) but ultimately moves laterally and deeper into surrounding substrate over the observational period (Figure 2.8D,F). This apparent movement into the deeper, more electrically conductive substrate, may be partially due to the increased density of the tracer fluid, observed in other studies (Muller et al., 2010), and the artificially raised hydraulic head during our tracer injection period. Although dispersion of the tracer and modeling results support complexity promoting preferential flow and long-term storage in the riparian substrate composition, the ERT imaging appears to depict a relatively uniformly expanding plume that might be expected in relatively homogenous substrate. The spatial resolution limitations of the ERT may prevent visualization of the variation in hydraulic conductivity at the spatial scale that actually determines the observed behavior (Day-Lewis et al., 2005; Ward et al., 2010b).

2.4.3 Flow Dynamics Dictate Nitrate Attenuation Patterns

Simulations that assume nitrate reduction occurs solely within the fine-textured compartment capture the general nitrate attenuation patterns observed along the monitored flow path. Assuming a first order nitrate consumption rate constant (k_F), the calculated $f_{N,out}$ value for most of the 2.5th percentile of simulations that most closely match the normalized tracer observations fell within the uncertainty range of the observed $f_{N,out}$ value (87.5% to 100%). This indicates that these simulations, using a first order nitrate consumption rate constant, are adequately capturing nitrate attenuation processes observed in this aquifer. Simulations that

resulted in $f_{N,out}$ values less than the observed nitrate attenuation value ($f_{N,out}$) range, indicating increased nitrate removal, coincided with reduced proportion of coarse material (f_C) (Figure 2.10). More coarse material indicates greater proportion of flow through the mobile non-reactive coarse compartment (Q_C), which limits possibility of reactivity within our less mobile fine compartment as the proportion of flow in this compartment (Q_F) is reduced. However, limitations of these findings are that the observed nitrate attenuation values are relatively uncertain due to limited observations at the upgradient well (one) and downgradient wells (two) providing limited constraint on our observed aquifer $f_{N,out}$ value. Additional measurements of groundwater nitrate concentrations along this flow path are needed to further constrain the observed aquifer $f_{N,out}$ value. Further, the observed $f_{N,out}$ value (94.5%) reflects a net change in nitrate, which does not account for gross changes due to production and consumption (Mayernik, et al., in revision).

The importance of flow through the fine textured material in dictating nitrate attenuation patterns within the aquifer is also captured when assessing variable k_F values. Applying k_F values at an order of magnitude higher and lower than the first order nitrate consumption rate constant resulted in an average $f_{N,out}$ range of 1.80% amongst the 2.5th percentile of best-fit normalized curves. This minimal range suggests that flow through the reactive compartment is more important for simulated nitrate attenuation processes than the reactive compartment's applied nitrate consumption value (k_F). Assessing nitrate consumption within the fines compartment ($f_{N,F,ss}$) at different k_F values resulted in a larger range of possibilities (average range of 30.5% from the 2.5th percentile of best-fit normalized curves). This suggests that within the fine compartment varying k_F does influence the nitrate attenuation patterns, but these patterns are muted at an aquifer scale, due to a larger proportion of flow occurring within the coarse substrate

compartment, limiting any potential reaction within these simulations. It is important to note that these simulations may underestimate the proportion of flow undergoing nitrate reduction due to the lack of simulated exchange of waters between coarse and fine substrate compartments within the model domain (Donado et al., 2009; Haggerty & Gorelick, 1995), although the limited extent of the control volume in the present simulation (0.52 m of flow path length) may limit the bias from this simplification. Additionally, the simplification that no nitrate reduction occurs within the coarse substrate may be an oversimplification, as nitrate reduction has been documented at depth in substrate with reduced DOC in riparian areas (Clément et al., 2002), but we assumed these reactions were negligible relative to residence times through this material.

Overall, our simulation results generally captured observed nitrate attenuation patterns and provide evidence to suggest that magnitude of flow through fine material is more important to nitrate attenuation processes within these stream corridors than the nitrate consumption rate constant of the reactive substrate. These results highlight the importance of augmented natural wetland ecosystems within agricultural landscapes, where human modification of the natural system has altered substrate architecture with e.g., pond construction, but has retained the essential wetland character. Augmented wetlands reduce flow rates of impaired groundwater, contribute organic carbon sources (Fisher & Acreman, 2004), and are known to be more efficient at removing nitrate as compared to constructed wetland systems (Batson et al., 2012; Tournebize et al., 2017). Considering agricultural nitrate pollutants are diffuse non-point source pollutants, maintaining productive natural wetlands amongst these agricultural landscapes will contribute to nitrate reduction at the landscape scale.

2.5. Conclusions

Our results provide a reach-scale perspective of the relationship between riparian groundwater nitrate concentration, flow dynamics, and substrate composition in stream corridors loaded with elevated nitrate from agricultural activities. This research provides a novel perspective of flow dynamics and nitrate attenuation patterns by combining geochemical data, geophysical observations, tracer observations, and hydrological simulations. We found that flow dynamics are intimately connected with nitrate concentrations, with riparian wells completed in coarser substrate having higher nitrate concentrations compared to wells completed in finer substrate. Simulations of the tracer results that account for nitrate attenuation generally captured observed nitrate attenuation processes and illustrate how coarse textures regulate the total amount of flow while the degree of exchange between coarse and fine textured material may regulate nitrate consumption. Human manipulation of substrate in these corridors affects the relative effects of reaction and transport, highlighting potential for managed nitrate reduction within agriculturally intensive stream corridors.

Acknowledgements

The authors thank the USDA-ARS Agreement 58-3032- 005, the Consortium for Research on Environmental Water Systems (NSF EPSCoR Cooperative Agreement OIA-1757351), the NSF Signals in the Soil Award 2034430, the Montana State University Nielson Pedology Graduate Research Fellowship (2024), the Montana Agricultural Experiment Station (Project numbers MONB00364 and MONB00349), and the Montana State University Environmental Analytical Lab. Any opinions, findings, conclusions or recommendations expressed in this material are

those of the authors and do not necessarily reflect the views of the National Science Foundation or the U.S. Department of Agriculture. We thank Caitlin Mayernik for initial data collection and laying the foundation for the work presented here. Additionally, we thank Dr. Toby Koffman, Skye Keeshin, Carl Krause, Kieran Tharp, Wyatt Kray, and Emma Tate for their help with data collection, analysis, and technical assistance.

CHAPTER THREE

STUBBLE MANAGEMENT AND ASSOCIATED SOIL MOISTURE DELIVERY IN CULTIVATED SOILS OF DRYLAND CEREAL PRODUCTION SYSTEMS IN CENTRAL AND SOUTHWEST MONTANA, USA

Contribution of Authors and Co-Authors

Manuscript in Chapter 3

Author: Jack W. Poole

Contributions: Collected field data, developed ideas and methodologies, and compiled manuscript.

Co-Author: Stephanie A. Ewing

Contributions: Developed research questions and goals, lead investigator on project, contributed to methodology creation, guidance on data analysis and extensive feedback on the manuscript.

Co-Author: Perry R. Miller

Contributions: Provided agronomic perspective on research and contributed to extensive manuscript feedback.

Co-Author: Simon I. Fordyce

Contributions: Provided agronomic perspective on research, helped with data collection, and provided manuscript feedback.

Co-Author: Robert A. Payn

Contributions: Provided extensive feedback on manuscript.

Co-Author: Eric A. Sproles

Contributions: Provided feedback on LiDAR imaging analysis procedures.

Manuscript Information

Jack W. Poole, Stephanie A. Ewing, Perry R. Miller, Simon I. Fordyce, Robert A. Payn, Eric A. Sproles

Status of Manuscript:
☒ Prepared for submission to a peer-reviewed journal
☐ Officially submitted to a peer-reviewed journal
☐ Accepted by a peer-reviewed journal
☐ Published in a peer-reviewed journal

Abstract

Dryland cereal production in the Northern Great Plains requires efficient water use. Historically, the management practice of summer fallow, in which arable land is left idle and weeds are controlled chemically, has been used as a means of mitigating drought induced crop failure. However, summer fallow can also create economic inefficiencies, increase soil erosion, and facilitate nutrient loss to groundwater. Alternative management practices that promote more effective soil water retention offer a potential solution by promoting beneficial conditions, supporting continuous cropping. Maximizing dryland cereal crop stubble using alternative harvest methods (e.g., "stripper header" technology) is known to improve snow capture and reduce evaporative losses, but impacts of these practices on the isotopic composition of soil water remain unclear. At two sites in central and southwest Montana, we combined meteorological monitoring, snowpack analysis, and multiple measures of soil water content and isotopic composition to assess these relationships. In southwest Montana during the winter of 2022-2023, we observed significantly more snowpack and snow water equivalent (SWE) with increased stubble height until late spring, when a large storm eliminated differences. At the central Montana site, we used soil water isotopic composition ($\delta^{18}O$, $\delta^{2}H$ values**)** to quantify snow contributions and evaporative loss. At this site, during the low-snow winter of 2023-2024, we observed mixed results of snow accumulation, with more accumulation in taller stubble in January during a small snowfall event, but equal snow accumulation in February, following a separate event. The greater snow accumulation in taller stubble during the January snowfall event led to soil water $\delta^{18}O$ and $\delta^{2}H$ values (0-10 cm) more closely resembling the isotopic composition of the snow in tall versus short stubble, reflecting an addition of 2.3 cm of snow-

derived water into the tall stubble soil profile. During summer sampling events, increased evaporation altered soil water $\delta^{18}O$ and $\delta^{2}H$ values, with a stronger evaporative signature at 10 cm depth and 1.2 cm greater water loss across the sampled soil profile (0-30 cm) in short stubble compared to tall stubble following a short period of reduced precipitation and warmer temperatures. Overall, our results demonstrate variability in snow accumulation in tall stubble as a function of residue management and snow delivery and show how soil water isotopic composition reflects gains and losses of soil water – caused by stubble height management - in dryland agricultural settings of central Montana.

3.1 Introduction

Globally, non-irrigated agriculture accounts for nearly 60% of total food production (Rosegrant et al., 2002; Siebert et al., 2005; Stewart et al., 2015). In the semi-arid Northern Great Plains of the United States (NGP) (Figure 1A), dryland cereal production is common, accounting for 34% of U.S. wheat (*Triticum aestivum* L.) and 51% of U.S. barley (*Hordeum vulgare* L.) (Hansen et al., 2017; Lawrence et al., 2018; Stewart & Koohafkan, 2015; USDA, n.d.). Changing weather patterns in this region are predicted to include shorter winters with warmer springs (H. W. Cutforth et al., 1999; Lanning et al., 2010; Whitlock et al., 2017). These changes make the interaction of the amount and timing of precipitation events with soil water storage in dryland agricultural systems critical for producers to achieve sustainable crop yields.

The predominantly dryland small-grain agriculture in this region relies on water use efficiency (WUE) for maximum productivity (Nielsen et al., 2005). In these systems, management practices that may influence soil water storage include no-till, summer fallow, and stubble height management (H. W. Cutforth & McConkey, 1997; Lyon et al., 1998; Nielsen et al.,

2005; Ries & Power, 1981; Schillinger & Wuest, 2021; Tanaka et al., 2010). In the NGP of Montana, the use of no-till has been widespread since the 1990s (Engel et al., 2017; Sigler et al. 2018) and summer fallowing has traditionally been ubiquitous, peaking in 1971, and included in typical dryland cropping rotations every two to four years (Engel et al., 2017; Lenssen et al., 2007; Lyon & Peterson, 2005; Tanaka et al., 2010). This practice is intended to store soil water for subsequent crops, potentially reducing the risk of crop failure from drought (Peterson & Westfall, 2004; Stöckle et al., 2018; Tanaka et al., 2010). However, it can also increase soil erosion (Larney et al., 1995; Liebig et al., 2004; Schillinger et al., 2015), diminish soil organic matter (SOM) (Cochran et al., 2015; Hatfield & Sauer, 2015; Liebig et al., 2004; Rasmussen & Parton, 1994; Williams, 2004), produce economic inefficiencies (Aase & Schaefer, 1996; Chen et al., 2015; Halvorson et al., 1994; Miller et al. 2015), and enhance leaching of soil nitrate derived from both nitrogen fertilizer and mineralization of soil organic matter (Custer, 1976; John et al., 2017; Sigler et al., 2020), degrading water quality in both underlying aquifers and connected riparian areas (Custer, 1976; John et al., 2017; Mayernik et al., 2024; Sigler et al., 2018).

Stubble height management in cereal crops manipulates the infield standing crop residue (stubble) during harvest. Very tall stubble (>45 cm) can be achieved at a producer field scale using a stripper header on a harvester that removes only the grain from the plant stem, leaving the plant stubble intact and at full height (Schlegel et al., 2023). This harvesting technique reduces harvest costs due to decreased machine in-field times (Klinner et al., 1987; L.A. Haag et al., 2004) and improved fuel efficiencies (Chegini & Mirnezami, 2016; İnce et al., 2011). Stubble height management has been studied for decades, showing that tall stubble can increase subsequent crop yields and improve WUE (Campbell et al., 1992; H. Cutforth et al., 2011; H. W.

Cutforth & McConkey, 1997), potentially providing favorable conditions for continuous cropping, reducing summer fallow rotations. In particular, increased stubble height can enhance snow retention during winter precipitation events (Aase & Siddoway, 1980; Black & Siddoway, 1977; Campbell et al., 1992; Hoefer et al., 1981; Schillinger & Wuest, 2021), increase shading of the soil surface that cools the soil and reduces near surface evaporation (H. W. Cutforth & McConkey, 1997), and decrease near surface wind velocities that increase favorable growing conditions and reduce soil erosion (Ann McCauley & Clain Jones, 2005; H. W. Cutforth & McConkey, 1997; McMaster et al., 2000). However, the snow capture and microclimate benefits of very tall stubble management are still not fully known, with inconsistencies of results among experiments, due to local management decisions and variable weather patterns (Aase & Siddoway, 1980; Campbell et al., 1992; Flerchinger et al., 2003).

Stable isotope ratios of hydrogen and oxygen (δ^2H and $\delta^{18}O$) in the water molecule offer a way to track seasonal water sources and transformation in soils. These δ^2H and $\delta^{18}O$ values originate with source precipitation in meteoric waters as a function of atmospheric temperature and can later be modified through evaporation and mixing (Sharp, 2017). In rain or snow, more negative values of δ^2H and $\delta^{18}O$ reflect colder temperatures, and less negative values reflect warmer temperatures (Clark & Fritz, 2013; Criss, 1999; Dansgaard, 1964). Evaporation effects favor loss of the lighter isotopes and are expressed first in shallow soils (<30 cm) that are exposed to solar radiation (Barnes & Allison, 1988; Martin et al., 2018; Mayernik et al. 2024; Oerter & Bowen, 2019; Sprenger et al., 2016, 2017), while hydrologic mixing occurs with both evaporated waters and isotopically variable precipitation (Martin et al., 2018; Mayernik et al., 2024; McDonnell et al., 1991; Tetzlaff et al., 2014). The temporal variability of soil water δ^2H

and $\delta^{18}O$ values can reveal effects of precipitation sources and microclimate differences with variation in stubble heights.

This research investigated how stubble height management influences precipitation delivery and retention in two dryland agricultural systems of central (Moccasin) and southwest Montana (Bozeman). We used soil water isotopic composition through the winter-spring transition at the central Montana site to signal effects of stubble height including both snow capture and microclimate conditions favorable for soil water retention. We sought to better understand the fundamental interactions of stubble height management with the resulting spatiotemporal patterns of soil water storage at a field scale. Given previous observations that taller stubble increases snow capture and results in beneficial microclimate conditions during the growing season, we predicted that soil water isotopes collected in taller stubble would reflect more snow derived soil water and less evaporation as compared to short stubble. To better understand these specific dynamics our objectives were to:

1. Determine how the timing and form of precipitation over the winter season interacts with stubble height, at a field scale, to dictate the ongoing spatial distribution of snow capture.
2. Determine how precipitation delivery and microclimate effects, caused by contrasting stubble heights, influence soil water isotopic composition and water content.

To address these objectives, we: (1) assessed the spatiotemporal variability of snowpack distribution at Bozeman and Moccasin MT, (2) quantified soil water content at Bozeman and Moccasin MT, and (3) evaluated soil water sources and character using soil water isotopic composition at Moccasin MT. Our results reveal how seasonal trends of soil water isotopes track the interaction of soil type with precipitation patterns and management strategies.

3.2 Data and Methods

3.2.1 Study areas

We studied the influence of wheat stubble height in test plots at two study sites, one in southwestern Montana at the Montana State University Arthur H. Post (Post) research farm (2022-2023), located near Bozeman, and the other at a cooperating producer's field in central Montana, near Moccasin (2023-2024) (Figure 3.1). The Moccasin study site is located within the Northern Great Plains (NGP) ecoregion (Figure 3.1A) (Padbury et al., 2002), while the Bozeman site is just outside of this region within the Middle Rockies ecoregion. These sites host a continental climate, with long, cold winters and short, warm summers, large differences between day and night temperatures, and frequent strong winds, more prevalent at the central Montana location (up to 15.7 m s^{-1} at Moccasin based on Mesonet data). Precipitation patterns are highly sporadic, particularly during the summertime with infrequent precipitation events, making dryland crop production difficult to predict and manage (Carr et al., 2020; P. R. Miller et al., 2002).

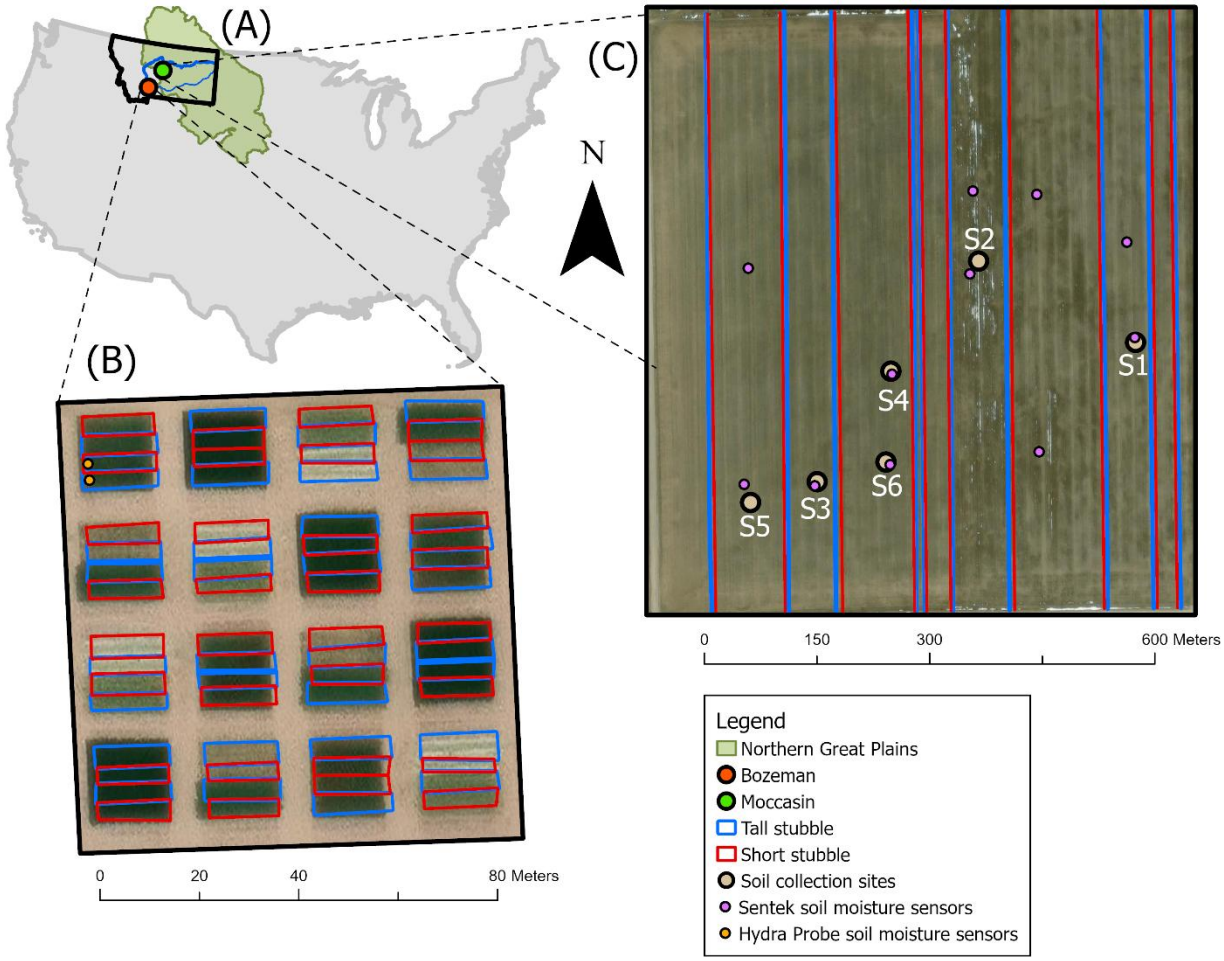


Figure 3.1: Study sites. (A) The location of the two study site locations, Bozeman (red) and Moccasin (green) which is within the Northern Great Plains ecoregion and the state of Montana. (B) Bozeman study site at the Arthur H. Post research farm, within ongoing crop rotation study plots (CARB). Red polygons indicate short stubble locations (<15 cm), and blue indicate tall stubble (>45 cm). Orange circles indicate locations of Hydra Probe soil moisture sensors. (C) Moccasin study site on private agricultural land showing stubble height distribution. Red polygons indicate short stubble (<20 cm), and blue polygons indicate tall stubble (>60 cm). Soil collection locations documented by labeled brown circles and Sentek moisture probe locations indicated by purple points.

Seasonal precipitation patterns vary slightly between Bozeman and Moccasin but change more dramatically across the NGP, with drier conditions in northern Montana (Figure 3.2A). At the Bozeman study site, data collected from 1991-2020 indicate mean annual precipitation of 40.9 cm, with 45.6% of annual precipitation falling in the months of April, May, and June

(Figure 3.2B) (PRISM Climate Group, 2023). Recorded mean annual temperature over this period of record was 6.8 °C. At the Moccasin study site, the mean annual precipitation total is 38.9 cm, with 45.6% of annual precipitation falling in the months of April, May, and June (Figure 3.2B) (PRISM Climate Group, 2023). Mean annual temperature at this location is 6.6°C. At the Bozeman study site, 16.8% of annual precipitation (6.7 cm) falls during winter months (December-March) while only 12.2% of annual precipitation (4.7 cm) falls during this same period at the Moccasin site. Moccasin gets slightly more of its annual rainfall during the summer (June-August) (15.7 cm) as compared to the Bozeman site (13.2 cm) (Figure 3.2B) (PRISM Climate Group, 2023).

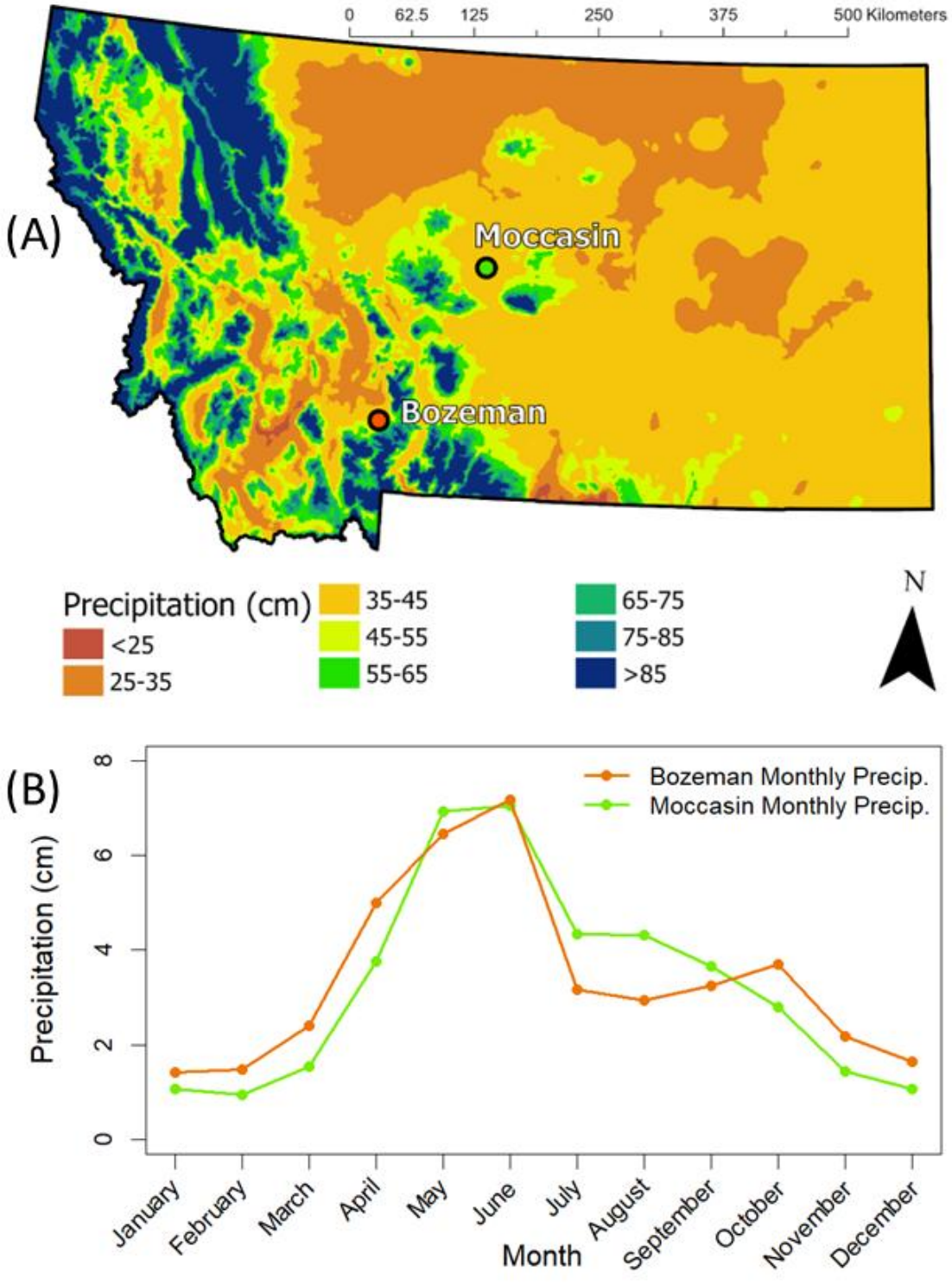


Figure 3.2: (A) Spatial patterns in 30-year (1991-2020) mean annual precipitation (cm) observed in Montana, including study sites at Bozeman and Moccasin, Montana. (B) Monthly

precipitation patterns at Bozeman and Moccasin, Montana. Data represents average over 30-year period (1991-2020), Data from the Oregon State PRISM network (PRISM Climate Group, 2023).

The Bozeman study site is located within an ongoing multi-year study, the carbon accrual rotation block (CARB), located at the Post farm. During the fall of 2021 winter wheat was planted across all study plots (3.66 m by 14.63 m, n = 64) and was harvested to generate randomized plots of very tall (>45 cm) and short (<15 cm) stubble during the fall of 2022. Soil moisture and snow data were collected from February until April of 2023, before the planting of the next season of crops in the spring. The study site consists of deep (>2 m) silt loam soils, classified as the Amsterdam soil series (Typic Haplustolls), formed from alluvially re-worked loess mantling alluvial fans (USDA NRCS, 2021).

The Moccasin study site was selected in collaboration with a local producer. The site is relatively flat, with an area of roughly 0.57 km^2, located at an elevation of 1,266 m. The collaborator planted winter wheat in fall 2022; harvested it with a stripper header (Shelbourne-Reynolds, Colby USA) in fall 2023 and subsequently cut the residue for straw with alternating very tall (>60 cm) and short (<15 cm) stubble strips, perpendicular to the prevailing westerly wind direction. After the winter of 2023-2024, field pea (*Pisum sativum*) was planted in May 2024 and harvested in July of 2024.The study site consists of shallow (0.4-1.0 m), dominantly fine-textured clay and clay loam soil horizons over horizons formed in alluvial gravels (Figure 3.S4, Table 3.S1). Soil series include the Judith series (Typic Calciustolls), with a transition to alluvial gravels at a shallow depth and limited clay accumulation; and the Danvers series (Typic Argiustolls), with higher clay accumulation percentages and a deeper transition to alluvial gravel

contact (USDA NRCS, 2021). We monitored snow and soil water from 23 January to 26 June, encompassing seeding and initial growth of the field pea crop (Table 3.1).

Table 3.1: Synthesis of sampling type by date for each location throughout our sampling campaigns of 2022-2023 (Bozeman) and 2023-2024 (Moccasin).

Sampling Date	**Location**	**Sample Type**
2/17/2023	Bozeman	Manual snow assessment, Snow-on drone flight
3/2/2023	Bozeman	Manual snow assessment, Snow-on drone flight
3/29/2023	Bozeman	Manual snow assessment
6/27/2023	Bozeman	Snow-free drone flight
1/23/2024	Moccasin	Manual snow assessment, Orthomosaic RGB image drone flight, Soil collection for water content and isotopic analysis
2/16/2024	Moccasin	Manual snow assessment, Soil collection for water content and isotopic analysis
3/26/2024	Moccasin	Soil collection for water content and isotopic analysis
4/5/2024	Moccasin	Soil collection for water content and isotopic analysis
4/14/2024	Moccasin	Soil collection for water content and isotopic analysis
5/15/2024	Moccasin	Soil collection for water content and isotopic analysis
6/11/2024	Moccasin	Soil collection for water content and isotopic analysis
6/26/2024	Moccasin	Soil collection for water content and isotopic analysis

3.2.2 Meteorological data, Bozeman and Moccasin MT

Data from neighboring Montana Mesonet sites (Montana Climate Office, 2025) reveal seasonal patterns in snow water equivalent and depth, precipitation, soil volumetric water content, soil temperature, and air temperature (Figures 3.2-3.3). For the Bozeman site, we present Mesonet data from the Montana State University Horticulture (Hort) farm on the MSU Bozeman campus, approximately six km from our study field at the Montana State University Post farm. Air temperature, precipitation, snow depth, soil volumetric water content, and soil temperature were measured at one-hr intervals at depths of 10, 20, and 50 cm (Montana Climate Office, 2025). Additionally, at the Hort Farm site, we sampled precipitation monthly for water isotope analysis using a Global Network of Isotopes in Precipitation (GNIP) sampler. When snow was present, snow depth and water equivalent were manually measured using an NRCS snow tube, with snow collected from the tube for water isotope analysis. Meteorological data presented from the Moccasin site is from the Montana State University Central Agricultural Research Center (CARC) Mesonet station, approximately four km from the Moccasin study site (Figure 3.1C). Snow water equivalent (SWE) was recorded every 15- min with a snow scale (Sommer SSG-2), while air temperature, precipitation, snow depth, soil volumetric water content, and soil temperature were measured at one-hr intervals at depths of 10, 20, and 50 cm (Montana Climate Office, 2025).

3.2.3 Snowpack observations, Bozeman and Moccasin MT

At Bozeman, snow depth and SWE were manually assessed on three dates: 17 February, 2 March, and 29 March 2023 (Table 3.1). At Moccasin, snowpack depth and SWE observations occurred on two dates, 23 January and 16 February 2024 (Table 3.1). Snow depth and SWE were

measured using a federal snow sampler, with snow collected from the tube for water isotope analysis (NRCS, n.d.). Snow depth was measured with a ruler when snow was too shallow for accurate SWE assessment.

We characterized snowpack spatial distribution by conducting unmanned aerial vehicle (UAV) (DJI Matrice 210 V2, Shenzhen China) flights with a mounted LiAir V70 (GreenValley International, Berkeley USA) LiDAR unit and a Sony A5100 RGB camera (Sony, Tokyo Japan) to capture snow depth information. Flights were conducted at an altitude of 100 m, with a flight speed of 5 m s^{-1}, a ground sample resolution of 3.33 cm $pixel^{-1}$, with a LiDAR unit equipped with a 905-nm wavelength laser. At Bozeman, LiDAR flights occurred within one day of manual field measurements on 17 February and 2 March 2023, with flight days selected accounting for recent storm events and local weather conditions suitable for successful UAV flights. The snow-free LiDAR model was collected on 27 June 2023 (Table 3.1). These datasets allowed for LiDAR derived snow depth calculations for each sampling date by subtracting the snow-free model from the snow-on model. An average LiDAR-derived snow depth bias was calculated for the flights on 17 February (4.6 cm) and 2 March 2023 (8.8 cm) by comparing the geolocated manual snow depth observations with the LiDAR derived observations. These values were then added to the LiDAR dataset to correct for error in LiDAR derived snow depth analysis, potentially caused by exposed agricultural stubble in the snow-free model (Harder et al., 2020) (Figure 3.S1, 3.S2). These datasets were further filtered, removing any visual outlier data values, and designating negative snow depth values as 0 cm (Figure 3.S3).

LiDAR-derived SWE measurements were calculated by multiplying LiDAR derived snow depth values with the average snow density calculated from manually collected SWE

measurements (Palomaki & Sproles, 2023). To assess point-based measured snow density (ρ_{SP}) from observed SWE (cm) and snow depth (cm) we use the following formula:

$$\rho_{SP} = \frac{SWE_O}{SD_O} \quad (1)$$

where both snow depth (SD_O) and SWE (SWE_O) measurements are recorded from on ground field observed measurements at individual points. We then calculate an average snow density (ρ_{SA}) based on all measured values, assuming a liquid water density of 1.000 g mL^{-1}. The average measured snow density on 17 February was 0.255 g cm^{-1} and 0.292 g cm^{-1} on 2 March. This average density value was then applied to all LiDAR derived snow depth values (SD_{UAV}), on each individual date, to obtain LiDAR - derived SWE measurements (SWE_{UAV}) using the following formula:

$$SWE_{UAV} = \rho_{SA} \cdot SD_{UAV} \quad (2)$$

At Moccasin, two flights were conducted on the same day as field measurements; however, due to limited snowpack depth on both sampling days (Table 3.1), the uncertainty in the LiDAR measurements was comparable to the observed snow depths, rendering the data unreliable for use. The orthomosaic RGB imaging from the drone flight on 23 January 2024 was used to capture presence / absence of snow, based on pixel reflectance, using a random forest classifier, trained using known locations of snow. This algorithm uses specific spectral values of individual pixels within the image and then builds multiple decision trees using this training data to classify other pixels within the image.

3.2.4 Soil sample collection and handling, Moccasin MT

Soil samples were collected eight times, from January to July of 2024 (Table 3.1). Soil samples were collected at depth intervals of 0-10 cm, 10-20 cm, and 20-30 cm using a soil sampling bucket and a handheld drill and auger head (Oakfield Apparatus, Oakfield USA). Three samples were collected at six locations co-located with Sentek soil moisture sensors (Sentek technologies, Stepney Australia) amongst tall stubble (S1, S2, S3) and short stubble (S4, S5, S6) (Figure 1C). Sampling locations were randomized within the field and samples were collected within two meters of previous sampling events.

Subsamples were collected in duplicate for soil water isotope analysis at each depth interval, from the same sampling hole, using 12 mL glass vials with poly-seal cone-lined caps, filled to maximum capacity. Vials were capped tightly, wrapped with parafilm, and stored in a cooler during transportation from the field site to the Montana State University's Environmental Analytical Lab (MSU EAL), where they were frozen for soil water extractions.

After filling vials, additional soil samples from adjacent holes, with the same depth intervals, were collected in the bucket samplers and transferred to gallon Ziploc bags for assessment of water content. At least 20 g of soil were collected at each depth and transported on ice in a cooler to the MSU EAL, where they were stored frozen until soil water content was assessed.

3.2.5 Soil water content, Bozeman and Moccasin MT

Bulk soils collected at the Moccasin study site were dried for 72 hr at 50 °C, then reweighed. Gravimetric water content (θ_g) was assessed using the following equation:

$$\theta_g = \frac{S_W - S_d}{(S_d - B)} \quad 3$$

where S_W represents the mass of the wet soil and collection bag (g), S_d represents the mass of the dry soil and collection bag (g), and B is the mass of the collection bag (g). Volumetric water content (θ_v) was then derived using a soil bulk density value (g cm^3):

$$\theta_v = \frac{\theta_g \cdot \rho_w}{\rho_b} \quad 4$$

Where ρ_b is the average soil bulk density and ρ_w is the density of water, which we assume is 1.000 g cm^{-3}. The average soil bulk density and one standard deviation values is based on samples collected between 19 July to 24 August 2012 in an adjacent field with similar soils (Clain Jones, unpublished data), at depth increments of 0-15 cm (1.271 ± 0.093 g cm^{-3}, n = 59) and 15-30 cm (1.288 ± 0.065 g cm^{-3}, n = 50). Interpolated values for our depth increments were as follows: 1.271 ± 0.094 g cm^{-3} for 0-10 cm, 1.279 ± 0.081 g cm^{-3} for 10-20 cm, and 1.288 ± 0.065 g cm^{-3} for 20-30 cm. The intermediate value 1.279 ± 0.081 g cm^{-3} represents the estimated bulk density for the 10–20 cm depth interval. This value was calculated as a weighted average of the 0–15 cm and 15–30 cm bulk density measurements, with equal weights (5 cm each) assigned to reflect the overlapping contributions of the two intervals to the 10–20 cm layer. Relative uncertainty (%s) was propagated when converting from a gravimetric water content to a volumetric water content at each soil depth:

$$\%s_{\theta v} = \sqrt{\%s_{\theta g}^2 + \%s_{\rho_b}^2} \quad 6$$

where $\%s_{\theta g}$ represents the gravimetric water content relative uncertainty (one standard deviation), and $\%s_{\rho_b}$ represents the soil bulk density relative uncertainty (one standard deviation), both calculated by dividing the standard deviation by the mean.

The height of water (H_w) in each depth increment was determined for each depth increment from the volumetric water content:

$$H_w = \theta_v \cdot H_S \quad 5$$

where H_S is the soil thickness, which is 10 cm for all samples. The total height of water is the sum of water heights in each depth increment.

$$H_t = H_{w,10} + H_{w,20} + H_{w,30} \quad 5$$

where subscript numbers indicate soil collection depths. Relative uncertainty in the height of water for each depth increment was assumed to be identical to the calculated relative uncertainty in the volumetric water content ($\%s_{\theta v}$), and was converted to an absolute uncertainty in the water heights ($s_{Hw} = \%s_{\theta v} \cdot \theta_v$) for propagation of uncertainty in the total height of water:

$$s_{Ht} = \sqrt{s_{Hw,10}^2 + s_{Hw,20}^2 + s_{Hw,30}^2} \quad 7$$

where s_{Ht} represents the absolute uncertainty in the total height of water and subscript digits represent soil collection depths.

Continuous soil moisture data was collected at the Bozeman site using Hydra Probe soil moisture and temperature monitoring devices (Stevens, Portland USA). Probes were deployed at two locations, one in short stubble and one in tall stubble, in the CARB study site (Figure 1B), at the depths of 10 cm and 20 cm. Locations were chosen to coincide with summer fallow crop rotations during the subsequent growing year, so they did not disturb ongoing research. Probes were installed on 12 April and removed on 12 September 2023. Reported observations were averaged to display one soil moisture content representative of soil moisture from 10-20 cm soil interval. At the Moccasin study site, continuous soil moisture data was collected using Sentek Drill and Drop Bluetooth soil moisture and temperature monitoring probes. Probe locations

within the Moccasin producer's field were randomized within the short stubble (n = 6) and tall stubble (n = 5) (Figure 1C). Continuous data were collected from 12 March until 8 April 8 2024, when probes were removed to allow for seeding of field pea at the study site. Probes were then reinstalled and recorded data from 17 May 17 to 29 July 2024. Downloaded data from the sensors were calibrated using Sentek website calibrations for clay loam soils, which is the expected texture at the study site (Figure S5). These observations were averaged for each date across sampling depths of 5, 15, 25, and 35 cm, and across the six field positions. Measurements at 45 and 55 cm were omitted due to potential sensor interference from shallow gravels within the soil profile (Barnes et al., 2025, M.S. Thesis; USDA NRCS, 2021).

3.2.6 Soil water extractions, Moccasin MT

For stable isotope analysis of soil water, we used cryogenic extraction on a pyrex vacuum line in the MSU EAL, following previous methods (West et al., 2006) but with an added equilibration step. Cryogenic extraction was performed to separate liquid water from soil samples by sublimation. Individual frozen soil samples were placed in an arm of the line in their collection vials, brought to vacuum, and isolated by closing a valve while constantly monitoring for pressure. A liquid nitrogen trap was placed on the adjacent arm in the isolated section of line, and the soil was heated to 105 °C using heating packs made with heating cords and heat tape wrapped around the arm to facilitate water sublimation from the soil material and freezing in the liquid nitrogen trap (Ingraham & Shadel, 1992; Orlowski et al., 2016). The liquid nitrogen trap was then removed, allowing the condensed water to thaw, and samples were equilibrated with the residual soil for 14 hr at room temperature, by leaving both the residual soil and the liquid water in the isolated section of line while under pressure (Scott Allen, personal communication).

Extractions generally involved at least 150 min of sample heating prior to the 14 hr of equilibration based on tests using water of known isotopic composition (Figure 3.S5). After the equilibration period, the condensed soil water was removed from the extraction apparatus, transferred to a 2 mL vial with a sealable cap, and stored frozen until isotopic analysis.

Due to the possibility of incomplete extractions potentially influencing the δ^2H and $\delta^{18}O$ values of extracted waters, we quantified isotopic offset from true values using repeat analysis on the cryogenic extraction line. Based on laser diffraction assessment, the clay loam to clay soil texture (Figure 3.S4, Table 3.S1) has relatively high clay content (19.3-51.4%), potentially resulting in stronger influence on the isotopic composition of extracted waters (Table 3.S2). We performed repeat extractions on soil from the study site, which was oven dried for 72 hr at 105° C, spiked with a water of a known isotopic composition, and extracted using our standard protocol (n=11). The extracted water was compared to the known isotopic composition of the spiked water ($\delta^2H = -130.15 \pm 1.12‰$, $\delta^{18}O = -17.54 \pm 0.65‰$,). These experiments yielded an average δ^2H value and one standard deviation of -130.22 ± 6.60‰ and an average $\delta^{18}O$ value and one standard deviation of -16.57 ± 1.28‰ for extracted waters, equal within our uncertainty (one standard deviation) to the known values (Figure 3.S5). We therefore did not correct the observed soil water isotopic compositions but assigned a higher uncertainty to our individual observed values (samples assessed in duplicate have reduced uncertainties).

3.2.6.1 Soil texture classification, Moccasin MT In order to understand how soil clay content influenced the cryogenic extraction results, we evaluated soil texture for the collection intervals of 10, 20, and 30 cm (Figure 3.S4, Table 3.S1). Clays are known to fractionate water isotopes when they bind water (E. Oerter et al., 2014), making cryogenic extraction incomplete

and isotopically distinct (Millar et al., 2022). Soil texture was analyzed using a Malvern Mastersizer 3000 (Malvern Panalytical, Worcester United Kingdom), which uses laser diffraction techniques to provide a continuous particle size distribution. Soil samples were riffle split, allowing for subdivided representative soil samples, into roughly 15-g sub-samples. From this sub-sample, we sieved (<2 mm) 2 g into a 50 mL digestion tube. The tube was then filled with 50 mL of sodium hexametaphosphate and placed on a platform shaker (Innova 2000, Edison USA) for 12 h at 320 rpm. Soil samples at each depth interval represent the average result from six different samples, collected at each sampling point within the producer's field (S1, S2, S3, S4, S5, and S6). Values occasionally did not add up to 100% for clay, silt, and sand particles, due to some particles being misinterpreted as larger than 2 mm (Table 3.S1). We report percentages of clay as soil particles between 0-6 μm, silt as 6-50 μm, and sand as 50-2,000 μm, common practice for laser diffraction soil particle analysis due to underestimates of clays <2 μm (Schaetzl & Thompson, 2015).

3.2.7 Analysis of isotopic ratios, Moccasin MT

Water samples were analyzed for oxygen and hydrogen isotopic composition ($\delta^{18}O$ and $\delta^{2}H$) using integrated cavity output spectroscopy (ICOS; Los Gatos Research; Mountain View, USA) in the MSU EAL. The instrument first reports the relative isotopic compositions of the hydrogen and oxygen atoms in water as atomic mass ratios of $^{2}H:^{1}H$ and $^{18}O:^{16}O$, respectively. These values are then normalized to their corresponding δ values based on deviation from the global water standard (Vienna Standard Mean Ocean Water, VSMOW) (Craig, 1961; Dansgaard, 1964), reported as a fractional deviation (‰). Analytical uncertainty was constrained using sealed USGS-certified standards 46 ($\delta^{18}O = -29.80‰$ and $\delta^{2}H = -235.80‰$), 47

($\delta^{18}O = -19.80‰$ and $\delta^{2}H = -150.20‰$), two MSU EAL working standards ($\delta^{18}O = -19.04‰$ and $\delta^{2}H = -149.41‰$, $\delta^{18}O = -19.04‰$ and $\delta^{2}H = -149.41‰$), and LGR working standard #3C ($\delta^{18}O = -13.39‰$ and $\delta^{2}H = -97.3‰$). Analytical memory was accounted for in analyzed samples to minimize its effects. Additionally, using USGS and LGR standards, a correction was applied for machine drift throughout a run using internal lab correction processes similar to previously implemented strategies (Gröning, 2011). Repeated observations of the two MSU EAL working standards run with the samples, one from a local groundwater sample near Bozeman, Montana (n = 43, $\delta^{18}O = -19.04‰$ and $\delta^{2}H = -149.41‰$), and the second from a snow sample collected near Big Sky, Montana, (n=31, $\delta^{18}O = -17.54‰$ and $\delta^{2}H = -130.15‰$), had standard deviations of ±1.12‰ for $\delta^{2}H$ and ±0.65‰ for $\delta^{18}O$ values, providing an estimate of analytical uncertainty associated with the samples. We combine these analytical uncertainties with those associated with the cryogenic extraction process using the following equation:

$$s_{TU} = \sqrt{s_{AU}^2 + s_{CU}^2} \qquad 8$$

where s_{AU} is the machine derived uncertainty (one standard deviation), s_{CU} is the uncertainty associated with the cryogenic extraction process (one standard deviation), and s_{TU} is the total combined absolute uncertainty. This results in a combined absolute uncertainty of ±6.69‰ for $\delta^{2}H$ and ±1.44‰ for $\delta^{18}O$ for individual cryogenically extracted soil water samples.

Mean $\delta^{18}O$ and $\delta^{2}H$ values were determined for precipitation data collected from 2012-2022, and fit to sinusoidal model (Mayernik et al., 2024). This resulting model was used to interpolate the isotopic composition of precipitation throughout the year in this study and calculate a volume-weighted annul mean (VWAM) precipitation $\delta^{18}O$ and $\delta^{2}H$ values for the period of 2012-2022 (Mayernik et al., 2024) for comparison to sample results.

3.2.7.1 Assessing evaporative effects on soil water, Moccasin MT We used a previous assessment of the local meteoric water line (LMWL) for this area (Mayernik et al., 2024) based on the isotopic composition of precipitation collected at the CARC from 2012-2022 using the following equation (Dansgaard, 1964):

$$\delta^2 H = m \cdot \delta^{18} O \ + b \quad (9)$$

where m and b are derived based on the linear regression of local precipitation δ^2H compared to $\delta^{18}O$ values. To assess meaningful deviation of water from the LMWL, a Monte Carlo analysis was conducted, using analytical uncertainty values associated with precipitation values used to calculate the LMWL, to establish the 95% confidence interval (Leuthold et al., 2021; Mayernik et al., 2024).

Water is influenced by evaporation at shallow soil depths (Mayernik et al., 2024; Sprenger et al., 2016), which favors loss of water molecules containing lighter isotopes of hydrogen and oxygen. Due to evaporation favoring the conversion of the molecularly lighter water containing deuterium ($^1H^2H^{16}O$) more readily than molecularly heavier water containing ^{18}O ($^1H_2{}^{18}O$), residual waters plot to the right of the LMWL (Craig et al., 1963). The deviation of the relationship between the δ^2H and $\delta^{18}O$ of a water sample compared to the average isotopic composition derived from the LMWL allows for assessment of evaporative effects on the water sample, using line-conditioned excess (lc excess) (Landwehr & Coplen, 2006):

$$lc\ excess = \delta^{2H} - m \cdot \delta^{18O} + b$$

where m and b represent the slope and intercept of the LMWL (m = 7.14 and b = -10.4‰ at Moccasin). More negative lc excess values suggest a greater influence of evaporative fractionation in a water sample, relative to local precipitation (Sprenger et al., 2016).

3.3 Results

3.3.1 Meteorological data, Bozeman and Moccasin MT

In 2022-2023 at the Bozeman study site (Figure 3.3), snow depth was persistent, with an average snow depth of 38.3 cm from the end of November through March. Then on 25 March 2023 a large storm increased the snow depth to a maximum value of 74.5 cm. Following this event, a gradual decrease in snow depth was followed by a large increase in soil moisture values, at all depths, to a maximum soil volumetric water content of 39.45% at 10 cm and 35.13% at 20 cm on 11 April and 30.29% at 50 cm on 17 April. Manual assessment of snow depths adjacent to the meteorological monitoring station at the Hort farm produce an average difference from the continuously monitored snow depths of 3.3 cm.

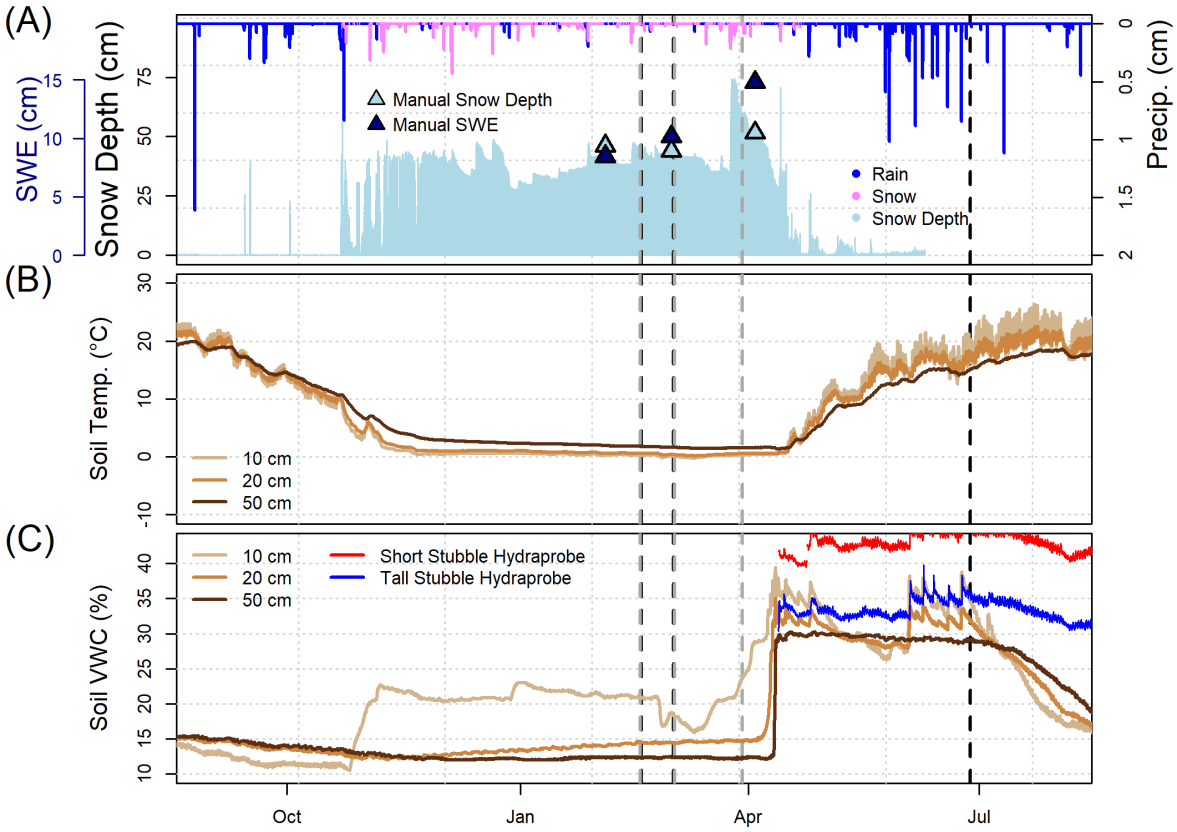


Figure 3.3: Precipitation and soil meteorological data during soil collection period, from September 2022 through July 2023, at the Bozeman Horticulture (Hort) Farm Mesonet site (Montana Climate Office, 2025). (A) Hourly snow depth and precipitation as snow or rain based on temperature. Precipitation data are dark blue to represent rainfall, when air temperature is >0 °C, and pink for snow, when air temperature is <0 °C. Vertical dashed lines represent sampling events, with grey lines indicating manual snow sampling and black indicating associated LiDAR drone flights. Triangles represent manual observations of snow depth (light blue) and snow water equivalent (navy), respectively, adjacent to the meteorological station. (B) Soil temperature at the depths of 10, 20, and 50 cm. (C) Soil volumetric water content at 10, 20, and 50 cm depths. Red (short stubble) and blue (tall stubble) indicate average measured volumetric water content, from 10-20 cm, in the two plots at the CARB study site.

In 2023-2024 at Moccasin, extended dry conditions included no precipitation from mid-December to mid-January (Figure 3.4). During this month the average air temperature was 4.8 °C, warmer than the historical normal (1991-2020) for December (-3.4 °C) and January (-3.7 °C) (PRISM Climate Group, 2023). Between September 2023 and July 2024, approximately 83.3%

of the total precipitation at the nearby CARC fell as rain, with snow contributing the remaining 16.7%. During this period 43.3% of total precipitation fell between the months of May through June, consistent with historic patterns. Snow dynamics varied from the previous sampling winter in Bozeman, with three observed small snowfall events, on 24 October 2022 (max = 23.3 cm), 12 January 2023 (max = 14.9 cm), and 13 February 2023 (max = 7.6 cm). The highest recorded SWE value during this time period was 4.2 cm, recorded 9 May 2024, while SWE values greater than 0.1 cm were only recorded for a period of eight days (12 February to 20 February 2024), indicating a highly ephemeral snowpack during this study period (Figure 3.4).

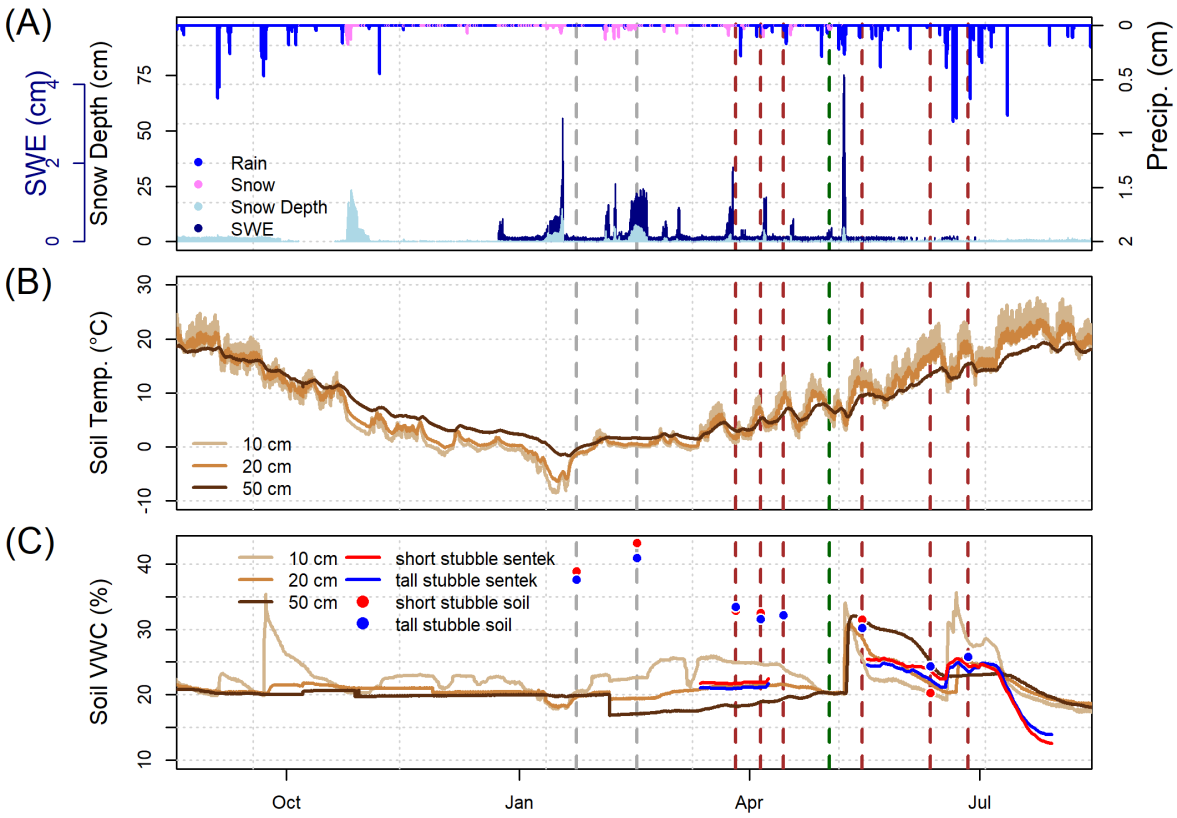


Figure 3.4: Precipitation and soil meteorological data during soil collection period, from September 2023 through June 2024, at the Central Agricultural Research Center (CARC) Mesonet site (Montana Climate Office, 2025). (A) Hourly snow depth, snow water equivalent (SWE) measured with a snow scale, and precipitation as snow or rain based on temperature. Precipitation data is blue to represent rainfall, when air temperature is >0 °C, and pink for snow,

when air temperature is <0 °C. Grey vertical dashed lines reflect combined snow and soil sampling events, brown only soil sampling, and green indicated field pea sampling date. (B) Soil temperature at the depths of 10, 20, and 50 cm. These depths were chosen to reflect general sampling depths of soil collection protocol. (C) Soil volumetric water content at 10, 20, and 50 cm depths. Red (short stubble) and blue (tall stubble) indicate average measured volumetric water content, from 0-35 cm, within the Moccasin producers' field. Points reflect average volumetric water content, based on total water from 0-30 cm, averaged across three bulk soil samples collected in the field, in the short (red) and tall (blue) stubble.

Soil volumetric water content (Figure 3.4C) increased in early fall (+15.53% at 10 cm) due to precipitation events on 21 and 22 September 2023. Soil water content values following this point remained relatively consistent at all depths until a gradual increase, primarily at 10 cm (+4.58%), near the end of January, due to snow melt. Then, as spring precipitation events began to increase in May 2024, soil water content increased at all depths, with a maximum of 35.6% at 10 cm on 21 June 2024. Starting in May 2024, evaporation and transpiration outpaced precipitation inputs, indicated by a gradual decline in soil water content. However, due to increased precipitation during this period, the maximum soil volumetric water content of the growing season (35.6%) also occurred. Soil temperature values during the study period followed expected seasonal trends of cooling and warming but were frozen only for a relatively short period during the winter (December-February 2024) of 33 days (Figure 3.4).

3.3.2 Snow depth and water content, Bozeman and Moccasin MT

Throughout both winter field sampling campaigns, we sampled snow five separate times, three times at the Bozeman study site, and twice at the Moccasin site (Table 3.2).

Table 3.2: Summary statistics of manually measured snow depth (cm) and SWE (cm) values sampled in Bozeman (2022-2023) and Moccasin (2023-2024).

Location	Date	Treatment	Snow Depth (cm)			SWE (cm)		
			n	Mean	SD	n	Mean	SD
Bozeman, MT	2/17/2023	Short	19	32.1	2.8	19	8.1	2.9
		Tall	20	41.3	2.5	20	10.6	2.3
	3/2/2023	Short	36	21	4	36	5.7	2.4
		Tall	36	34.4	3.9	36	10.5	2.5
	3/29/2023	Short	18	37.8	4.6	18	7.3	3.1
		Tall	19	38.9	2.5	19	5.8	1.9
Moccasin, MT	1/23/2024	Short	9	2.7	1.2	NA	NA	NA
		Tall	18	4.9	1.2	18	2.3	0.5
	2/16/2024	Short	24	12.9	2.1	24	1.5	0.9
		Tall	17	13.4	0.9	17	1.9	0.6

On two of the three reported sampling dates (17 February and 2 March 2023) at the Bozeman study site, higher confidence (p-value<0.05) was associated with difference in mean or median snow depth accumulation and SWE values between short and tall stubble (Figure 3.5A,B). Differences on 17 February and 2 March were observed during a period of relatively uniform snowpack during the winte of 2022-23 in Bozeman (Figure 3.3A). However, on 29 March, no difference in mean snow depth and median SWE values were observed as a function of stubble height at the Bozeman site (Figure 3.5C), due to the large snow storm event on March 25 (Figure 3.3A).

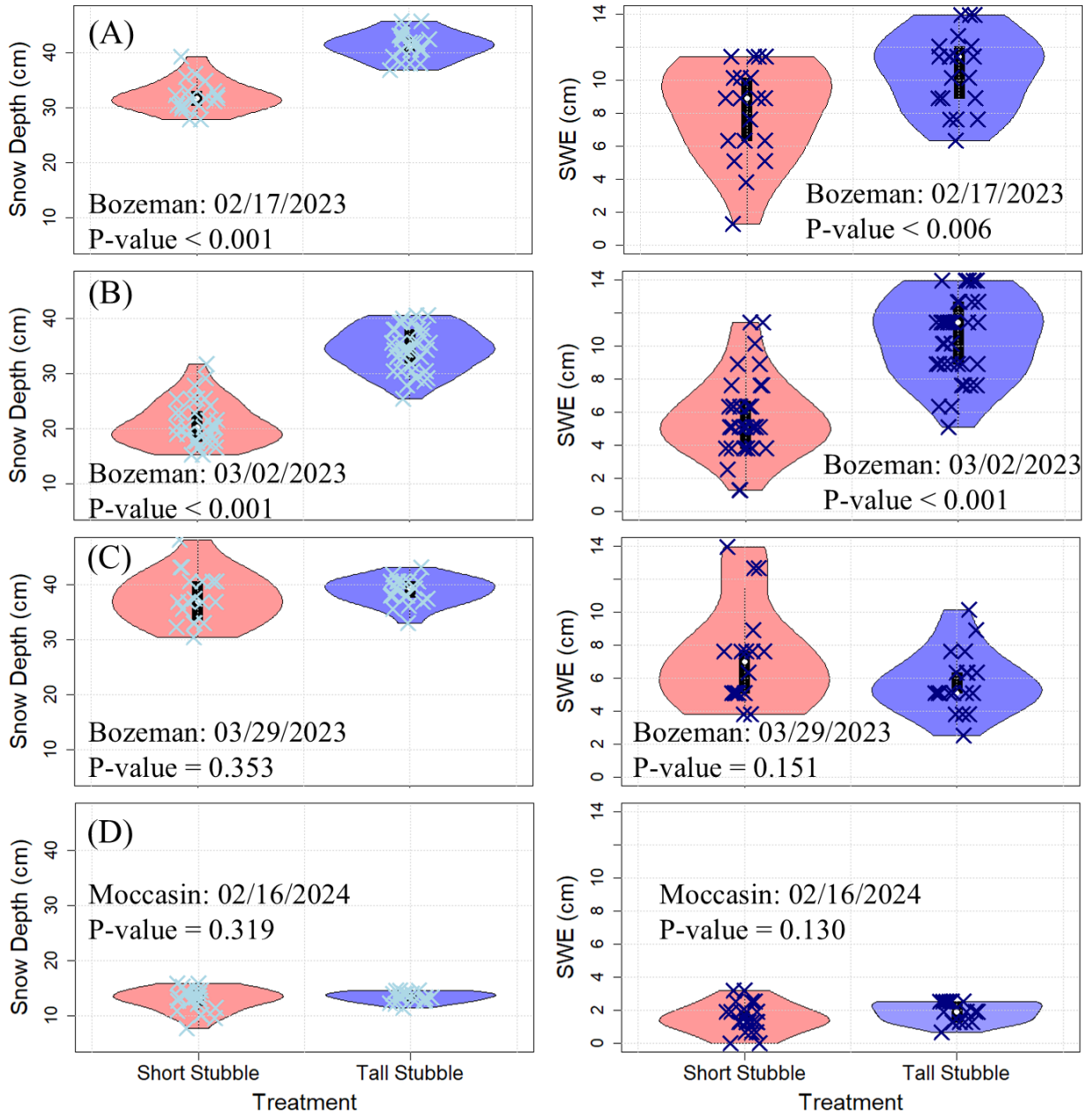


Figure 3.5: Snowpack information collected at the Bozeman and Moccasin study sites. Reported p-value reflects confidence from either t-test, assuming normality, or Wilcoxon rank sum test, when normality is violated. (A) Snow depths (cm) and SWE (cm) in short and tall stubble at the Bozeman field site 17 February 2023. (B) Snow depths (cm) and SWE (cm) in short and tall stubble at the Bozeman field site 2 March 2023. (C) Snow depths (cm) and SWE (cm) in short and tall stubble at the Bozeman field site 29 March 2023. (D) Snow depths (cm) and SWE (cm) in short and tall stubble at the Moccasin producers' field site 16 February 2024. Observed SWE

(cumulative mean = 1.70cm) is slightly larger than the snow scale reading (~1.23 cm) on this date in Figure 4C.

LiDAR derived snow depths collected 17 February and 2 March 2023 are fairly consistent with manually observed data points and suggest accumulation of snow in tall stubble as compared to short stubble (Figure 3.6, Table 3.2). On 17 February, tall stubble exhibited an average increase of 6.9 cm in LiDAR-derived snow depth and 1.8 cm in SWE compared to short stubble. On 2 March, tall stubble had 8.8 cm greater snow depth and 2.6 cm greater SWE on average compared to short stubble.

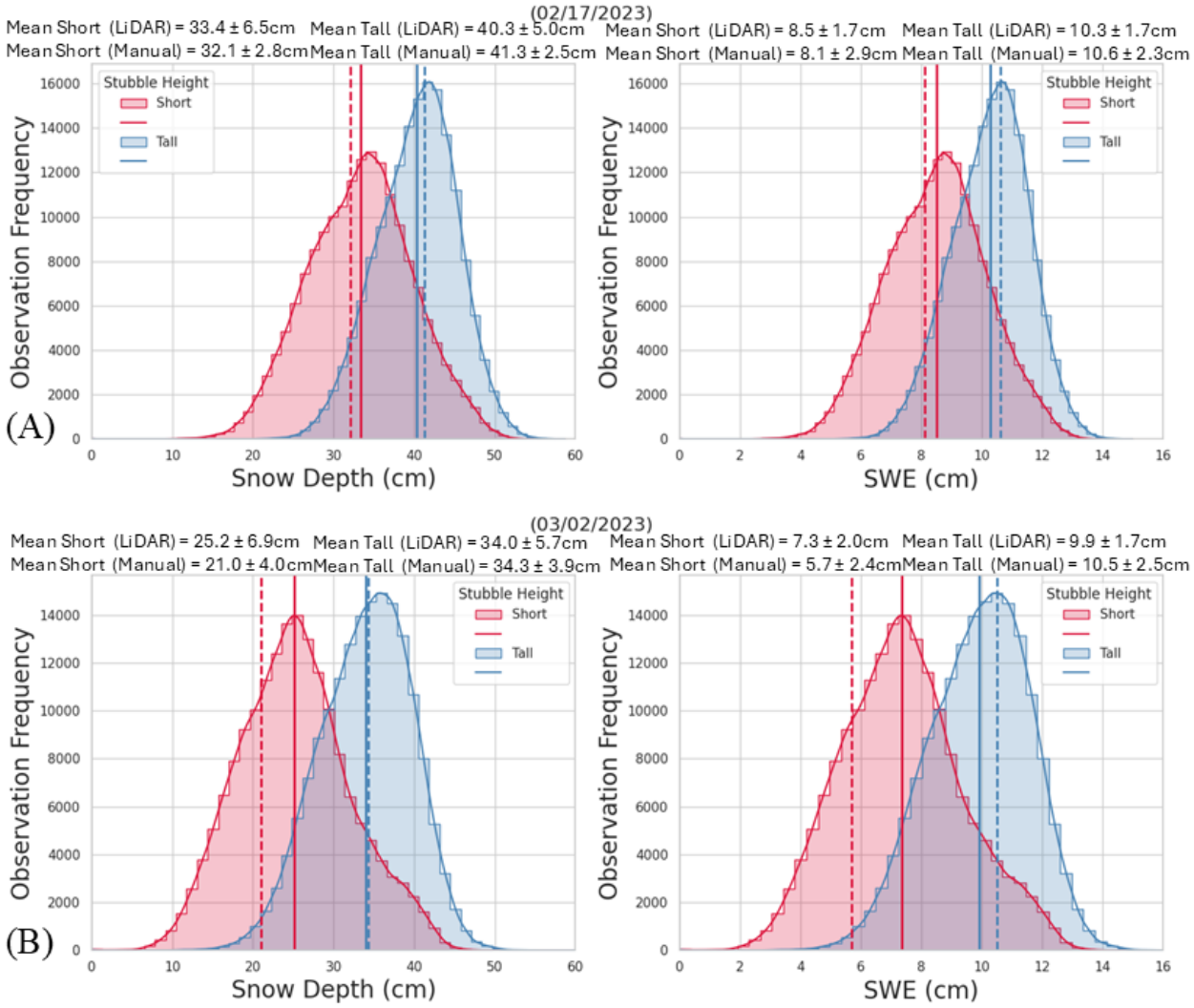


Figure 3.6: LiDAR derived distribution of snow depth (cm) and SWE (cm) values within short (red) and tall (blue) stubble at the Bozeman study site. Observation frequency represents number of LiDAR derived point estimates. Solid line depicts LiDAR derived mean snow depth and SWE values while the dashed line indicates manually measured mean snow depth and SWE values. Mean values for each group reflected on the top of each graph along with associated uncertainty (one standard deviation). (A) Snow pack analysis 17 February 2023. (B) 2 March 2023.

Snow was limited during 2023-2024 at Moccasin (Table 3.2, Figure 3.5D), with successful sampling events on two dates, 23 January and 16 February, 2024. In January, median snow depth accumulation differed between tall and short stubble treatments (Wilcoxon rank sum test, p-value < 0.001) but SWE values in the short stubble were uncertain (Table 3.2) due to

patchy snow distribution (Figure 3.7B). Spatially variable snowpack dynamics were captured using RGB imaging (Figure 3.7A) on this date. The orthomosaic image resulted in a cover of 66% within tall stubble and a cover of 22% amongst short stubble, with a 98.5% validation accuracy of pixels (Figure 3.7B).

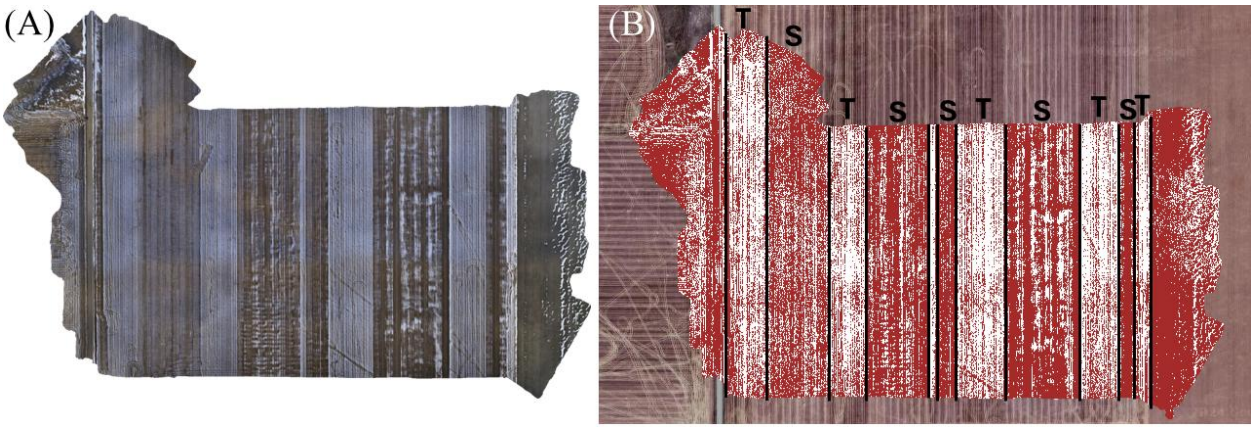


Figure 3.7: Snow cover across Moccasin producers' field 23 January 2024. (A) Orthomosaic RGB image of producer's field, captured via drone. (B) Radom forest model assessment of snow-covered area (white) and bare soil (red) based on orthomosaic image. Tall and short stubble divides marked as S and T lettering at top of image.

Deeper snowpack on 16 February 2024 allowed for assessment of both snow depth and SWE values in short and tall stubble at Moccasin (Table 3.2, Figure 3.5D). On this sampling date both the snow depth and SWE were nominally greater in the tall stubble as compared to the short stubble but did not differ in mean snow depth (t-test, p-value > 0.05) and median SWE values (Wilcoxon rank sum test, p-value > 0.05) (Figure 3.5D). Snow depth (s = 2.081 cm) and SWE (s = 0.911 cm) exhibited greater variability in the short stubble compared to the tall stubble (snow depth s = 0.937 cm, SWE s = 0.614 cm), suggesting more consistent snowpack conditions within the tall stubble treatment (Figure 3.5D).

3.3.3 Seasonal variation in soil water content, Bozeman and Moccasin MT

Soil volumetric water content was measured in Bozeman at two locations within short and tall stubble, representing an average soil water content between measurements at 10 cm and 20 cm (Figure 3.1B). Water content monitored in the tall stubble followed patterns similar to measurements recorded at the nearby Hort farm Mesonet site at 10 and 20 cm, until the beginning of July, when water content dropped rapidly in the reported Mesonet data but not in the tall stubble water content. This indicates soil water losses to transpiration at the Mesonet location, not observed in the tall stubble as the plot was in a summer fallow rotation (Figure 3.3C). Values monitored in the short stubble were continuously greater than measurements in both the tall stubble and the Mesonet site, often greater than 40% reported volumetric water content (Figure 3.3C). We believe this is likely caused by some error during instillation or calibration issue, and data should be considered untrustworthy.

Water content at the Moccasin field site (2024) was monitored via two approaches: continuously recorded volumetric water content (Sentek Drill and Drop Bluetooth soil moisture probes) and by assessing bulk soil water content on soil sampling collection dates (n = 8). Averaged Sentek results (six positions, four depths) prior to planting (12 March – 8 April 2024) plot similarly to measured volumetric water content recorded at 20 cm at the nearby CARC Mesonet station (Figure 3.4C). These similarities are expected as the reported in field volumetric water content reflects the average water content across the depth intervals of 5, 15, 25, and 35 cm. Short stubble water content (n=6) consistently remains nominally higher than the tall stubble (n=6) during this pre-planting period, with confidence that the distributions have different median values (Wilcoxon rank sum test, p-value < 0.005). This difference is unexpected and may

be caused by potential probe reading error due to poor contact with soil during this period, or trampling of tall stubble during instillation.

During the growing season collection period (17 May – 29 July 2024) soil water content, reported by the Sentek probes, increased during the start of the collection period when compared to the values reported at the end of the pre-planting period (Figure 3.4C) (+2.93%). This reflects increased precipitation in early May and follows similar trends to the recorded Mesonet data (Figure 3.4C). Following seeding of field peas on 2 May, the soil volumetric water content is initially higher than reported values prior to planting, due to increased precipitation inputs. Then, volumetric water content begins to gradually decline in both the short and tall stubble, until a dramatic reduction in soil volumetric water content on 7 July (-10.33%), signaling uptake of soil water by the crop during the peak growing season. We lack confidence that the distributions have different median values between the short and tall stubble Sentek measurements during this period (Wilcoxon rank sum test, p-value > 0.05).

Manually assessed soil water content gradually diminished during the sampling collection period at the Moccasin site (Figure 3.9). When compared to continuously recorded soil moisture contents by the infield Sentek probes we see fairly comparable data on the sampling dates of 15 May, 11 June (-0.73%), and 29 June (1.90%) 2024, but larger discrepancies on the other six manual sampling dates between January and April 2024 (Figure 3.4C), with manual measurements resulting in consistently higher average water contents (10.55% to 11.75%). Discrepancies may reflect soil temperatures below 0 °C that interfere with the detection of liquid water using sensors, or inclusion of snow in the bulk soil samples when snow is present at the study site (Table 3.2), leading to higher water content values in manually collected samples

(Table 3.3, Figure 3.9). Additionally, during early spring sampling events (26 March, 4 April, and 14 April 2024) increased soil water content in manually collected samples may reflect infiltration of small amounts of spring precipitation (rain or snowmelt), which may elevate shallow water contents but not reach the depth of the sensors or influence the sensor averages (Figure 3.4C, Figure 3.9).

Table 3.3: Total height of water across the sampled soil profile. Total height of water calculated by adding the height of water from 0-10, 10-20, and 20-30 cm on each date for each stubble height treatment. Difference calculated tall minus short, where negative values indicate less water in tall. The three largest absolute differences in soil water storage are bolded.

Collection date	**Treatment**	**Total soil water (cm water)**	**Propagated uncertainty (cm water)**	**Difference in storage (cm water)**
1/23/2024	Short Stubble	11.66	0.62	-0.38
	Tall Stubble	11.28	1.27	
2/16/2024	Short Stubble	12.95	0.94	**-0.67**
	Tall Stubble	12.28	0.68	
3/26/2024	Short Stubble	9.87	0.59	0.16
	Tall Stubble	10.02	0.49	
4/5/2024	Short Stubble	9.76	0.37	-0.28
	Tall Stubble	9.48	0.38	
4/14/2024	Short Stubble	9.66	0.50	0.01
	Tall Stubble	9.66	0.53	
5/15/2024	Short Stubble	9.45	1.07	**-0.39**
	Tall Stubble	9.06	0.41	
6/11/2024	Short Stubble	6.08	0.54	**1.22**
	Tall Stubble	7.30	0.45	
6/26/2024	Short Stubble	7.76	0.40	-0.03
	Tall Stubble	7.73	0.36	

In our manual observations of soil water, the area-normalized volume of water within the sampled soil profile is highest in both the short and tall stubble during winter sampling events, 23 January (Short = 11.66 cm water, Tall = 11.28 cm water) and 16 February (Short = 12.95 cm water, Tall = 12.28 cm water) and lowest 11 June (Short = 6.08 cm water, Tall = 7.30 cm water) (Table 3.3, Figure 3.9). We record the lowest soil water content during sampling events in June when evaporation and transpiration likely outpaced precipitation inputs, during peak crop growth (Figure 3.8, 3.9).

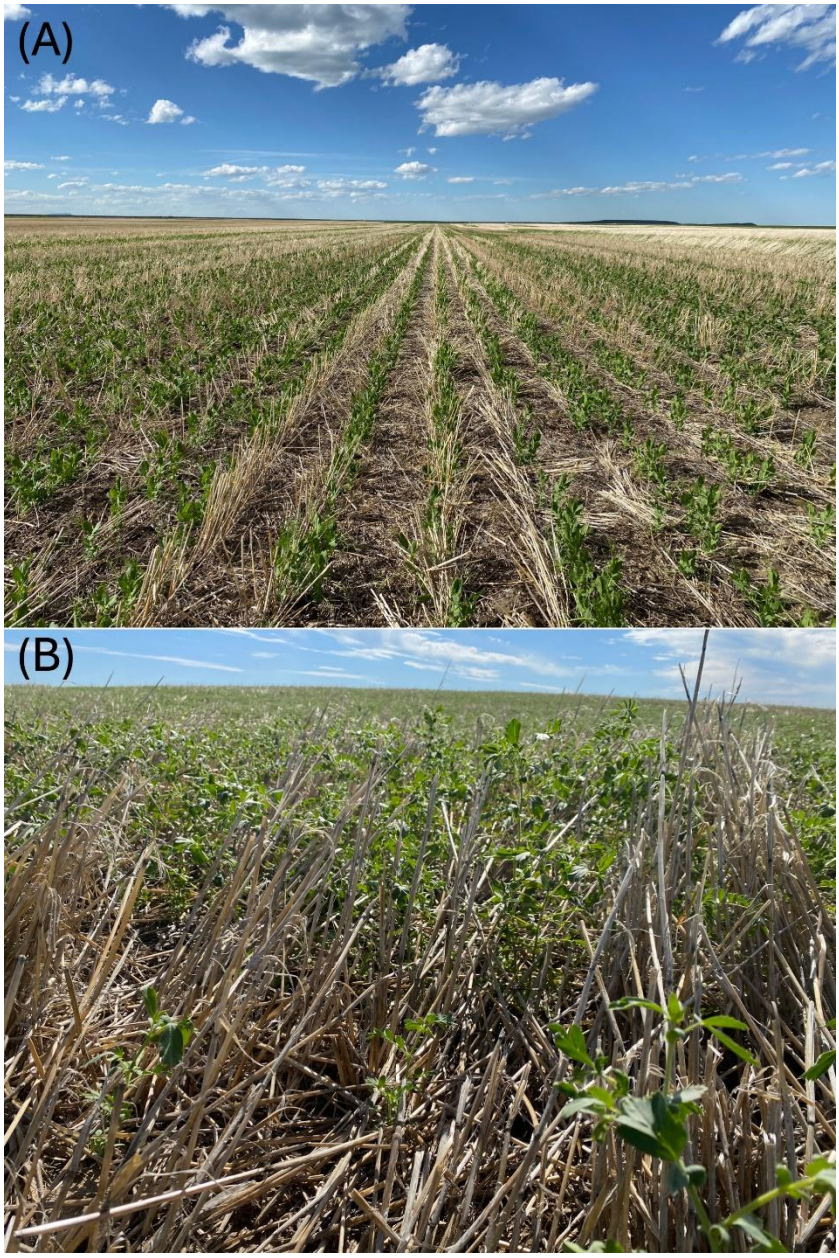


Figure 3.8: Field pea crop growing conditions. (A) Crop growth on 11 June 2024. Picture captures crop growth, prior to flowering, in short stubble at the Moccasin field site. Plant height was roughly 10-20 cm during this time. (B) Crop growth on 26 June 2024. Picture captures crop growth in tall stubble at the Moccasin field site. Plant height was roughly 50-60 cm on this date (Visual estimate).

On 11 June 2024 we record the largest difference between short and tall stubble soil water height (1.22 cm water), nearly double the second closest absolute difference on 26 February (-

0.67 cm water), with more water in the tall stubble on this specific date (Table 3.3, bolded, Figure 3.9). The total height of water in the soil profile is distinct between short and tall stubble on 11 June with no overlap in the propagated uncertainty associated with the total height of water calculation (Figure 3.9, eq.7). On all other collection dates, propagated uncertainty in the total height of water overlaps between the short and tall stubble (Figure 3.9, Table 3.3), suggesting no discernable difference in water heights between the short and tall stubble.

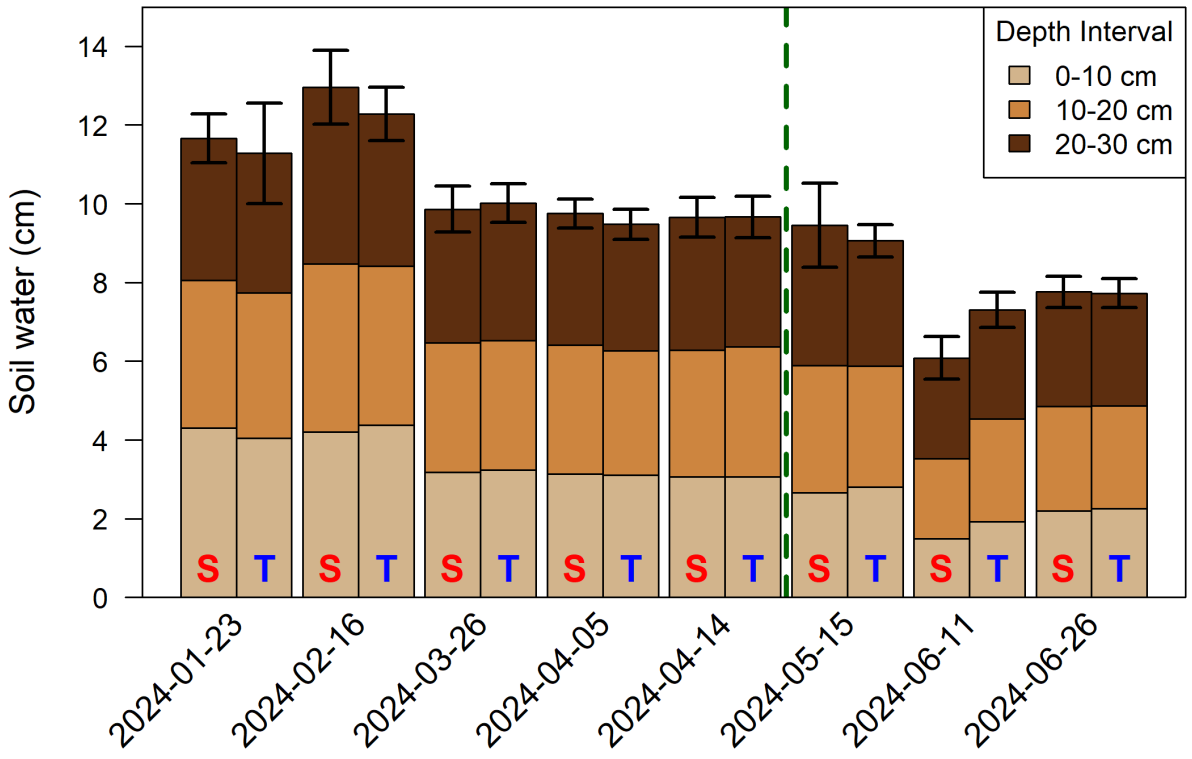


Figure 3.9: Soil water within the top 30 cm of the soil profile, by sample collection date. Samples at each depth interval (0-10, 10-20, 20-30 cm) reflect an average value from three different locations in tall stubble (S1, S2, and S3) and short stubble (S4, S5, S6). Error bars indicate propagated uncertainty associated with calculating the total height of water by summing the three depth intervals. Field pea planting indicated by vertical green dotted line (2 May 2024).

When comparing mean soil water height, at individual sampling depths by collection date, we observed the largest absolute difference between short and tall stubble (-0.615 cm

water) at 30 cm depth on 16 February (Table 3.4, bolded, Figure 3.9), with more water in the short stubble. The second and third largest differences occurred on 11 June at 0-10 cm (0.443 cm water) and at 20-30 cm (0.554 cm water) (Table 3.4, bolded, Figure 3.9). The mean height of water, for individual sampling depths, did not discernably differ on any collection date between short and tall stubble.

Table 3.4: Summary statistics of soil water height by depth collection interval and stubble treatment type, on each collection date. Difference calculated tall minus short, where negative values indicate less water in tall. The three largest absolute differences in soil water storage are bolded. There is low confidence that the mean values were different between short and tall stubble at any individual depth on any day.

Collection date	**Depth interval (cm soil)**	**Soil water tall stubble (cm water)**			**Soil water short stubble (cm water)**			**Difference in storage (cm water)**
		Mean	**SD**	**n**	**Mean**	**SD**	**n**	
	0-10	4.05	0.85	3	4.31	0.32	3	-0.26
	10-20	3.69	0.73	3	3.74	0.30	3	-0.05
1/23/2024	20-30	3.54	0.43	3	3.61	0.05	3	-0.07
	0-10	4.38	0.28	3	4.21	0.16	3	0.17
	10-20	4.04	0.21	3	4.27	0.31	3	-0.23
2/16/2024	20-30	3.86	0.36	3	4.48	0.73	3	**-0.61**
	0-10	3.24	0.10	3	3.18	0.12	3	0.06
	10-20	3.29	0.14	3	3.29	0.26	3	-0.01
3/26/2024	20-30	3.50	0.29	3	3.39	0.37	3	0.11
	0-10	3.11	0.06	3	3.14	0.08	3	-0.03
	10-20	3.15	0.12	3	3.27	0.04	3	-0.12
4/5/2024	20-30	3.21	0.10	3	3.35	0.07	3	-0.14
	0-10	3.07	0.07	3	3.06	0.07	3	0.01
	10-20	3.30	0.26	3	3.22	0.22	3	0.08
4/14/2024	20-30	3.29	0.30	3	3.37	0.28	3	-0.08

Collection date	Depth interval (cm soil)	Soil water tall stubble (cm water)			Soil water short stubble (cm water)			Difference in storage (cm water)
		Mean	SD	n	Mean	SD	n	
5/15/2024	0-10	2.80	0.11	3	2.66	0.64	3	0.14
	10-20	3.07	0.12	3	3.24	0.44	3	-0.17
	20-30	3.19	0.20	3	3.56	0.65	3	-0.37
6/11/2024	0-10	1.93	0.33	3	1.49	0.20	3	**0.44**
	10-20	2.60	0.09	3	2.05	0.41	3	**0.55**
	20-30	2.77	0.12	3	2.55	0.20	3	0.23
6/26/2024	0-10	2.26	0.13	3	2.20	0.09	3	0.06
	10-20	2.62	0.05	3	2.66	0.22	2	-0.05
	20-30	2.86	0.19	3	2.90	0.16	3	-0.04

3.3.4 Soil water isotopic composition, Moccasin MT

Seasonal trends of soil water isotopic values at the Moccasin study site (2024), followed expected seasonal patterns, based upon precipitation inputs, within the top 0-10 cm of the soil profile, indicated by a positive relationship between sampling time and δ^2H value (Figure 3.10B). General trends of soil water isotopic composition at 10-20 cm and 20-30 cm indicate values become more negative between winter and summer, indicating in-mixing of snow and colder precipitation to greater depths over time (Figure 3.10C,D).

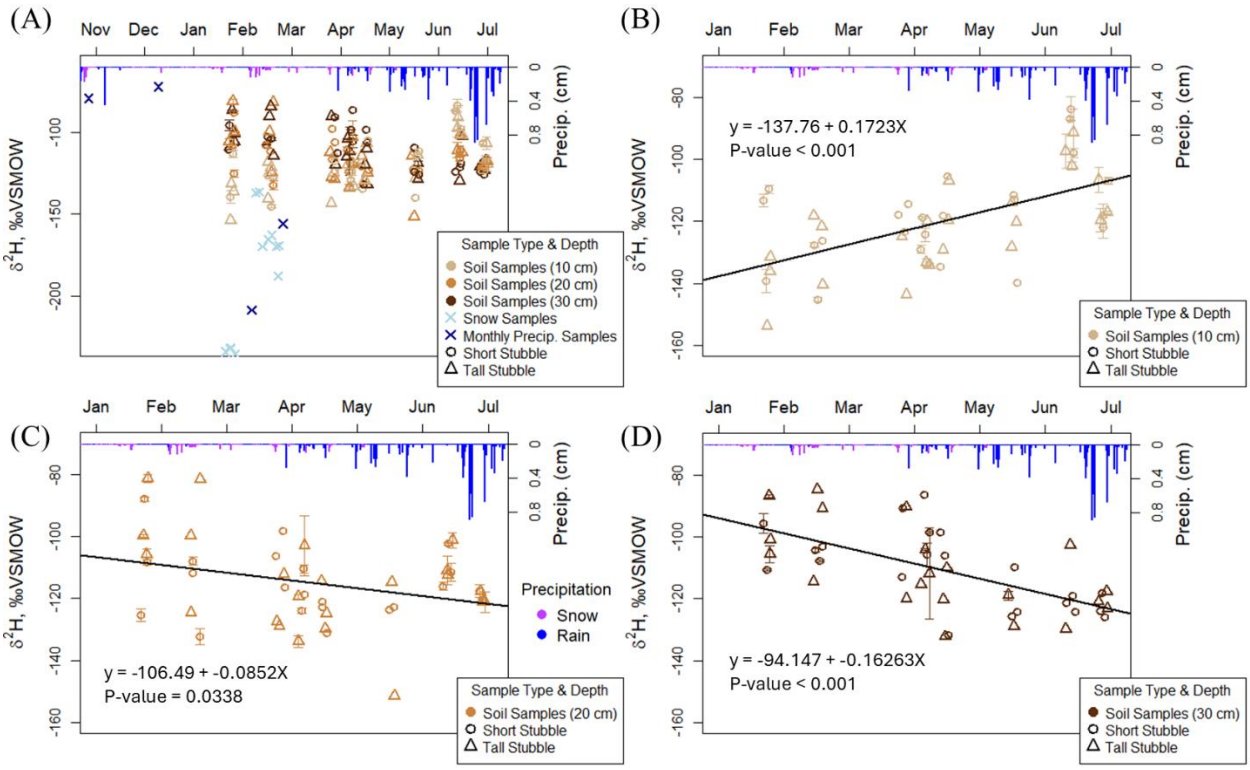


Figure 3.10: Seasonal trends (January through June 2024) of terrace soil water δ^2H values. (A) All soil water δ^2H values samples during sampling period. Soil samples from short stubble indicated as open circles and tall stubble as open triangles. Precipitation values marked as crosses in dark blue for monthly precipitation sampler collected at the Central Agricultural Research Center and as snow in light blue. (B) Soil water δ^2H values at a collection depth of 0-10 cm. Black line represents best fit trend line of soil water values. (C) Soil water δ^2H values at a collection depth of 10-20 cm. (D) Soil water δ^2H values at a collection depth of 20-30 cm.

Although a limited number of observations prevents assessment of significance, we observed the largest difference in mean isotopic values between short and tall stubble treatments on 23 January at 0-10 cm depth (Figure 3.10B). Soil water δ^2H values at 0-10 cm depth are more negative in tall stubble (m = -140.5‰, s = 11.68‰) as compared to short stubble (m = -120.73‰, s = 16.19‰) (Table 3.S2).

Soil water isotopic composition varied with soil sampling depth and treatment type (short or tall stubble). At shallow depths (0-10 cm) δ^2H values (m = -119.96‰, s = 15.18‰) exhibit

greater variability (range of -153.78‰ to -83.60‰) across sampling events compared to greater depths (20-30 cm) where δ^2H values (m = -110.99‰, s = 13.27‰), show lower variability (range of -132.27‰ to -84.63‰) (Figure 3.11A). Additionally, δ^2H values (m = -119.96‰) are lower at shallow depths (0-10 cm) compared to deeper soil depths (m = -111.78‰) (Figure 3.11A). When comparing depth trends, the mean δ^2H values at 0-10 and 20-30 cm depths differed (t-test, p-value < 0.005), but did not differ between soil depths 10-20 cm and 20-30 cm or 0-10 cm and 10-20 cm (p-value > 0.05) (Table 3.S2, Figure 3.11A). When assessing stubble height influence on soil water δ^2H values, the mean values for the two groups did not differ (t-test, p-value > 0.05) (Figure 3.11C), with slightly greater variability within the tall stubble (s = 15.70‰), as compared to short stubble (s = 13.19‰) (Figure 3.11C).

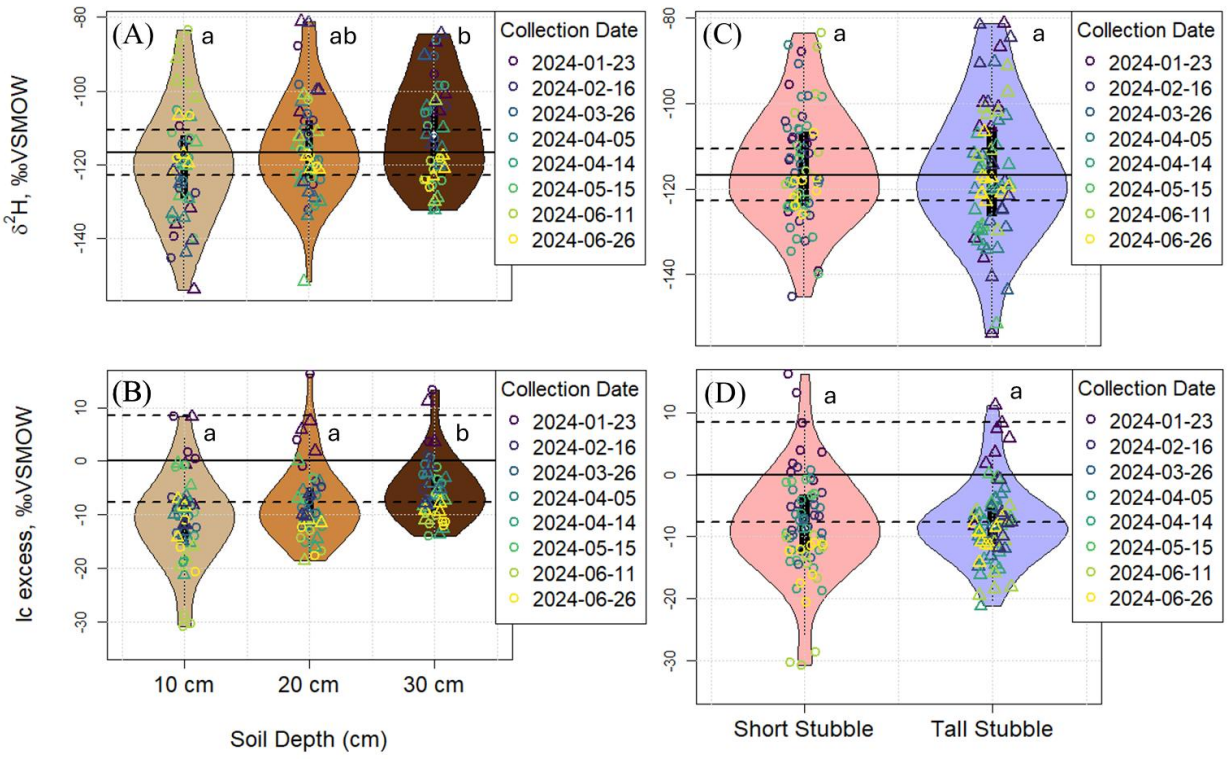


Figure 3.11: Soil water isotopic composition with depth trends. Groups that share the same lower-case letter represent a lack in confidence that the distributions have different means. (A) δ^2H values for each depth interval at 0-10, 10-20, and 20-30 cm depths. The solid black line represents the multi-year (2012-2022) volume-weighted mean (VWAM) δ^2H precipitation value with uncertainty reflecting variance in precipitation at the CARC (Mayernik, et al., 2024). Color corresponds to collection date and the symbol corresponds to stubble treatment, with open circles as shorter stubble and open triangles as tall stubble. (B) Lc excess values of soil water at each depth interval. The solid black line represents the LMWL and the dashed lines reflect the 95% confidence interval around this established LMWL (Mayernik, et al., 2024). (C) δ^2H values grouped by stubble height, including VWAM line indicated in black. (D) Lc excess values grouped by stubble height.

Isotopic deviation from the LMWL indicates the extent of evaporation expressed by a water sample. We infer meaningful influence from evaporation when paired δ^2H and $\delta^{18}O$ soil samples fall below the 95% confidence interval of the LMWL (Figure 12), and when negative lc excess values fall below the 95% confidence interval (Figure 11B,D). Lc excess value of soils sampled at shallower depths (0-10 cm) exhibited more variability (s = 8.43) and had a more

negative mean value (m = -10.27) as compared to soils sampled from 20-30 cm (s = 5.90, m = -5.37) (Figure 3.11B). In all samples from 0-10 cm depth, the mean lc excess value was lower (m = -10.27) than the lower end of the 95% confidence interval (m = -8.28), suggesting meaningful evaporative fractionation effects of soil water at this sampling depth (Figure 3.11B). Samples at this depth generally plotted to the right of the LMWL more frequently than deeper soil depths (Figure 3.12A). When comparing soil lc excess values the median value differed between the 0-10 and 20-30 cm (Wilcoxon rank sum test, p-value < 0.001) and the 10-20 and 20-30 cm depths (Wilcoxon rank sum test, p-value < 0.05), but lack confidence in differences in the median values between soil depths from 0-10 cm and 10-20 cm (Figure 3.11B). We observed more variability in lc excess values in the short stubble (s = 8.48) as compared to the tall stubble (s = 6.41) but the median of the distribution of values did not differ between the groups (Wilcoxon rank sum test, p-value > 0.05) (Figure 3.11D).

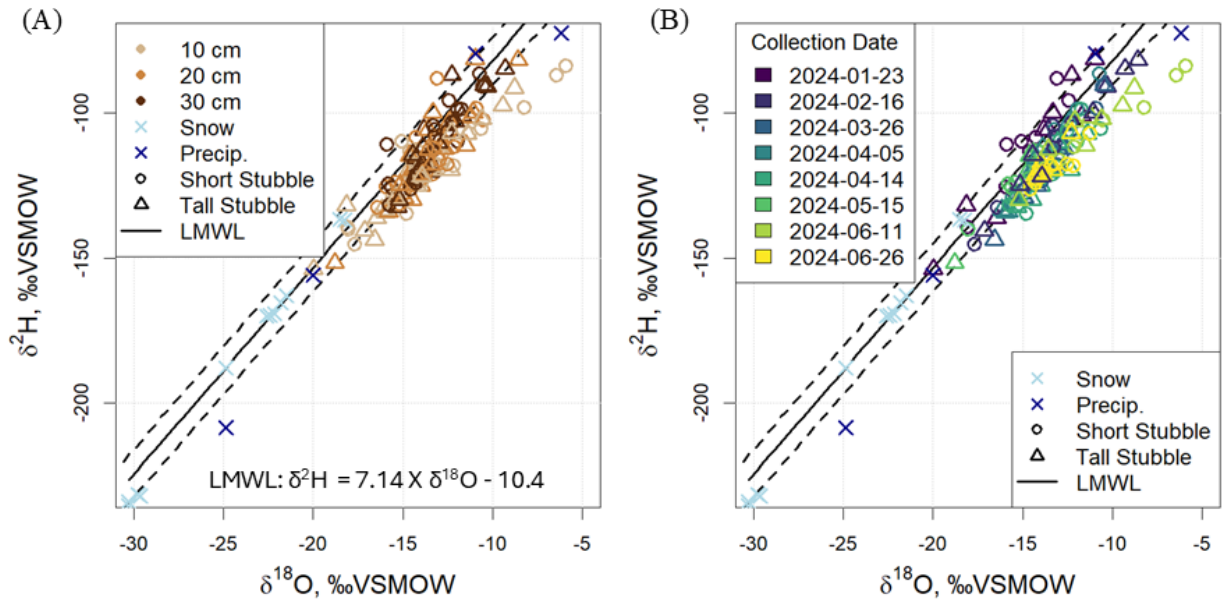


Figure 3.12: Dual-isotope plot of all water isotope samples collected during sampling period. (A) Soil water samples color coded by soil collection depth and (B) soil water samples color coded

by sample collection date relative to the local meteoric water line (solid black line) and 95% confidence interval (dashed black lines) (Mayernik et al., 2024). Open circles represent soil samples from short stubble and open triangles reflect samples from tall stubble.

On four of eight sampling dates, the mean lc excess value of all sampling depths was more negative than the lower limit of the established 95% confidence interval (m = -8.28) (Figure 3.12B, 3.13); specifically on 26 March (m = -10.23), 14 April (m = -12.72), 11 June (m = -15.89), and 26 June (m = -11.92) (Table 3.S2). This suggests meaningful evaporative effects on soil water at all depths on these specific dates (Figure 3.13) and generally plot to the right of the LMWL (Figure 3.12B).

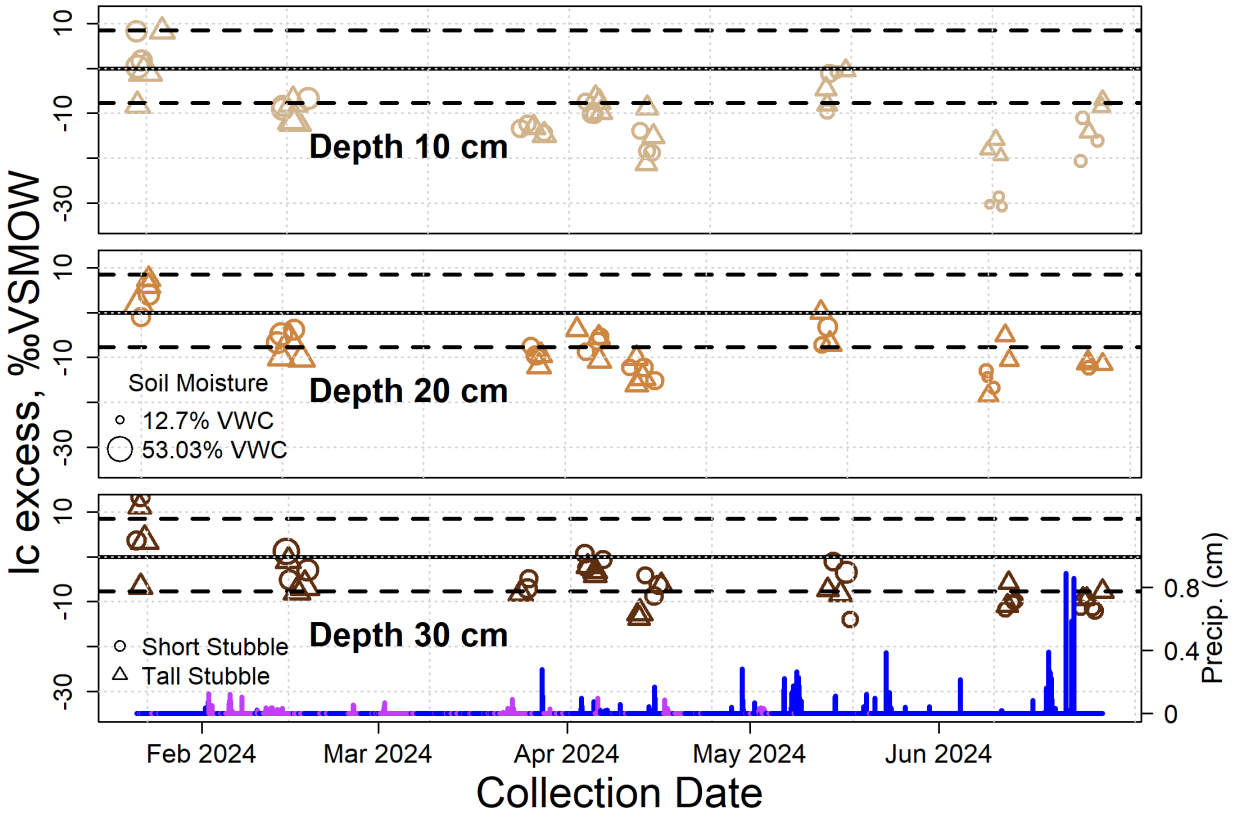


Figure 3.13: Seasonal trends of line excess (lc excess) values across all sampling days. (A) Values for soils sampled from 0-10 cm; (B) 10-20 cm; and (C) 20-30 cm. The solid black line indicates the local meteoric water line, with the dashed lines reflecting the 95% confidence interval (Mayernik et al., 2024). Open circles represent soil samples from short stubble and open

triangles reflect samples from tall stubble. The size of the symbol corresponds to the volumetric water content at that specific soil depth and location, with bigger symbols reflecting higher water content.

Soil water on 11 June exhibited the most negative average lc excess values, across all sampling depths, indicating influence from evaporation in addition to likely transpiration on this date (Figure 3.8, 3.13, Table 3.S2). Additionally, we observed the largest difference in mean lc excess values between the two stubble treatment types, short (m = -29.95) and tall (m= -17.89) (Figure 3.13A, Table 3.S2), at any depth (0-10 cm) on this same date. These data correspond with the lowest water content, at a soil collection interval of 0-10 cm, of any sampling date (Figure 3.9, Table 3.4), further suggesting effects due to evaporation and transpiration.

3.4 Discussion

3.4.1 Precipitation delivery dictated by crop stubble height

Precipitation events and snow retention were sporadic during the winter sampling of 2023-2024 at Moccasin (Figure 3.4A), with 4.26 cm of snow-derived water from December to March. In comparison, 19.54 cm of water was delivered as snow at Bozeman in the winter of 2022-2023 (Figure 3.3A). In Bozeman, snow depth and SWE values over the winter of 2023 showed increased snow capture in tall stubble as compared to short during mid-winter conditions on 17 February and 2 March 2023 (Figure 3.5A,B). The Bozeman LiDAR data further supports these manually observed differences, with similar snow depth and SWE values reported in both the short and tall stubble on both days (Figure 3.6). These similarities point to the power of the LiDAR derived data to assess snowpack dynamics, with a large number of observations in the short (n=173,801) and tall (n=167,749) stubble on 17 February and in the short (n=173,591) and

tall (n=167,659) stubble plots on 2 March, providing rigorous measures of variability across the study area (Figure 3.6, 3.S3). Differences between the manual and LiDAR values may be associated with limited manual data observations, resulting in values that do not capture spatial variability of snow and SWE values (Figure 3.S3).

However, due to deep perennial snowpack throughout the winter (Figure 3.3A), a large snow fall event at the end of March 2023 negated differences between these treatment types, likely fully filling the tall stubble and short stubble, as indicated by mean snow depths in both treatment types similar to the height of the cut tall stubble (45 cm) (Figure 3.5C). This observation points to limitations of small plot designs for snow entrapment study (Figure 3.1B), supporting further research at field scale, as was conducted the following winter in Moccasin (Figure 3.1C).

Reflecting the severely limited winter moisture delivery at Moccasin in 2023–2024, there was a 30-day period of zero precipitation from 11 December 2023 to 11 January 2024 (Figure 3.4A). This occurred alongside warmer-than-average air temperatures and precipitation with less negative δ^2H values during November and December 2023 (Figure 3.10A). These conditions, likely combined with 12.21 cm of warmer fall moisture (September – December 2023; Figure 3.4A), drove soil water δ^2H values to reflect warmer precipitation values at 10–20 cm and 20–30 cm soil depth intervals during the first two sampling events (Figure 3.10C,D). Contrastingly, on 23 January and 16 February 2024, the 0-10 cm soil water δ^2H values were more negative than at 10-20 cm or 20-30 cm. Specifically, on 23 January we observed the most negative average δ^2H values in soil water of any soil depth interval (0-10 cm) on any collection date (-130.64‰) (Figure 3.10A), indicating contribution from mixing of 0.76-2.3 cm of snow melt water in the

soil profile based on meteorological and manual measurements of snow inputs (Figure 3.4A, Figure 3.9). Assuming that the average δ^2H value (-101.4‰) and average height of water (3.72 cm) on 23 January at 20 cm reflects the soil water content and δ^2H value from 0-10 cm prior to any snow water inputs and using an average snow δ^2H value of (-233.2‰), a volume weighted mixing model suggests an addition of 1.06 cm of snow-derived water would be required to produce the observed value from 0-10 cm (-130.6‰). This estimated value falls within our estimated range of snow water inputs on 0.76-2.3 cm, providing supporting evidence that soil water from 0-10 cm on 23 of January is influenced by snow melt water.

Throughout the sampling campaign, δ^2H values at shallow depths (0-10 cm) became less negative (Figure 3.10B), reflecting contributions of warmer precipitation (Figure 3.10A). This suggests that – from 0-10 cm depth –soil water isotopic values rose readily in response to small, isotopically distinct precipitation inputs. Increased variation in δ^2H values at soil depths of 0-10 cm as compared to 20-30 cm, indicates the response of the isotopic composition of soil water to changing meteorological inputs at shallow depths (Figure 3.11A). In contrast, we observed decreasing isotopic values in soil water at 10-20 cm (Figure 3.10C) and at 20-30 cm (Figure 10D). This trend suggests delayed infiltration and mixing of input precipitation with residual soil water (Sprenger et al., 2016), resulting in a dampening effect of the precipitation signal with depth (Bertrand et al., 2014).

Although we did not observe a difference in Moccasin soil water δ^2H values between short and tall stubble in the cumulative data (Figure 3.11C), we did see differences on individual sampling dates in 2024. The greatest difference in δ^2H values between short and tall stubble occurred at 0-10 cm on 23 January (Figure 3.10B), likely due to an ephemeral snowpack

preferentially accumulating in taller stubble areas of the field (Figure 3.7). Snow was blown out of the short stubble and accumulated in the tall stubble, resulting in limited influence from snow melt in the soil water isotopic signature under short stubble (Figure 3.10B). We report increased soil water content in the short stubble on this date, which would contradict snowpack accumulating in tall stubble, but believe snow may have accumulated in the soil moisture sample but is not reflected in the isotopic samples due to the high spatial variability of soil water isotopes. Contrastingly, on 16 February as snow melted and infiltrated deeper into the soil profile, the isotopic composition of the soil water became more negative from 10-20 cm in the short stubble as compared to the tall stubble (Figure 3.10C). We would expect more negative values within the tall stubble due to an increased presence of snow on 23 January (Figure 3.7). However, due to limited precipitation inputs (m = 2.3 cm, Figure 3.4), based on meteorological data from the beginning of January to 16 February, the influence of the average isotopic composition of the snow melt water (δ^2H = -186.0‰), may be limited due to mixing with residual soil water on 23 of January within the top 20 cm (7.42 cm, δ^2H = -116.0‰; Table 3.4). This mixing would result in an average δ^2H of 132.6‰ from 0-20 cm on the 16 of February, similar to our observed average value of -119.8‰. On 26 March we observe more negative δ^2H values in the tall stubble, at 0-10 and 10-20 cm, as compared to the short stubble. This finding would suggest more influence from colder meteorological inputs in the tall stubble. However, this is contradicted as sampled snow on 16 February showed no meaningful differences in snow accumulation in the short or tall stubble (Figure 3.5D, Table 3.2), which we expect would result in a relatively uniform soil water isotopic composition due to snow water infiltration into the soil profile by the time we sampled on 26 March. This finding could indicate a missed snow event in

late March, which could have favored snow accumulation in the tall stubble, or more effective retention and infiltration of melt water in the tall stubble (Gaj et al., 2017; Millar et al., 2022; E. J. Oerter & Bowen, 2019; Sprenger et al., 2016).

We detected no differences in manually assessed soil water content, between short and tall stubble, during our winter sampling campaign in Moccasin (January-March 2024), additionally supported by the Sentek soil water content monitoring (Table 3.3, Figure 3.9)(Barnes et al., 2025, M.S. Thesis). We expect this due to limited wintertime precipitation (4.26 cm) with minimal snow accumulation favoring tall stubble on only one of two sampling dates (Table 2, Figure 3.5D, 3.7). Continuously recorded Sentek data lose resolution when averaged (Figure 3.4C), while manual measures likely improved accounting for small additions of water.

3.4.2 Soil water evaporative signal trends and stubble management microclimate influence on soil water isotopic composition and content

Seasonal trends in Moccasin soil water lc excess values point to chronic water loss to evaporation in spring and early summer (Figure 3.8). Throughout the sampling campaign, lc excess values became more negative, at all collection depths, but rebounded somewhat in the middle of May and at the end of June from 0-10 cm (Figure 3.13A), when increased precipitation reset the evaporative signal of the soil water. Additionally, the rebound in lc excess values at the end of June may reflect non-fractionating transpiration, beginning to outweigh evaporation (Hsieh et al., 1998). On four separate sampling dates (26 March, 14 April, 11 June, 26 June) the mean lc excess value across all sampling depths was more negative than the mean value for the lower end of the established confidence interval (Figure 3.11B,13) (Mayernik et al., 2024). This

indicates meaningful evaporative effects on soil water at all depths (Figure 3.11B). We did not observe substantial evaporative signals on 5 April, at 10-20 cm and 20-30 cm, and across all depths on 15 May potentially due to precipitation events occurring before the collection date, likely reducing the evaporative signal (Figure 3.4A, 3.13).

Multiple lines of evidence indicate variable influence from evaporation on soil water, dependent on soil sampling depth. On average, we saw the most substantial and consistent evaporative signal in the soil water collected at 0-10 cm during the sampling campaigns (Figure 3.11B, 3.13A). Influence of evaporation – likely in water evaporated near the surface before infiltrating to greater depths in the profile – persists in the 20-30 cm soil depth interval (Figure 3.13C), depending on the sampling date (Sprenger et al., 2016). As a whole, evaporative losses are likely small in magnitude, with total water heights diminished by ~2.5 cm between May-June sampling events likely reflecting both evaporation and transpiration.

Cumulative soil water isotopic lc excess values did not show a difference between short and tall stubble, but temporal pattens suggest hot moments of evaporative influence at the Moccasin field site in 2024. When assessing individual collection dates, we saw the largest difference in lc excess values on 11 June, at a depth of 10 cm, with more negative lc excess values in the short versus tall stubble (Figure 3.13A). Prior to this sampling event the study site experienced a period of seven days without precipitation (nothing >1mm of rain hr^{-1}) (Figure 3.4A), allowing for evaporative signals to be evident within soil water (Figure 3.13A) (Gaj et al., 2016). This evidence is supported by the fact that on 11 June we saw the largest difference in the total height of water on any sampling date between the short and tall stubble (1.2 cm) (Table 3.3, Figure 3.9). On this same date, the second and third largest differences in soil water occurred at

0–10 cm (0.44 cm) and 10–20 cm (0.55 cm), respectively, with higher water content in tall stubble, indicating greater evaporation in short stubble (Table 3.4, Figure 3.9). On 26 June we saw the second largest difference in lc excess values between the short and tall stubble at 10 cm, with more negative values within the short stubble (Figure 3.13A). Likely, we saw a decreased lc excess value difference between the short and tall stubble on this date, as compared to 11 June, due to increased precipitation inputs (5.94 cm) prior to this sampling event, mixing with limited soil water at 10cm (1.71 cm), resetting the evaporative signal in the soil profile (Figure 3.4A, 3.13A). Additionally, on 26 June, the mean lc excess value, across all sampling depths, is more negative in short stubble as compared to tall stubble, suggesting increased evaporation in the short stubble at all soil depths (Figure 3.13A, 3.S6). These observations suggest that 1.49 cm of evaporated soil water, based on the height of soil water in short stubble on 11 June from 0-10 cm (Figure 3.9, Table 3.4), percolated downward due to 5.94 cm of precipitation inputs between these sampling events, leading to detectable differences in lc excess values with depth (Figure 8, S3). Overall, lc excess values expressed evaporation more frequently during late spring to summer sampling events, with differences between short and tall stubble detected due to increased soil shading effects caused by the taller stubble, consistent with previously reported evaporation patterns exhibited in short and tall stubble studies (H. W. Cutforth & McConkey, 1997) and more generally in the context of vegetative shading effects on soil water isotopic composition (Dubbert et al., 2013; Zimmermann et al., 1967).

Averaged Sentek soil moisture measurements during the growing season (17 May - 29 July 2024) did not reveal substantial difference in soil moisture between the short and tall stubble (Figure 3.4C; Barnes et al., 2025, M.S. Thesis); however, depth resolved data from sensors at

discrete depths showed persistently greater moisture in tall stubble at 15 and 25 cm over the May-July period (Barnes et al., 2025, M.S. Thesis; Appendix B). Consistent with this, manual soil water content measurements on 11 June, indicate 1.2 cm increase in the height of soil water, across the sampled soil profile (0-30 cm), within the tall stubble as compared to the short stubble. In light of observed lc excess values (Figure 3.13), we suspect this difference is caused by increased evaporation of the soil water in the short stubble. The more persistent difference suggested by continuous sensing may signal ongoing effects of evaporation but is not consistent with manual sampling results. Additional observations are merited.

3.5 Conclusion

This work provides an isotopic perspective on how dryland agricultural management practices influence water storage in soils. Observed $\delta^{2}H$ and $\delta^{18}O$ values, coupled with soil water content, meteorological monitoring, and snow accumulation assessment, provide insight into how managed cereal grain stubble heights influence soil water character and content seasonally, and interact with a subsequent pulse crop. The results highlight the increased temporal sensitivity of soil water isotopic values to small additions and losses of water. At shallower soil sampling depths (0-10 cm) the isotopic composition of soil water is sensitive to small precipitation inputs, while at greater depths (20-30 cm), soil water from shallower depths mixes with residual soil water, which alters and homogenizes the isotopic composition. The data reiterate that evaporation influences soil water readily during warmer months and at shallow depths (0-10 cm) as compared to greater depths (10-20 cm, 20-30 cm), although we see evaporative signals in soil water at all sampling depths due to downward percolation and mixing. On 23 January 2024, the isotopic signature of soil water from 0-10 cm reflected greater influence from snow-derived

precipitation, indicated by more negative δ^2H values. This effect is more pronounced in tall stubble soils due to increased snowpack retention and effective capture of melt water compared to short stubble. On 11 June 2024 we observed isotopic signals indicating increased evaporation of soil water at 0-10 cm, in the short stubble as compared to the tall stubble, resulting in ~1.2 cm of water loss across the manually monitored soil profile (0-30 cm). Further, on 26 June 2024, despite a diminished evaporative signal at 0-10 cm, we observed greater in-mixing of evaporated waters throughout the short stubble soil profile. Overall, the results point to temporal differences in the retention and loss of soil water in short and tall stubble dryland agricultural fields, with timing and form of precipitation patterns driving the extent of both soil water storage and evaporative loss.

Acknowledgements

We are extremely thankful to the producers in Moccasin and Geraldine Montana, without their participation and support this work would not have been possible. The authors thank the USDA-ARS Agreement 58-3032-005, the Montana State University Nielson Pedology Graduate Research Fellowship (2024), and the Montana Wheat and Barley Committee, for funding of this research. Additionally, we are thankful for the support received from the Montana Agricultural Experiment Station (Project MONB00364) and the Montana State University Environmental Analytical Lab, and for data provided by the Montana Mesonet. Any opinions, findings, conclusions or recommendations expressed in this material are those of the authors and do not necessarily reflect the views of the U.S. Department of Agriculture. We thank Caitlin Mayernik and Adam Sigler for their foundational work in this area, providing the necessary groundwork to make this research possible. We thank Dr. Perry Miller for introducing the concept of stubble

management in these locations and providing beneficial agronomic information critical to the formation of this chapter. We thank fellow graduate student Ryan Barnes for help establishing field sites and contributing to data collection. We thank Dr. Eric A. Sproles and the entire GEOSWIRL lab for graciously lending their drone equipment and expertise for successful remote sensing of snowpack dynamics. Additionally, we thank Dr. Jane Klassen, Aneliya Cox, Emma Tate, Kieran Tharp, Niko Hinz, Cole Edwards, Wally Tonks, and Maggie Druckenmiller for help with data collection, analysis, and technical assistance.

CHAPTER FOUR

GENERAL CONCLUSION

This thesis links the terrestrial and riparian ecosystems of central Montana through the central theme of hydrologic controls on nitrate mobilization and attenuation. The presented collaborative research investigates the dryland agricultural practices of stubble height management, as a rotation practice used to maximize soil water storage, particularly ahead of a pulse crop. The common practice of summer fallow influences nitrate leaching dynamics by maximizing water storage that contributes to deep percolation of nitrate (Sigler et al., 2020). High nitrate concentrations in oxic groundwater ultimately compromise the water quality of hydrologically connected stream corridors. Within these stream corridors, nitrate reduction processes are fueled by anaerobic soils with organic carbon present, improving water quality.

Riparian areas play an integral role in buffering upland agricultural nitrate pollution. The first manuscript in this thesis (Chapter 2) explores riparian flow dynamics and nitrate attenuation patterns, combining geochemical data, geophysical observations, tracer observations, and simulations. We found that flow dynamics are intimately connected with nitrate concentrations in the Louse Creek stream corridor. Coarser, more transmissive substrate material, indicated by higher K_{sat} values and higher resistivity values (K-means cluster 3-4), resulted in higher and more variable riparian groundwater nitrate concentration values. Simulations of the tracer results that account for nitrate attenuation illustrate how coarse textures regulate flow and how the proportion of flow through fine textured material regulates nitrate consumption.

Within terrestrial ecosystems, the dryland agricultural practice of stubble height management has the potential to enhance soil water storage. The third chapter of this thesis

explores the interaction of cereal grain stubble height with precipitation patterns to regulate soil water retention, combining measures of soil water isotopic composition (δ^2H and $\delta^{18}O$ values), soil water content, meteorological monitoring, and snow accumulation assessment. Our results highlight the temporal sensitivity of soil water isotopic composition to added precipitation, rendering sample timing critically important to tracking differences in soil water isotopic composition between short and tall stubble. We observed increased effects of soil water evaporation, recorded as lower lc excess values in short stubble at shallow depths during dry periods of summer months. Additionally, we saw increased snow derived soil water (lower δ^2H values) at shallow depths in tall stubble following winter precipitation events that favored accumulation in tall stubble. Isotopic compositions then propagated downward through soils over time, reflecting transport and mixing effects. Overall, even with an extremely dry winter, these results point to temporal variation in the isotopic composition of soil water with stubble height, with timing and form of precipitation patterns driving these differences. Further research in this setting could elucidate differences in soil water isotopic composition between short and tall stubble by targeting sampling times when the largest differences are expected, as suggested by the findings of this study.

Management practices can reduce nitrate loading within hydrologically connected terrestrial and aquatic agroecosystems. Within stream corridors supplying organic carbon, nitrate consumption is likely driven by hydrologic interaction with fine-textured material, highlighting the importance of shallow groundwater interacting with these zones. Consequently, human-altered wetlands still fuel nitrate consumption when they slow flow through reactive material. Upstream of these wetlands, using stubble management to enhance soil water storage, followed

by a pulse crop that limits N additions and consumes stored water, may balance water and N use efficiencies, delivering less nitrate to riparian areas. Ultimately, creative cropping system solutions are required to temper environmental consequences of nutrient and water use in a changing climate (Whitlock et al., 2017).

CUMULATIVE REFERENCES CITED

Aase, J. K., & Schaefer, G. M. (1996). Economics of tillage practices and spring wheat and barley crop sequence in the Northern Great Plains. *Journal of Soil and Water Conservation*, *51*(2).

Aase, J. K., & Siddoway, F. H. (1980). Stubble height effects on seasonal microclimate, water balance, and plant development of no-till winter wheat. *Agricultural Meteorology*, *21*(1). https://doi.org/10.1016/0002-1571(80)90065-5

Amoozegar, A., & Warrick, A. W. (2018). Hydraulic conductivity of saturated soils: Field methods. In *Methods of Soil Analysis, Part 1: Physical and Mineralogical Methods*. https://doi.org/10.2136/sssabookser5.1.2ed.c29

Angier, J. T., McCarty, G. W., & Prestegaard, K. L. (2005). Hydrology of a first-order riparian zone and stream, mid-Atlantic coastal plain, Maryland. *Journal of Hydrology*, *309*(1–4). https://doi.org/10.1016/j.jhydrol.2004.11.017

Ann McCauley, & Clain Jones. (2005). Managing for Soil Erosion. *Soil and Water, Module 3, Montana State University Extension Service*, 1–12.

Barnes, C. J., & Allison, G. B. (1988). Tracing of water movement in the unsaturated zone using stable isotopes of hydrogen and oxygen. *Journal of Hydrology*, *100*(1–3). https://doi.org/10.1016/0022-1694(88)90184-9

Batson, J. A., Mander, Ü., & Mitsch, W. J. (2012). Denitrification and a Nitrogen Budget of Created Riparian Wetlands. *Journal of Environmental Quality*, *41*(6). https://doi.org/10.2134/jeq2011.0449

Bear, J. (1975). Dynamics of Fluids in Porous Media. *Soil Science*, *120*(2). https://doi.org/10.1097/00010694-197508000-00022

Bertrand, G., Masini, J., Goldscheider, N., Meeks, J., Lavastre, V., Celle-Jeanton, H., Gobat, J. M., & Hunkeler, D. (2014). Determination of spatiotemporal variability of tree water uptake using stable isotopes (δ18O, δ2H) in an alluvial system supplied by a high-altitude watershed, Pfyn forest, Switzerland. *Ecohydrology*, *7*(2). https://doi.org/10.1002/eco.1347

Binley, A., & Kemna, A. (2005). DC Resistivity and Induced Polarization Methods. In *Hydrogeophysics*. https://doi.org/10.1007/1-4020-3102-5_5

Black, A. L., & Siddoway, F. H. (1977). Winter Wheat Recropping on Dryland as Affected by Stubble Height and Nitrogen Fertilization. *Soil Science Society of America Journal*, *41*(6). https://doi.org/10.2136/sssaj1977.03615995004100060035x

Bouchard, D. C., Williams, M. K., & Surampalli, R. Y. (1992). Nitrate contamination of groundwater: sources and potential health effects. *Journal / American Water Works Association*, *84*(9). https://doi.org/10.1002/j.1551-8833.1992.tb07430.x

Burt, T. P., Matchett, L. S., Goulding, K. W. T., Webster, C. P., & Haycock, N. E. (1999). Denitrification in riparian buffer zones: The role of floodplain hydrology. *Hydrological Processes*, *13*(10). https://doi.org/10.1002/(SICI)1099-1085(199907)13:10<1451::AID-HYP822>3.0.CO;2-W

Campbell, C. A., McConkey, B. G., Zentner, R. P., Selles, F., & Dyck, F. B. (1992). Benefits of wheat stubble strips for conserving snow in southwestern Saskatchewan. *Journal of Soil & Water Conservation*, *47*(1).

Cardenas, M. B., & Markowski, M. S. (2011). Geoelectrical imaging of hyporheic exchange and mixing of river water and groundwater in a large regulated river. *Environmental Science and Technology*, *45*(4). https://doi.org/10.1021/es103438a

Cardillo, M. J., Bullock, P., Gulden, R., Glenn, A., & Cutforth, H. (2015). Stubble management effects on canola performance across different climatic regions of western Canada. *Canadian Journal of Plant Science*, *95*(1). https://doi.org/10.4141/cjps-2014-172

Carr, P. M., Boss, D. L., Chen, C., Dafoe, J. M., Eberly, J. O., Fordyce, S., Hydner, R. M., Fryer, H. K., Lachowiec, J. A., Lamb, P. F., McVay, K. A., Khan, Q. A., Miller, P. R., Miller, Z. J., & Torrion, J. A. (2020). Warm-season forage options in Northern Dryland Regions. *Agronomy Journal*, *112*(5). https://doi.org/10.1002/agj2.20261

Cedergren. (1977). Cedergren, H. R., Seepage, Drainage, & Flow Nets. 2nd. edition. New York-London-Sydney-Toronto, John Wiley & Sons 1977. XIII, 534 S., £ 23.15. *ZAMM - Journal of Applied Mathematics and Mechanics / Zeitschrift Für Angewandte Mathematik Und Mechanik*, *60*(1). https://doi.org/10.1002/zamm.19800600117

Chegini, G., & Mirnezami, S. V. (2016). Experimental comparison of combine performance with two harvesting methods: Stripper header and conventional header. *Agricultural Engineering International: CIGR Journal*, *18*(1).

Chen, C., Bekkerman, A., Afshar, R. K., & Neill, K. (2015). Intensification of dryland cropping systems for bio-feedstock production: Evaluation of agronomic and economic benefits of Camelina sativa. *Industrial Crops and Products*, *71*. https://doi.org/10.1016/j.indcrop.2015.02.065

Clark, I. D., & Fritz, P. (2013). Environmental Isotopes in Hydrogeology. In *Environmental Isotopes in Hydrogeology*. https://doi.org/10.1201/9781482242911

Clément, J., Pinay, G., & Marmonier, P. (2002). Seasonal Dynamics of Denitrification along Topohydrosequences in Three Different Riparian Wetlands. *Journal of Environmental Quality*, *31*(3). https://doi.org/10.2134/jeq2002.1025

C.M. Mayernik, S.A. Ewing, & R.A. Payn. (2024). Nitrate and sulfate isotopes indicate dynamic production and loss patterns in stream corridors draining agricultural landscapes. . *Biogeochemistry*.

Cochran, V., Danielson, J., Kolberg, R., & Miller, P. (2015). Dryland cropping in the Canadian prairies and the U.S. northern great plains. In *Dryland Agriculture* (Vol. 23). https://doi.org/10.2134/agronmonogr23.2ed.c9

Cooper, A. B. (1990). Nitrate depletion in the riparian zone and stream channel of a small headwater catchment. *Hydrobiologia*, *202*(1–2). https://doi.org/10.1007/BF02208124

Coscia, I., Greenhalgh, S. A., Linde, N., Doetsch, J., Marescot, L., GuNther, T., Vogt, T., & Green, A. G. (2011). 3D crosshole ERT for aquifer characterization and monitoring of infiltrating river water. *Geophysics*, *76*(2). https://doi.org/10.1190/1.3553003

Craig, H. (1961). Isotopic variations in meteoric waters. *Science*, *133*(3465). https://doi.org/10.1126/science.133.3465.1702

Craig, H., Gordon, L. I., & Horibe, Y. (1963). Isotopic exchange effects in the evaporation of water: 1. Low-temperature experimental results. *Journal of Geophysical Research*, *68*(17). https://doi.org/10.1029/jz068i017p05079

Criss, R. E. (1999). Principles of Stable Isotope Distribution. In *Principles of Stable Isotope Distribution*. https://doi.org/10.1093/oso/9780195117752.001.0001

Crook, N., Binley, A., Knight, R., Robinson, D. A., Zarnetske, J., & Haggerty, R. (2008). Electrical resistivity imaging of the architecture of substream sediments. *Water Resources Research*, *46*(4). https://doi.org/10.1029/2008WR006968

Custer, S. (1976). NITRATE IN GROUND WATER. A SEARCH FOR SOURCES NEAR RAPELJE, MONTANA. *NORTHWEST GEOL*, *5*, 25–33.

Cutforth, H., McConkey, B., Angadi, S., & Judiesch, D. (2011). Extra-tall stubble can increase crop yield in the semiarid canadian prairie. *Canadian Journal of Plant Science*, *91*(4). https://doi.org/10.4141/cjps10168

Cutforth, H. W., Angadi, S. V., & McConkey, B. G. (2006). Stubble management and microclimate, yield and water use efficiency of canola grown in the semiarid Canadian prairie. *Canadian Journal of Plant Science*, *86*(1). https://doi.org/10.4141/P05-073

Cutforth, H. W., & McConkey, B. G. (1997). Stubble height effects on microclimate, yield and water use efficiency of spring wheat grown in a semiarid climate on the Canadian prairies. *Canadian Journal of Plant Science*, *77*(3). https://doi.org/10.4141/P96-153

Cutforth, H. W., McConkey, B. G., Woodvine, R. J., Smith, D. G., Jefferson, P. G., & Akinremi, O. O. (1999). Climate change in the semiarid prairie of southwestern Saskatchewan: Late winter-early spring. *Canadian Journal of Plant Science*, *79*(3). https://doi.org/10.4141/P98-137

Dansgaard, W. (1964). Stable isotopes in precipitation. *Tellus A: Dynamic Meteorology and Oceanography*, *16*(4). https://doi.org/10.3402/tellusa.v16i4.8993

Day-Lewis, F. D., Singha, K., & Binley, A. M. (2005). Applying petrophysical models to radar travel time and electrical resistivity tomograms: Resolution-dependent limitations. *Journal of Geophysical Research: Solid Earth*, *110*(8). https://doi.org/10.1029/2004JB003569

Devito, K. J., Fitzgerald, D., Hill, A. R., & Aravena, R. (2000). Nitrate Dynamics in Relation to Lithology and Hydrologic Flow Path in a River Riparian Zone. *Journal of Environmental Quality*, *29*(4). https://doi.org/10.2134/jeq2000.00472425002900040007x

Doughty, M., Sawyer, A. H., Wohl, E., & Singha, K. (2020). Mapping increases in hyporheic exchange from channel-spanning logjams. *Journal of Hydrology*, *587*. https://doi.org/10.1016/j.jhydrol.2020.124931

Dubbert, M., Cuntz, M., Piayda, A., Maguás, C., & Werner, C. (2013). Partitioning evapotranspiration - Testing the Craig and Gordon model with field measurements of oxygen isotope ratios of evaporative fluxes. *Journal of Hydrology*, *496*. https://doi.org/10.1016/j.jhydrol.2013.05.033

Engel, R. E., Miller, P. R., McConkey, B. G., & Wallander, R. (2017). Soil Organic Carbon Changes to Increasing Cropping Intensity and No-Till in a Semiarid Climate. *Soil Science Society of America Journal*, *81*(2). https://doi.org/10.2136/sssaj2016.06.0194

Evans, A. E., Mateo-Sagasta, J., Qadir, M., Boelee, E., & Ippolito, A. (2019). Agricultural water pollution: key knowledge gaps and research needs. In *Current Opinion in Environmental Sustainability* (Vol. 36). https://doi.org/10.1016/j.cosust.2018.10.003

Fisher, J., & Acreman, M. C. (2004). Wetland nutrient removal: A review of the evidence. In *Hydrology and Earth System Sciences* (Vol. 8, Issue 4). https://doi.org/10.5194/hess-8-673-2004

Flerchinger, G. N., Sauer, T. J., & Aiken, R. A. (2003). Effects of crop residue cover and architecture on heat and water transfer at the soil surface. *Geoderma*, *116*(1–2). https://doi.org/10.1016/S0016-7061(03)00102-2

G. Blanchy, S. Saneiyan, J. Boyd, P. McLachlan, & A. Binley. (2020). *"ResIPy, an Intuitive Open Source Software for Complex Geological Inversion/Modeling"* (3.5.4). Computers and Geosciences. https://doi.org/10.1016/j.cageo.2020.104423

Gaj, M., Beyer, M., Koeniger, P., Wanke, H., Hamutoko, J., & Himmelsbach, T. (2016). In-situ unsaturated zone stable water isotope (2H and 18O) measurements in semi-arid environments using tunable off-axis integrated cavity output spectroscopy. In *Hydrology and Earth System Sciences* (pp. 6115–6149). Copernicus Publications on behalf of the European Geosciences Union. https://doi.org/10.5194/hessd-12-6115-2015

Gaj, M., Kaufhold, S., Koeniger, P., Beyer, M., Weiler, M., & Himmelsbach, T. (2017). Mineral mediated isotope fractionation of soil water. *Rapid Communications in Mass Spectrometry*, *31*(3). https://doi.org/10.1002/rcm.7787

Groffman, P. M., Butterbach-Bahl, K., Fulweiler, R. W., Gold, A. J., Morse, J. L., Stander, E. K., Tague, C., Tonitto, C., & Vidon, P. (2009). Challenges to incorporating spatially and temporally explicit phenomena (hotspots and hot moments) in denitrification models. *Biogeochemistry*, *93*(1–2). https://doi.org/10.1007/s10533-008-9277-5

Gröning, M. (2011). Improved water δ2H and δ18O calibration and calculation of measurement uncertainty using a simple software tool. *Rapid Communications in Mass Spectrometry*, *25*(19). https://doi.org/10.1002/rcm.5074

Halvorson, A. D., Anderson, R. L., Toman, N. E., & Welsh, J. R. (1994). Economic comparison of three winter wheat-fallow tillage systems. *Journal of Production Agriculture*, *7*(3). https://doi.org/10.2134/jpa1994.0381

Hansen, N. C., Allen, B. L., Anapalli, S., Blackshaw, R. E., Lyon, D. J., & Machado, S. (2017). Dryland agriculture in north america. In *Innovations in Dryland Agriculture*. https://doi.org/10.1007/978-3-319-47928-6_15

Hanson, G. C., Groffman, P. M., & Gold, A. J. (1994). Denitrification in Riparian Wetlands Receiving High and Low Groundwater Nitrate Inputs. *Journal of Environmental Quality*, *23*(5). https://doi.org/10.2134/jeq1994.00472425002300050011x

Harder, P., Pomeroy, J. W., Helgason, W. D., & Helgason, W. D. (2020). Improving sub-canopy snow depth mapping with unmanned aerial vehicles: Lidar versus structure-from-motion techniques. *Cryosphere*, *14*(6). https://doi.org/10.5194/tc-14-1919-2020

Hatfield, J. L., & Sauer, T. J. (2015). Soil Management: Building a Stable Base for Agriculture. In *Soil Management: Building a Stable Base for Agriculture*. https://doi.org/10.2136/2011.soilmanagement

Haycock, N. E., & Pinay, G. (1993). Groundwater Nitrate Dynamics in Grass and Poplar Vegetated Riparian Buffer Strips during the Winter. *Journal of Environmental Quality*, *22*(2). https://doi.org/10.2134/jeq1993.00472425002200020007x

Heisler, J., Glibert, P. M., Burkholder, J. M., Anderson, D. M., Cochlan, W., Dennison, W. C., Dortch, Q., Gobler, C. J., Heil, C. A., Humphries, E., Lewitus, A., Magnien, R., Marshall, H. G., Sellner, K., Stockwell, D. A., Stoecker, D. K., & Suddleson, M. (2008).

Eutrophication and harmful algal blooms: A scientific consensus. *Harmful Algae*, *8*(1). https://doi.org/10.1016/j.hal.2008.08.006

Hester, E. T., & Fox, G. A. (2020). Preferential Flow in Riparian Groundwater: Gateways for Watershed Solute Transport and Implications for Water Quality Management. In *Water Resources Research* (Vol. 56, Issue 12). https://doi.org/10.1029/2020WR028186

Hill, A. R. (1996). Nitrate Removal in Stream Riparian Zones. *Journal of Environmental Quality*, *25*(4). https://doi.org/10.2134/jeq1996.00472425002500040014x

Hill, A. R. (2019). Groundwater nitrate removal in riparian buffer zones: a review of research progress in the past 20 years. *Biogeochemistry*, *143*(3). https://doi.org/10.1007/s10533-019-00566-5

Hill, A. R., Devito, K. J., Campagnolo, S., & Sanmugadas, K. (2000). Subsurface denitrification in a forest riparian zone: Interactions between hydrology and supplies of nitrate and organic carbon. *Biogeochemistry*, *51*(2). https://doi.org/10.1023/A:1006476514038

Hoefer, R. H., Wicks, G. A., & Burnside, O. C. (1981). Grain Yields, Soil Water Storage, and Weed Growth in a Winter Wheat-Corn-Fallow Rotation 1 . *Agronomy Journal*, *73*(6). https://doi.org/10.2134/agronj1981.00021962007300060038x

Houlton, B. Z., Boyer, E., Finzi, A., Galloway, J., Leach, A., Liptzin, D., Melillo, J., Rosenstock, T. S., Sobota, D., & Townsend, A. R. (2013). Intentional versus unintentional nitrogen use in the United States: Trends, efficiency and implications. *Biogeochemistry*, *114*(1–3). https://doi.org/10.1007/s10533-012-9801-5

Hsieh, J. C. C., Chadwick, O. A., Kelly, E. F., & Savin, S. M. (1998). Oxygen isotopic composition of soil water: Quantifying evaporation and transpiration. *Geoderma*, *82*(1–3). https://doi.org/10.1016/S0016-7061(97)00105-5

Hvorslev, M. J. (1951). Time Lag and Soil Permeability in Ground-Water Observations. *Bulletin n. 36*, *36*.

İnce, A., Say, S. M., Kara, O., & Bilgili, E. (2011). Comparing of Different Harvesting Systems in Wheat Harvesting. In *Journal of Agricultural Machinery Science* (Vol. 7, Issue 1).

Ingraham, N. L., & Shadel, C. (1992). A comparison of the toluene distillation and vacuum/heat methods for extracting soil water for stable isotopic analysis. *Journal of Hydrology*, *140*(1–4). https://doi.org/10.1016/0022-1694(92)90249-U

John, A. A., Jones, C. A., Ewing, S. A., Sigler, W. A., Bekkerman, A., & Miller, P. R. (2017). Fallow replacement and alternative nitrogen management for reducing nitrate leaching in a semiarid region. *Nutrient Cycling in Agroecosystems*, *108*(3). https://doi.org/10.1007/s10705-017-9855-9

Klinner, W. E., Neale, M. A., Arnold, R. E., Geikie, A. A., & Hobson, R. N. (1987). A new concept in combine harvester headers. *Journal of Agricultural Engineering Research*, *38*(1). https://doi.org/10.1016/0021-8634(87)90137-5

L.A. Haag, R.K. Taylor, K.C. Dhuyvetter, & M.D. Schrock. (2004). Using yield monitor data to compare harvesting methods. *International ASAE Meeting*, *04*(1094).

Landwehr, J. M., & Coplen, T. B. (2006). Line-conditioned excess: a new method for characterizing stable hydrogen and oxygen isotope ratios in hydrologic systems. *International Conference on Isotopes in Environmental Studies*, *May*.

Lanning, S. P., Kephart, K., Carlson, G. R., Eckhoff, J. E., Stougaard, R. N., Wichman, D. M., Martin, J. M., & Talbert, L. E. (2010). Climatic change and agronomic performance of hard red spring wheat from 1950 to 2007. *Crop Science*, *50*(3). https://doi.org/10.2135/cropsci2009.06.0314

Larney, F. J., Bullock, M. S., McGinn, S. M., & Fryrear, D. W. (1995). Quantifying wind erosion on summer fallow in southern Alberta. *Journal of Soil and Water Conservation*, *50*(1).

Lawrence, P. G., Maxwell, B. D., Rew, L. J., Ellis, C., & Bekkerman, A. (2018). Vulnerability of dryland agricultural regimes to economic and climatic change. *Ecology and Society*, *23*(1). https://doi.org/10.5751/ES-09983-230134

Lenssen, A. W., Johnson, G. D., & Carlson, G. R. (2007). Cropping sequence and tillage system influences annual crop production and water use in semiarid Montana, USA. *Field Crops Research*, *100*(1). https://doi.org/10.1016/j.fcr.2006.05.004

Leuthold, S. J., Ewing, S. A., Payn, R. A., Miller, F. R., & Custer, S. G. (2021). Seasonal connections between meteoric water and streamflow generation along a mountain headwater stream. *Hydrological Processes*, *35*(2). https://doi.org/10.1002/hyp.14029

Liebig, M. A., Tanaka, D. L., & Wienhold, B. J. (2004). Tillage and cropping effects on soil quality indicators in the northern Great Plains. *Soil and Tillage Research*, *78*(2). https://doi.org/10.1016/j.still.2004.02.002

Lyon, D. J., & Peterson, G. A. (2005). Continuous dryland cropping in the Great Plains: What are the limits? *Agronomy Journal*, *97*(2). https://doi.org/10.2134/agronj2005.0347

Lyon, D. J., Stroup, W. W., & Brown, R. E. (1998). Crop production and soil water storage in long-term winter wheat-fallow tillage experiments. *Soil and Tillage Research*, *49*(1–2). https://doi.org/10.1016/S0167-1987(98)00151-2

Martin, J., Looker, N., Hoylman, Z., Jencso, K., & Hu, J. (2018). Differential use of winter precipitation by upper and lower elevation Douglas fir in the Northern Rockies. *Global Change Biology*, *24*(12). https://doi.org/10.1111/gcb.14435

Marzadri, A., Tonina, D., & Bellin, A. (2012). Morphodynamic controls on redox conditions and on nitrogen dynamics within the hyporheic zone: Application to gravel bed rivers with alternate-bar morphology. *Journal of Geophysical Research: Biogeosciences*, *117*(3). https://doi.org/10.1029/2012JG001966

Mayernik, C. M., Ewing, S. A., Degrandpre, M. D., Koffman, T. N. B., Foster, M. J., Dixon, J. L., Jones, C. A., Reinhold, A. M., & Payn, R. A. (2025). *Riparian Processes in Semi-Arid Landscapes: Balancing Nitrate Mitigation and Sulfate Augmentation in Agricultural System*.

Mayernik, C. M., Ewing, S. A., Sigler, W. A., Jencso, K. G., & Payn, R. A. (2024). Water isotopic composition traces source and dynamics of water supply in a semi-arid agricultural landscape. *Hydrological Processes*, *38*(2). https://doi.org/10.1002/hyp.15069

McDonnell, J. J., Stewart, M. K., & Owens, I. F. (1991). Effect of Catchment-Scale Subsurface Mixing on Stream Isotopic Response. *Water Resources Research*, *27*(12). https://doi.org/10.1029/91WR02025

McMaster, G. S., Aiken, R. M., & Nielsen, D. C. (2000). Optimizing wheat harvest cutting height for harvest efficiency and soil and water conservation. *Agronomy Journal*, *92*(6). https://doi.org/10.2134/agronj2000.9261104x

Melillo, J. M. (2021). Disruption of the global nitrogen cycle: A grand challenge for the twenty-first century. *Ambio*, *50*(4). https://doi.org/10.1007/s13280-020-01429-2

Millar, C., Janzen, K., Nehemy, M. F., Koehler, G., Hervé-Fernández, P., Wang, H., Orlowski, N., Barbeta, A., & McDonnell, J. J. (2022). On the urgent need for standardization in isotope-based ecohydrological investigations. *Hydrological Processes*, *36*(10). https://doi.org/10.1002/hyp.14698

Miller, C., Ewing, S., Brookshire, J., Sigler, A., Jones, C., Jackson-Smith, D., & Weissmann, G. (2013). *Groundwater nitrate transport and residence time in a vulnerable aquifer under dryland cereal production, M.S. Thesis*. Montana State University.

Miller, P. R., McConkey, B. G., Clayton, G. W., Brandt, S. A., Staricka, J. A., Johnston, A. M., Lafond, G. P., Schatz, B. G., Baltensperger, D. D., & Neill, K. E. (2002). Pulse crop adaptation in the northern Great Plains. *Agronomy Journal*, *94*(2). https://doi.org/10.2134/agronj2002.0261

Miller, R. B., Heeren, D. M., Fox, G. A., Halihan, T., Storm, D. E., & Mittelstet, A. R. (2014). The hydraulic conductivity structure of gravel-dominated vadose zones within alluvial floodplains. *Journal of Hydrology*, *513*. https://doi.org/10.1016/j.jhydrol.2014.03.046

Montana Climate Office. (2025, January 26). *Montana Climate Office. (2025). Mesonet Dashboard. Retrieved from: https://mesonet.climate.umt.edu/dash/*.

Muller, K., Vanderborght, J., Englert, A., Kemna, A., Huisman, J. A., Rings, J., & Vereecken, H. (2010). Imaging and characterization of solute transport during two tracer tests in a shallow aquifer using electrical resistivity tomography and multilevel groundwater samplers. *Water Resources Research*, *46*(3). https://doi.org/10.1029/2008WR007595

Naiman, R. J., & Décamps, H. (1997). The ecology of interfaces: Riparian zones. In *Annual Review of Ecology and Systematics* (Vol. 28). https://doi.org/10.1146/annurev.ecolsys.28.1.621

Nielsen, D. C., Unger, P. W., & Miller, P. R. (2005). Efficient water use in dryland cropping systems in the Great Plains. *Agronomy Journal*, *97*(2). https://doi.org/10.2134/agronj2005.0364

NRCS. (n.d.). *Snow Sampling Equipment*. Https://Www.Nrcs.Usda.Gov/Wps/Portal/Wcc/Home/AboutUs/MonitoringPrograms/SnowSamplingEquipment.

Ocampo, C. J., Oldham, C. E., & Sivapalan, M. (2006). Nitrate attenuation in agricultural catchments: Shifting balances between transport and reaction. *Water Resources Research*, *42*(1). https://doi.org/10.1029/2004WR003773

Oerter, E., Finstad, K., Schaefer, J., Goldsmith, G. R., Dawson, T., & Amundson, R. (2014). Oxygen isotope fractionation effects in soil water via interaction with cations (Mg, Ca, K, Na) adsorbed to phyllosilicate clay minerals. *Journal of Hydrology*, *515*. https://doi.org/10.1016/j.jhydrol.2014.04.029

Oerter, E. J., & Bowen, G. J. (2019). Spatio-temporal heterogeneity in soil water stable isotopic composition and its ecohydrologic implications in semiarid ecosystems. *Hydrological Processes*, *33*(12). https://doi.org/10.1002/hyp.13434

Orlowski, N., Breuer, L., & Mcdonnell, J. J. (2016). Critical issues with cryogenic extraction of soil water for stable isotope analysis. *Ecohydrology*, *9*(1). https://doi.org/10.1002/eco.1722

Padbury, G., Waltman, S., Caprio, J., Coen, G., McGinn, S., Mortensen, D., Nielsen, G., & Sinclair, R. (2002). Agroecosystems and Land Resources of the Northern Great Plains. *Agronomy Journal*, *94*(2). https://doi.org/10.2134/agronj2002.2510

Palomaki, R. T., & Sproles, E. A. (2023). Assessment of L-band InSAR snow estimation techniques over a shallow, heterogeneous prairie snowpack. *Remote Sensing of Environment*, *296*. https://doi.org/10.1016/j.rse.2023.113744

Peterson, G. A., & Westfall, D. G. (2004). Managing precipitation use in sustainable dryland agroecosystems. In *Annals of Applied Biology* (Vol. 144, Issue 2). https://doi.org/10.1111/j.1744-7348.2004.tb00326.x

Poole, J. W., & Ewing, S. A. (2025a). *Data supporting Jack Poole Chapter three of Masters thesis - Stubble management and associated soil moisture delivery in cultivated soils of dryland cereal production systems in central and southwest Montana, USA*. HydroShare, Http://Www.Hydroshare.Org/Resource/91166359814f4b639c585723b8e5d965.

Poole, J. W., & Ewing, S. A. (2025b). *Data supporting the manuscript - Understanding nitrate processing in agricultural stream corridors using electrical resistivity tomography and a salt tracer experiment in an unconfined riparian aquifer*. HydroShare, Http://Www.Hydroshare.Org/Resource/543c4c6793c5419fb472810e4a557558.

PRISM Climate Group. (2023, December 12). *PRISM Climate Group*. Oregon State University. https://prism.oregonstate.edu

Ranalli, A. J., & Macalady, D. L. (2010). The importance of the riparian zone and in-stream processes in nitrate attenuation in undisturbed and agricultural watersheds - A review of the scientific literature. In *Journal of Hydrology* (Vol. 389, Issues 3–4). https://doi.org/10.1016/j.jhydrol.2010.05.045

Rasmussen, P. E., & Parton, W. J. (1994). Long-Term Effects of Residue Management in Wheat-Fallow: I. Inputs, Yield, and Soil Organic Matter. *Soil Science Society of America Journal*, *58*(2). https://doi.org/10.2136/sssaj1994.03615995005800020039x

Rein, A., Hoffmann, R., & Dietrich, P. (2004). Influence of natural time-dependent variations of electrical conductivity on DC resistivity measurements. *Journal of Hydrology*, *285*(1–4). https://doi.org/10.1016/j.jhydrol.2003.08.015

Reinhold, A. M., Ewing, S. A., Payn, R. A., Poole, G. C., & Valett, H. M. (2025). *Simulating Streams as Biogeochemical Reactors*.

Ries, R. E., & Power, J. F. (1981). Increased Soil Water Storage and Herbage Production from Snow Catch in North Dakota. *Journal of Range Management*, *34*(6). https://doi.org/10.2307/3898104

Rivett, M. O., Buss, S. R., Morgan, P., Smith, J. W. N., & Bemment, C. D. (2008). Nitrate attenuation in groundwater: A review of biogeochemical controlling processes. In *Water Research* (Vol. 42, Issue 16). https://doi.org/10.1016/j.watres.2008.07.020

Roberts, T. L. (2009). The role of fertilizer in growing the world's food. *Better Crops*, *93*(2).

Robinson, D. A., Binley, A., Crook, N., Day-Lewis, F. D., Ferré, T. P. A., Grauch, V. J. S., Knight, R., Knoll, M., Lakshmi, V., Miller, R., Nyquist, J., Pellerin, L., Singha, K., & Slater, L. (2008). Advancing process-based watershed hydrological research using near-surface geophysics: A vision for, and review of, electrical and magnetic geophysical methods. In *Hydrological Processes* (Vol. 22, Issue 18). https://doi.org/10.1002/hyp.6963

Roley, S. S., Tank, J. L., & Williams, M. A. (2012). Hydrologic connectivity increases denitrification in the hyporheic zone and restored floodplains of an agricultural stream. *Journal of Geophysical Research: Biogeosciences*, *117*(3). https://doi.org/10.1029/2012JG001950

Rosegrant, M., Cai, X., Cline, S., & Nakagawa, N. (2002). The Role of Rainfed Agriculture in the Future of Global Food Production. *Environment and Production Technology Division*, *90*.

Rosenberry, D. O., Briggs, M. A., Delin, G., & Hare, D. K. (2016). Combined use of thermal methods and seepage meters to efficiently locate, quantify, and monitor focused groundwater discharge to a sand-bed stream. *Water Resources Research*, *52*(6). https://doi.org/10.1002/2016WR018808

Ryan G. Barnes, Perry R. Miller, Stephanie A. Ewing, Patrick M. Carr, & Paul Nugent. (2025). *Impacts of very tall stubble on pulse crop morphology and productivity in the Northern Great Plains, M.S.Thesis*.

Sanchez-Vila, X., Guadagnini, A., & Carrera, J. (2006). Representative hydraulic conductivities in saturated groundwater flow. *Reviews of Geophysics*, *44*(3). https://doi.org/10.1029/2005RG000169

Schaetzl, R. J., & Thomson, M. I. (2015). Soils: Genesis and Geomorphology: Second Edition. In *Cambridge University Press*.

Schillinger, W. F., Papendick, R. I., Guy, S. O., Rasmussen, P. E., & Van Kessel, C. (2015). Dryland cropping in the western United States. In *Dryland Agriculture* (Vol. 23). https://doi.org/10.2134/agronmonogr23.2ed.c11

Schillinger, W. F., & Wuest, S. B. (2021). Wheat stubble height effects on soil water capture and retention during long fallow. *Agricultural Water Management*, *256*. https://doi.org/10.1016/j.agwat.2021.107117

Schlegel, A., Haag, L., Assefa, Y., & Holman, J. (2023). Wheat stubble height effects on subsequent corn and grain sorghum crops. *Crop Science*, *63*(3). https://doi.org/10.1002/csc2.20890

Shabaga, J. A., & Hill, A. R. (2010). Groundwater-fed surface flow path hydrodynamics and nitrate removal in three riparian zones in southern Ontario, Canada. *Journal of Hydrology*, *388*(1–2). https://doi.org/10.1016/j.jhydrol.2010.04.028

Sharp, Z. (2017). Principles of Stable Isotope Geochemistry, 2nd edition. *Principles of Stable Isotope Geochemistry, 2nd Edition*, *136*(1).

Siebert, S., Döll, P., Hoogeveen, J., Faures, J. M., Frenken, K., & Feick, S. (2005). Development and validation of the global map of irrigation areas. *Hydrology and Earth System Sciences*, *9*(5). https://doi.org/10.5194/hess-9-535-2005

Sigler, W. A., Ewing, S. A., Jones, C. A., Payn, R. A., Brookshire, E. N. J., Klassen, J. K., Jackson-Smith, D., & Weissmann, G. S. (2018). Connections among soil, ground, and surface water chemistries characterize nitrogen loss from an agricultural landscape in the

upper Missouri River Basin. *Journal of Hydrology*, *556*. https://doi.org/10.1016/j.jhydrol.2017.10.018

Sigler, W. A., Ewing, S. A., Jones, C. A., Payn, R. A., Miller, P., & Maneta, M. (2020). Water and nitrate loss from dryland agricultural soils is controlled by management, soils, and weather. *Agriculture, Ecosystems and Environment*, *304*. https://doi.org/10.1016/j.agee.2020.107158

Sigler, W. A., Ewing, S. A., Wankel, S. D., Jones, C. A., Leuthold, S., Brookshire, E. N. J., & Payn, R. A. (2022). Isotopic signals in an agricultural watershed suggest denitrification is locally intensive in riparian areas but extensive in upland soils. *Biogeochemistry*, *158*(2). https://doi.org/10.1007/s10533-022-00898-9

Singha, K., Pidlisecky, A., Day-Lewis, F. D., & Gooseff, M. N. (2008). Electrical characterization of non-Fickian transport in groundwater and hyporheic systems. *Water Resources Research*, *46*(4). https://doi.org/10.1029/2008WR007048

Slater, L. (2007). Near surface electrical characterization of hydraulic conductivity: From petrophysical properties to aquifer geometries - A review. *Surveys in Geophysics*, *28*(2–3). https://doi.org/10.1007/s10712-007-9022-y

Slater, L. D., Ntarlagiannis, D., Day-Lewis, F. D., Mwakanyamale, K., Versteeg, R. J., Ward, A., Strickland, C., Johnson, C. D., & Lane, J. W. (2010). Use of electrical imaging and distributed temperature sensing methods to characterize surface water-groundwater exchange regulating uranium transport at the Hanford 300 Area, Washington. *Water Resources Research*, *46*(10). https://doi.org/10.1029/2010WR009110

Smith, V. H., Tilman, G. D., & Nekola, J. C. (1999). Eutrophication: Impacts of excess nutrient inputs on freshwater, marine, and terrestrial ecosystems. *Environmental Pollution*, *100*(1–3). https://doi.org/10.1016/S0269-7491(99)00091-3

Sprenger, M., Leistert, H., Gimbel, K., & Weiler, M. (2016). Illuminating hydrological processes at the soil-vegetation-atmosphere interface with water stable isotopes. In *Reviews of Geophysics* (Vol. 54, Issue 3). https://doi.org/10.1002/2015RG000515

Sprenger, M., Tetzlaff, D., & Soulsby, C. (2017). Soil water stable isotopes reveal evaporation dynamics at the soil-plant-atmosphere interface of the critical zone. *Hydrology and Earth System Sciences*, *21*(7). https://doi.org/10.5194/hess-21-3839-2017

Stewart, B. A., & Koohafkan, P. (2015). Dryland agriculture: Long neglected but of worldwide importance. In *Challenges and Strategies of Dryland Agriculture*. https://doi.org/10.2135/cssaspecpub32.c2

Stewart, B. A., Koohafkan, P., & Ramamoorthy, K. (2015). Dryland agriculture defined and its importance to the world. In *Dryland Agriculture* (Vol. 23). https://doi.org/10.2134/agronmonogr23.2ed.c1

Stöckle, C. O., Higgins, S., Nelson, R., Abatzoglou, J., Huggins, D., Pan, W., Karimi, T., Antle, J., Eigenbrode, S. D., & Brooks, E. (2018). Evaluating opportunities for an increased role of winter crops as adaptation to climate change in dryland cropping systems of the U.S. Inland Pacific Northwest. *Climatic Change*, *146*(1–2). https://doi.org/10.1007/s10584-017-1950-z

Tanaka, D. L., Lyon, D. J., Miller, P. R., Merrill, S. D., & McConkey, B. G. (2010). Soil and water conservation advances in the semiarid northern great plains. In *Soil and Water*

Conservation Advances in the United States (Vol. 60). https://doi.org/10.2136/sssaspecpub60.c3

Tesoriero, A. J., Duff, J. H., Saad, D. A., Spahr, N. E., & Wolock, D. M. (2013). Vulnerability of streams to legacy nitrate sources. *Environmental Science and Technology*, *47*(8). https://doi.org/10.1021/es305026x

Tetzlaff, D., Birkel, C., Dick, J., Geris, J., & Soulsby, C. (2014). Storage dynamics in hydropedological units control hillslope connectivity, runoff generation, and the evolution of catchment transit time distributions. *Water Resources Research*, *50*(2). https://doi.org/10.1002/2013WR014147

Tilman, D. (1998). The greening of the green revolution. In *Nature* (Vol. 396, Issue 6708). https://doi.org/10.1038/24254

Tournebize, J., Chaumont, C., & Mander, Ü. (2017). Implications for constructed wetlands to mitigate nitrate and pesticide pollution in agricultural drained watersheds. *Ecological Engineering*, *103*. https://doi.org/10.1016/j.ecoleng.2016.02.014

United States Department of Agriculture. (1953). *Primary Characterization Data*.

United States Department of Agriculture (USDA) National Agricultural Statistics Service (NASS). (2023, January 30). *2022 Montana Cropland Data Layer | USDA NASS*. USDA NASS Marketing and Information Services Office, Washington, D.C.

USDA. (n.d.). *Focus on Croplands in the Northern Plains*. Northern Plains Climate Hub.

USDA. (2025, February 20). *https://nassgeodata.gmu.edu/CropScape/*.

USDA NRCS. (n.d.). *Soil Texture Calculator*. Retrieved March 8, 2025, from https://www.nrcs.usda.gov/resources/education-and-teaching-materials/soil-texture-calculator

USDA NRCS. (2021). Web Soil Survey. In *Natural Resources Conservation Service, United States Department of Agriculture*.

Verchot, L. V., Franklin, E. C., & Gilliam, J. W. (1997). Nitrogen Cycling in Piedmont Vegetated Filter Zones: II. Subsurface Nitrate Removal. *Journal of Environmental Quality*, *26*(2). https://doi.org/10.2134/jeq1997.00472425002600020003x

Vidon, P., Allan, C., Burns, D., Duval, T. P., Gurwick, N., Inamdar, S., Lowrance, R., Okay, J., Scott, D., & Sebestyen, S. (2010). Hot spots and hot moments in riparian zones: Potential for improved water quality management. *Journal of the American Water Resources Association*, *46*(2). https://doi.org/10.1111/j.1752-1688.2010.00420.x

Vidon, P. G. F., & Hill, A. R. (2004). Landscape controls on the hydrology of stream riparian zones. *Journal of Hydrology*, *292*(1–4). https://doi.org/10.1016/j.jhydrol.2004.01.005

Vidon, P. G., & Hill, A. R. (2006). A landscape-based approach to estimate riparian hydrological and nitrate removal functions. *Journal of the American Water Resources Association*, *42*(4). https://doi.org/10.1111/j.1752-1688.2006.tb04516.x

Vuke, S. M., Berg, R. B., Colton, R. B., & O'brien, H. E. (2002). *GEOLOGIC MAP OF THE BELT 30'x 60' QUADRANGLE, CENTRAL MONTANA*.

Wagner, F. M., Möller, M., Schmidt-Hattenberger, C., Kempka, T., & Maurer, H. (2013). Monitoring freshwater salinization in analog transport models by time-lapse electrical

resistivity tomography. *Journal of Applied Geophysics*, *89*. https://doi.org/10.1016/j.jappgeo.2012.11.013

Wald, J. A., Graham, R. C., & Schoeneberger, P. J. (2013). Distribution and properties of soft weathered bedrock at ≤ 1m depth in the contiguous United States. *Earth Surface Processes and Landforms*, *38*(6). https://doi.org/10.1002/esp.3343

Ward, A. S., Gooseff, M. N., & Singha, K. (2010a). Characterizing hyporheic transport processes - Interpretation of electrical geophysical data in coupled stream-hyporheic zone systems during solute tracer studies. *Advances in Water Resources*, *33*(11). https://doi.org/10.1016/j.advwatres.2010.05.008

Ward, A. S., Gooseff, M. N., & Singha, K. (2010b). Imaging hyporheic zone solute transport using electrical resistivity. *Hydrological Processes*, *24*(7). https://doi.org/10.1002/hyp.7672

Warwick, J., & Hill, A. R. (1988). Nitrate depletion in the riparian zone of a small woodland stream. *Hydrobiologia*, *157*(3). https://doi.org/10.1007/BF00004200

West, A. G., Patrickson, S. J., & Ehleringer, J. R. (2006). Water extraction times for plant and soil materials used in stable isotope analysis. *Rapid Communications in Mass Spectrometry*, *20*(8). https://doi.org/10.1002/rcm.2456

Whitlock, C., Cross, W. F., Maxwell, B., Silverman, N., & Wade, A. A. (2017). 2017 Montana Climate Assessment. In *Bozeman and Missoula MT: Montana State University and University of Montana, Montana Institute on Ecosystems*.

Willems, H. P. L., Rotelli, M. D., Berry, D. F., Smith, E. P., Reneau, R. B., & Mostaghimi, S. (1997). Nitrate removal in riparian wetland soils: Effects of flow rate, temperature, nitrate

concentration and soil depth. *Water Research*, *31*(4). https://doi.org/10.1016/S0043-1354(96)00315-6

Williams, J. D. (2004). Effects of long-term winter wheat, summer fallow residue and nutrient management on field hydrology for a silt loam in north-central Oregon. *Soil and Tillage Research*, *75*(2). https://doi.org/10.1016/j.still.2003.08.010

Zimmermann, U., Ehhalt, D., & Münnich, K. O. (1967). Soil-water movement and evapotranspiration: Changes in the isotopic composition of the water. *Symposium on Isotopes in Hydrology*, *I*.

APPENDICES

APPENDIX A

CHAPTER TWO: PHYSICAL PARAMETERS OF RIPARIAN WELLS

Table 2.S1: Physical well parameters and locations for all riparian well sites within the Louse Creek stream corridor.

Well	Longitude	Latitude	Screened interval (cm)[1]	Total depth (cm)[2]
RW01	-109.96608	47.06719	44.7 - 76.7	76.7
RW02	-109.96417	47.06806	43.0 – 73.0	73
RW03	-109.96398	47.06781	46.6 - 76.6	76.6
RW04	-109.9605	47.06895	33.7 - 65.7	65.7
RW05	-109.95995	47.06951	23.4 - 55.4	55.4
RW06	-109.96325	47.06819	0.8 - 53.8	53.8
RW07	-109.96153	47.06911	24.0 – 77.0	77
RW08	-109.96401	47.06818	11.5 - 64.5	64.5
RW09	-109.96081	47.06953	11.0 – 64.0	64
RW10	-109.96073	47.06872	27.0 – 80.0	80
RW11	-109.96412	47.068	56.9 - 106.9	106.9
RW12	-109.96412	47.06801	16.7 - 66.7	66.7
RW13	-109.96412	47.068	46.9 - 96.9	96.9
RW14	-109.96412	47.068	46.1 - 96.1	96.1
RW15	-109.96411	47.068	60.3 - 110.3	110.3
RW16	-109.9641	47.06801	61.5 - 111.5	111.5

[1] Centimeters below ground surface
[2] Total depth below ground surface

APPENDIX B

CHAPTER TWO: RIPARIAN WELL SUBSURFACE RESISTIVITY VALUES AND K-MEANS CLUSTERING

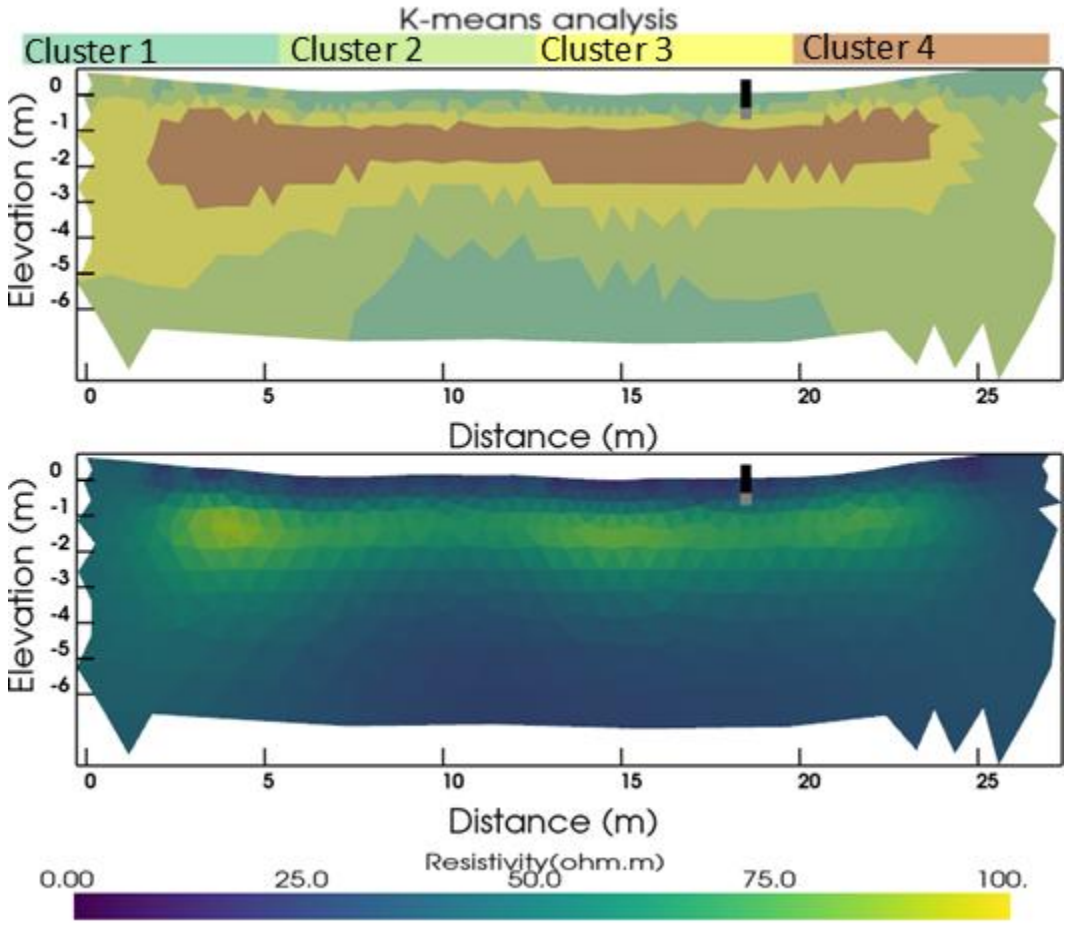


Figure 2.S1: Raw subsurface resistivity values (bottom) and K-means clustering results (top) at riparian well RW01 within the Louse Creek stream corridor. Image traverses a well (black vertical bar), with the well screen presented (grey vertical bar).

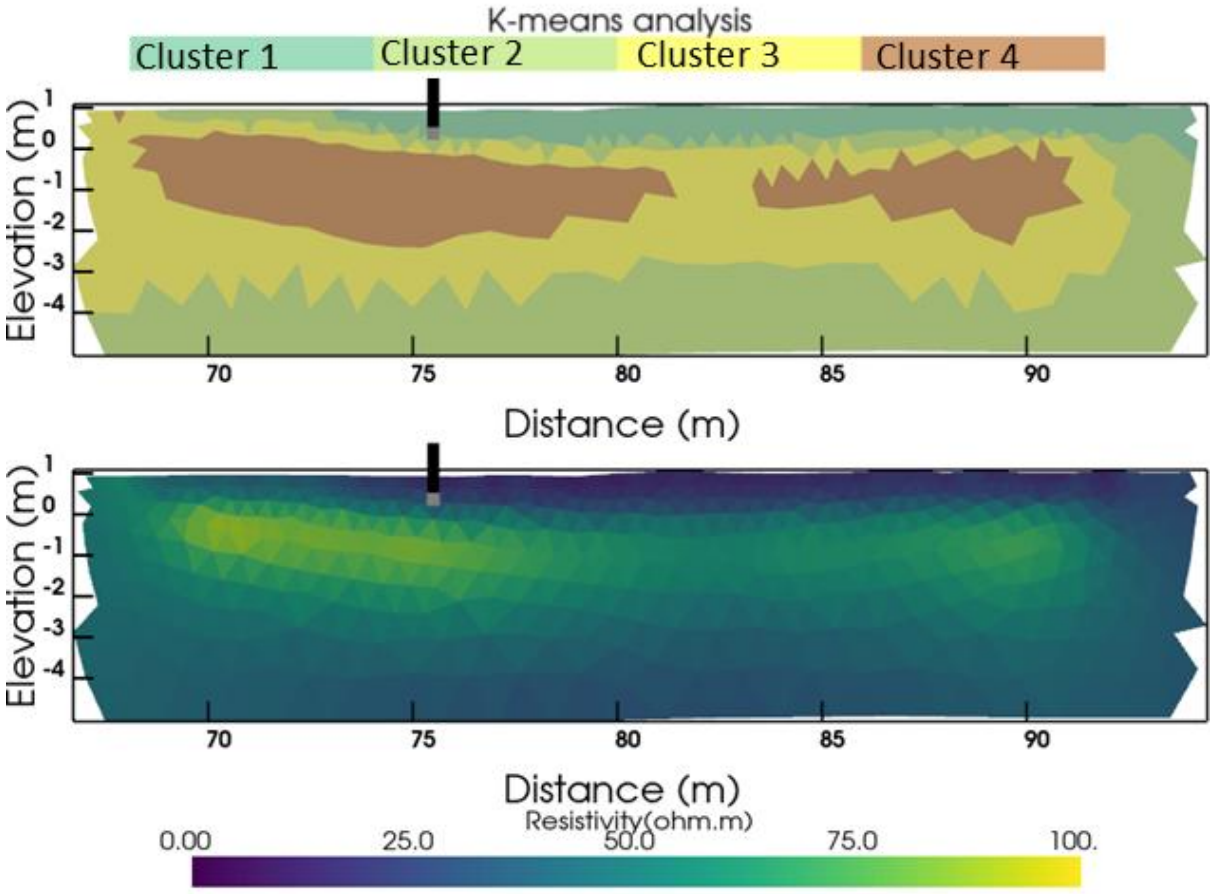


Figure 2.S2: Raw subsurface resistivity values (bottom) and K-means clustering results (top) at riparian well RW02 within the Louse Creek stream corridor. Image traverses a well (black vertical bar), with the well screen presented (grey vertical bar).

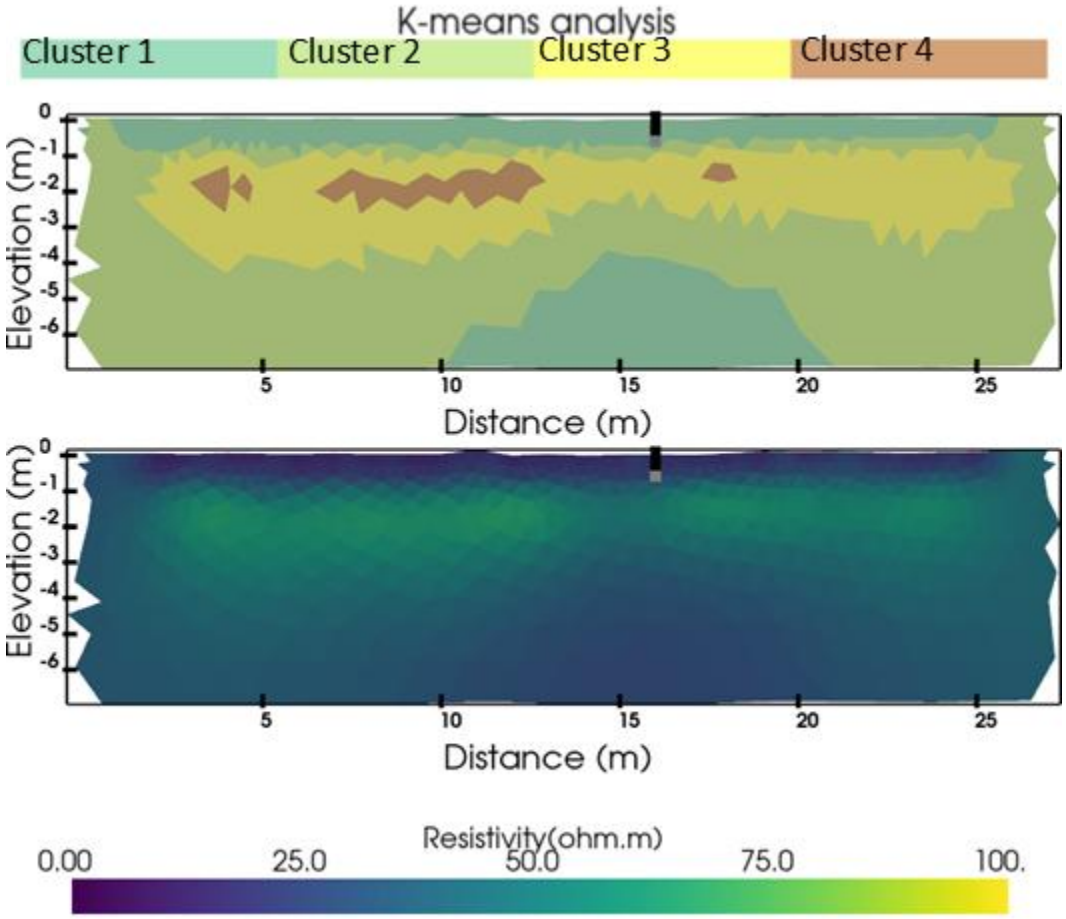


Figure 2.S3: Raw subsurface resistivity values (bottom) and K-means clustering results (top) at riparian well RW03 within the Louse Creek stream corridor. Image traverses a well (black vertical bar), with the well screen presented (grey vertical bar).

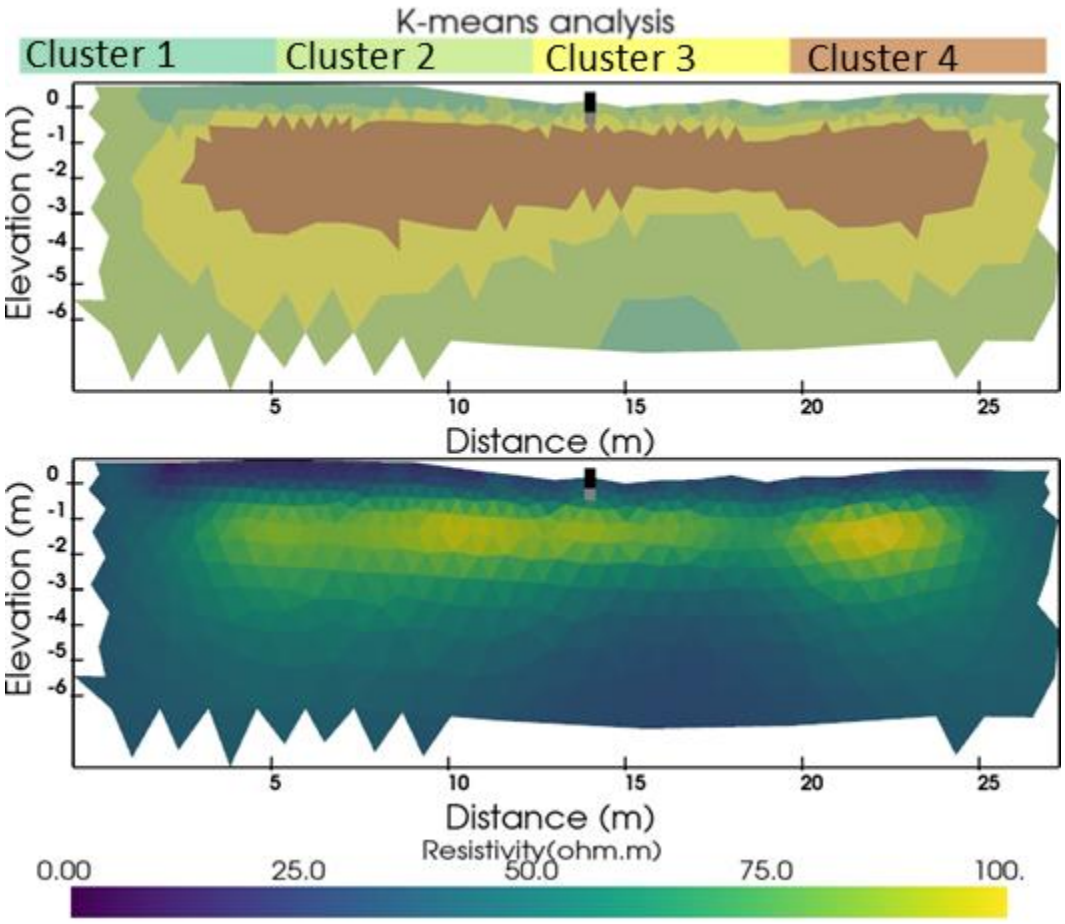


Figure 2.S4: Raw subsurface resistivity values (bottom) and K-means clustering results (top) at riparian well RW04 within the Louse Creek stream corridor. Image traverses a well (black vertical bar), with the well screen presented (grey vertical bar).

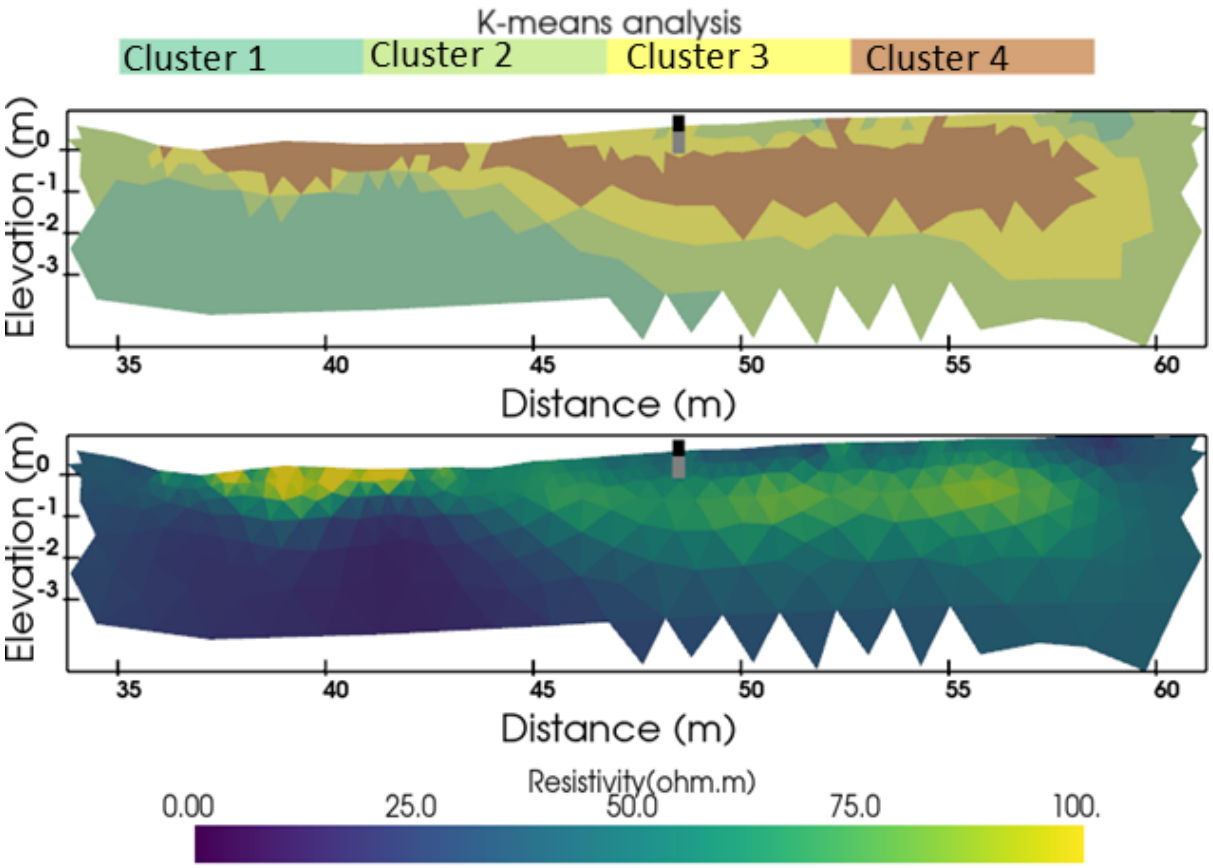


Figure 2.S5: Raw subsurface resistivity values (bottom) and K-means clustering results (top) at riparian well RW08 within the Louse Creek stream corridor. Image traverses a well (black vertical bar), with the well screen presented (grey vertical bar).

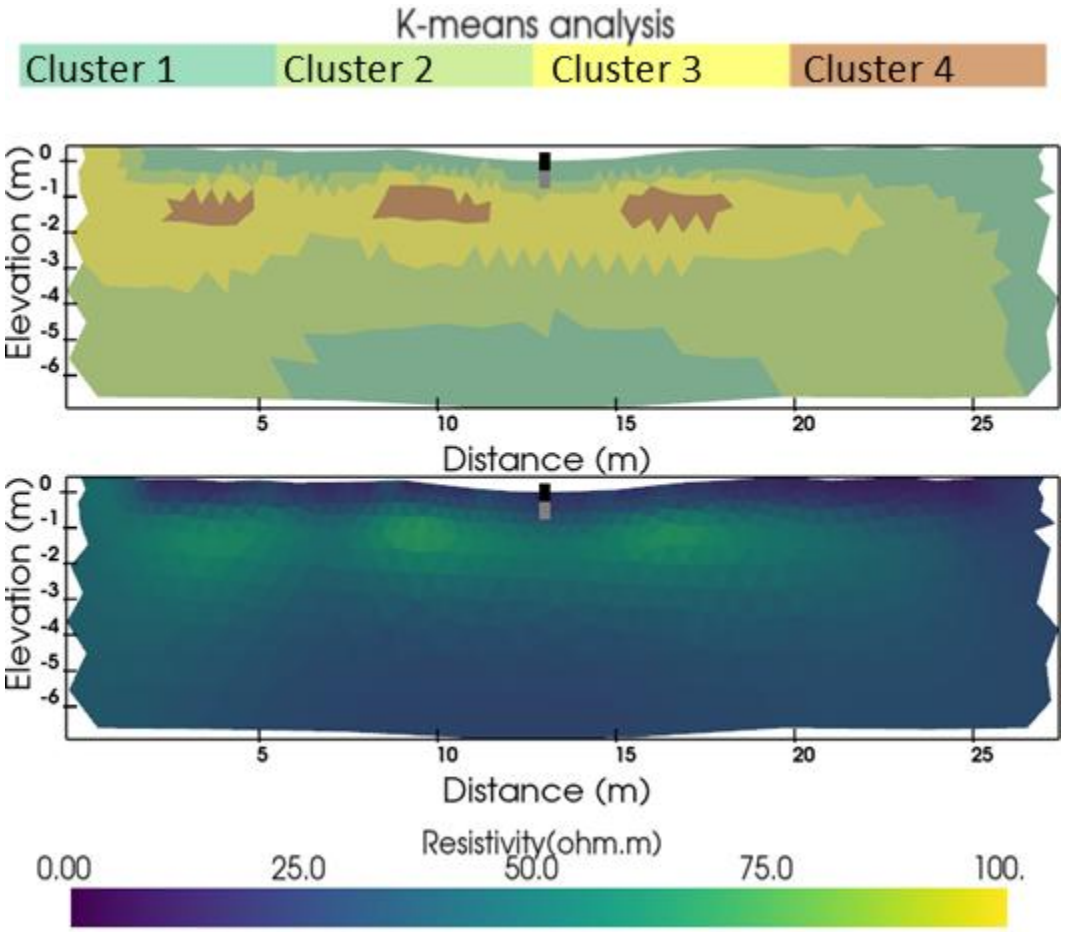


Figure 2.S6: Raw subsurface resistivity values (bottom) and K-means clustering results (top) at riparian well RW10 within the Louse Creek stream corridor. Image traverses a well (black vertical bar), with the well screen presented (grey vertical bar).

APPENDIX C

CHAPTER TWO: RIPARIAN WELLS NITRATE VALUES

Table 2.S2: All individual nitrate values (NO_3-N mg L^{-1}) and associated uncertainty (NO_3-N mg L^{-1}) presented in chapter two of this thesis.

Well	Value (NO_3-N mg L^{-1})	Uncertainty (NO_3-N mg L^{-1})	flag	Date
RW01	4.60	0.230	ok	4/19/2022
RW01	2.66	0.133	ok	6/10/2022
RW01	2.69	0.134	ok	8/1/2022
RW01	1.79	0.089	ok	10/6/2022
RW01	7.81	0.390	ok	12/6/2023
RW01	8.66	0.433	ok	3/19/2024
RW01	8.26	0.413	ok	4/2/2024
RW01	6.65	0.332	ok	5/13/2024
RW01	6.27	0.314	ok	5/28/2024
RW01	6.17	0.308	ok	6/11/2024
RW01	6.36	0.318	ok	6/21/2024
RW01	5.94	0.297	ok	7/26/2024
RW01	7.42	0.371	ok	8/29/2024
RW01	8.59	0.429	ok	10/24/2024
RW02	0.00	0.009	bdl	4/7/2021
RW02	0.00	0.048	bdl	6/3/2021
RW02	0.00	0.024	bdl	6/16/2021
RW02	0.02	0.002	bql	4/21/2021
RW02	0.00	0.008	bdl	5/1/2021
RW02	0.00	0.008	bdl	5/18/2021
RW02	0.00	0.010	bdl	4/19/2022
RW03	2.03	0.101	ok	4/7/2021
RW03	0.35	0.018	ok	6/3/2021
RW03	0.11	0.006	ok	6/17/2021
RW03	1.55	0.078	ok	4/21/2021

Well	Value (NO_3-N mg L^{-1})	Uncertainty (NO_3-N mg L^{-1})	flag	Date
RW04	0.42	0.021	ok	8/30/2021
RW04	5.92	0.296	ok	4/7/2021
RW04	2.50	0.125	ok	6/3/2021
RW04	1.89	0.095	ok	6/16/2021
RW04	1.46	0.073	ok	6/24/2021
RW04	1.39	0.070	ok	7/13/2021
RW04	5.54	0.277	ok	4/21/2021
RW04	5.14	0.257	ok	5/1/2021
RW04	3.66	0.183	ok	5/18/2021
RW04	1.90	0.095	ok	4/18/2022
RW04	2.17	0.108	ok	4/19/2022
RW04	0.34	0.017	ok	6/6/2022
RW04	0.00	0.059	bdl	8/1/2022
RW04	0.02	0.002	bql	10/6/2022
RW04	0.00	0.171	bdl	12/6/2023
RW04	1.53	0.077	ok	3/19/2024
RW04	1.39	0.070	ok	4/2/2024
RW04	0.83	0.042	ok	5/13/2024
RW04	0.18	0.018	bql	5/28/2024
RW04	0.00	0.171	bdl	6/11/2024
RW04	0.98	0.049	ok	6/21/2024
RW04	0.00	0.171	bdl	7/26/2024
RW04	0.07	0.007	bql	8/29/2024
RW04	0.23	0.011	ok	10/24/2024
RW05	0.01	0.001	bql	4/8/2021
RW05	0.00	0.048	bdl	6/3/2021
RW05	0.06	0.006	bql	4/21/2021

Well	Value (NO_3-N mg L^{-1})	Uncertainty (NO_3-N mg L^{-1})	flag	Date
RW05	0.00	0.020	bdl	6/10/2022
RW06	0.40	0.020	ok	4/7/2021
RW06	0.18	0.009	ok	6/3/2021
RW06	1.28	0.064	ok	6/16/2021
RW06	1.08	0.054	ok	6/24/2021
RW06	0.14	0.007	ok	4/21/2021
RW06	0.07	0.003	ok	5/1/2021
RW06	0.03	0.003	bql	5/18/2021
RW06	0.03	0.003	bql	6/10/2022
RW07	0.05	0.005	bql	4/8/2021
RW07	0.00	0.048	bdl	6/3/2021
RW07	0.00	0.024	bdl	6/16/2021
RW07	0.00	0.010	bdl	6/24/2021
RW07	0.00	0.016	bdl	7/13/2021
RW07	0.00	0.011	bdl	4/21/2021
RW07	0.00	0.020	bdl	6/10/2022
RW08	1.11	0.056	ok	8/30/2021
RW08	4.59	0.229	ok	3/26/2021
RW08	5.05	0.253	ok	4/7/2021
RW08	3.23	0.162	ok	6/3/2021
RW08	0.03	0.003	bql	6/16/2021
RW08	2.61	0.130	ok	6/24/2021
RW08	2.17	0.108	ok	7/13/2021
RW08	4.93	0.246	ok	4/21/2021
RW08	4.28	0.214	ok	5/1/2021
RW08	4.22	0.211	ok	5/18/2021
RW08	2.04	0.102	ok	4/18/2022

Well	Value (NO_3-N mg L^{-1})	Uncertainty (NO_3-N mg L^{-1})	flag	Date
RW08	2.18	0.109	ok	4/19/2022
RW08	1.14	0.057	ok	6/6/2022
RW08	2.39	0.119	ok	10/6/2022
RW08	4.74	0.237	ok	12/6/2023
RW08	6.01	0.301	ok	3/19/2024
RW08	5.55	0.278	ok	4/2/2024
RW08	4.35	0.218	ok	5/13/2024
RW08	2.60	0.130	ok	5/28/2024
RW08	2.84	0.142	ok	6/11/2024
RW08	3.88	0.194	ok	6/20/2024
RW08	2.11	0.106	ok	7/26/2024
RW08	1.82	0.091	ok	8/29/2024
RW09	0.07	0.007	bql	4/8/2021
RW09	0.00	0.048	bdl	6/3/2021
RW09	0.00	0.024	bdl	6/16/2021
RW09	0.00	0.010	bdl	6/24/2021
RW09	0.04	0.004	bql	7/13/2021
RW09	0.02	0.002	bql	4/21/2021
RW09	0.00	0.020	bdl	6/10/2022
RW10	0.00	0.009	bdl	4/8/2021
RW10	0.00	0.048	bdl	6/2/2021
RW10	2.57	0.129	ok	6/17/2021
RW10	0.00	0.010	bdl	6/24/2021
RW10	0.00	0.016	bdl	7/13/2021
RW10	0.00	0.011	bdl	4/21/2021
RW10	0.00	0.020	bdl	6/11/2022
RW11	2.74	0.137	ok	5/27/2024

Well	Value (NO_3-N mg L^{-1})	Uncertainty (NO_3-N mg L^{-1})	flag	Date
RW12	2.02	0.101	ok	5/27/2024
RW13	3.17	0.158	ok	5/27/2024
RW14	3.62	0.181	ok	5/27/2024
RW16	2.61	0.131	ok	5/30/2024
RW16	2.08	0.104	ok	5/31/2024

APPENDIX D

CHAPTER TWO: CONVERTING ERT IMAGES TO NACL CONCENTRATIONS

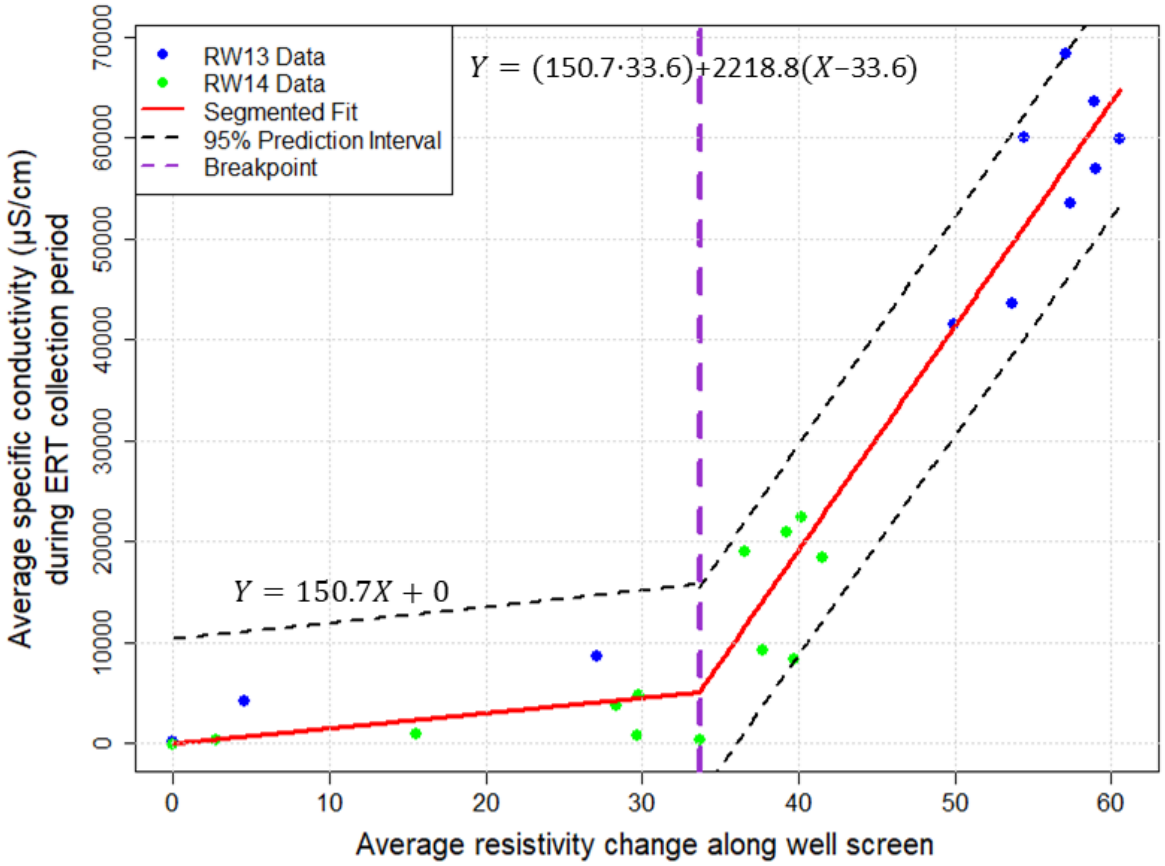


Figure 2.S7: Piecewise segmented relationship between bulk resistivity percent change and specific conductivity (µS cm^{-1}), measured at RW13 and RW14. Resistivity change values are presented in absolute value and are the average value from ERT cells along the well screen (RW13, RW14), and the specific conductivity (µS cm^{-1}) value is the average value, at each well, during the ERT collection period. The piecewise relationship breakpoint occurs at 33.6 average resistivity change (purple dashed line).

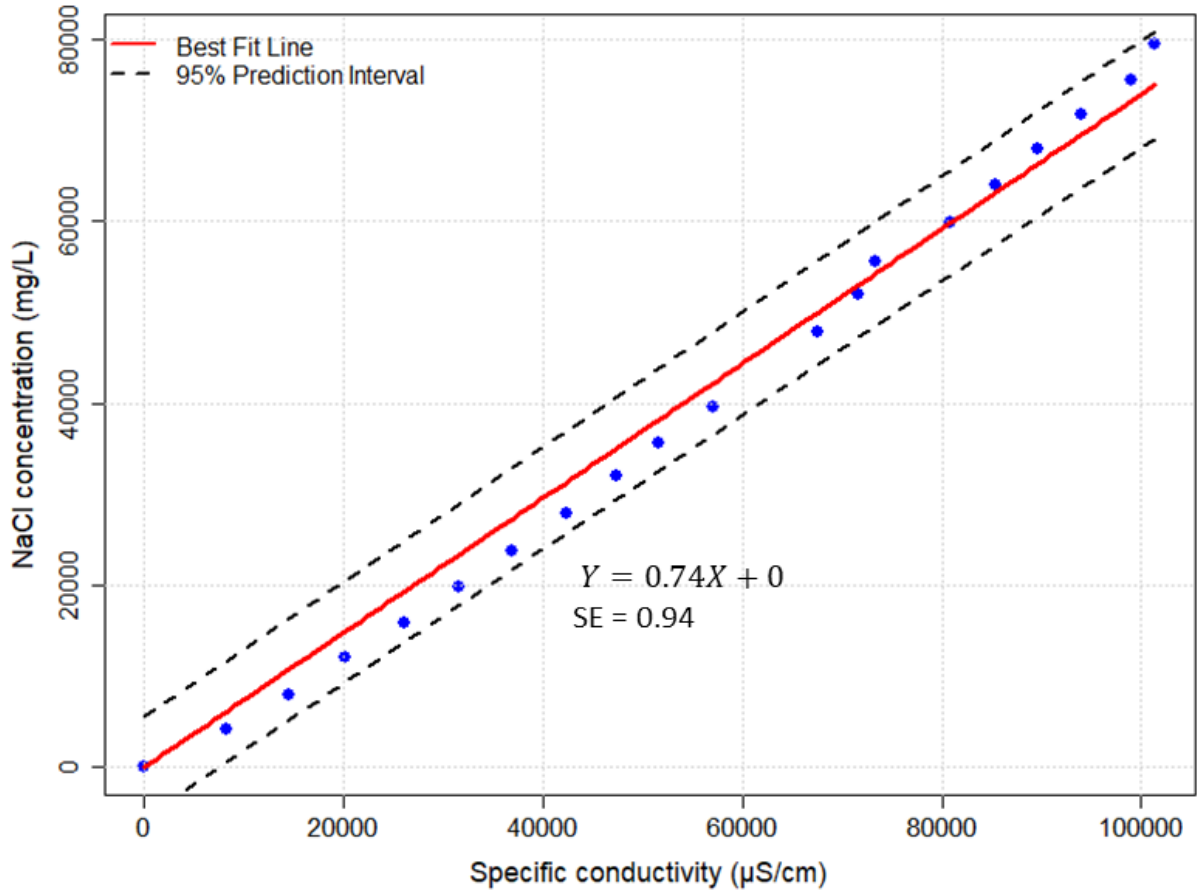


Figure 2.S8: Linear relationship between specific conductivity (µS cm^{-1}) and NaCl concentration (mg L^{-1}). One calibration point was removed due to inaccurate NaCl concentration recording.

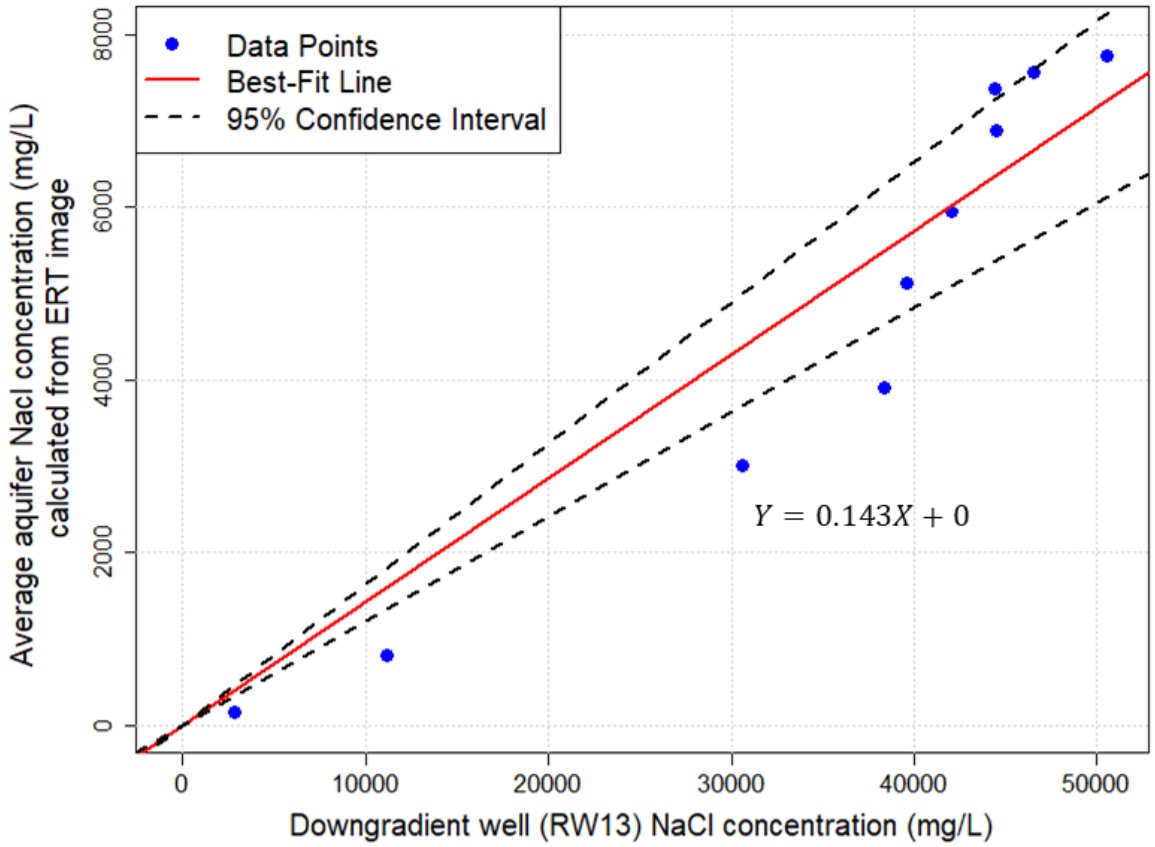


Figure 2.S9: Linear relationship between average aquifer NaCl concentration, derived from ERT images, and the NaCl observed from the specific conductivity recording at RW13. This relationship is used to convert our continuous specific conductivity (µS cm^{-1}) readings at RW13 to an average aquifer concentration. 95% confidence interval encompasses the propagated uncertainty associated with converting from percent change in resistivity, from ERT images (Figure 2.S7) to a specific conductivity (µS cm^{-1}), and then from a specific conductivity (µS cm^{-1}) to a NaCl concentration (mg L^{-1}) (Figure 2.S8). Confidence interval derived using Monte Carlo uncertainty propagation.

APPENDIX E

CHAPTER THREE: ASSESSMENT OF LIDAR DERIVED SNOW DEPTH COMPARED TO MANUALLY OBSERVED MEASUREMENTS

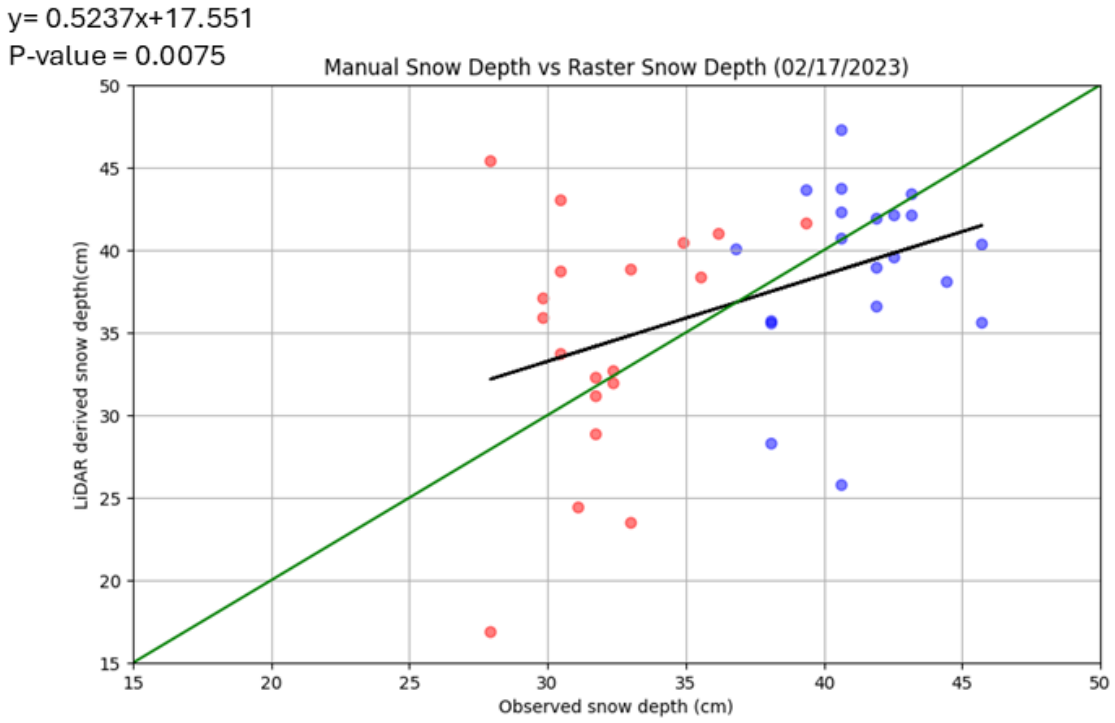


Figure 3.S1: Assessment of corrected LiDAR derived snow depth to on ground measured values, on 17 February 2023. Average difference between the observed snow depth samples and LiDAR derived snow depth was 4.6 cm, favoring higher snow depths in the manually observed points. This correction value was applied to all LiDAR derived snow depths. Red points indicate snow depth in short stubble plots and blue in tall stubble. Black line represents best fit and green line is 1:1.

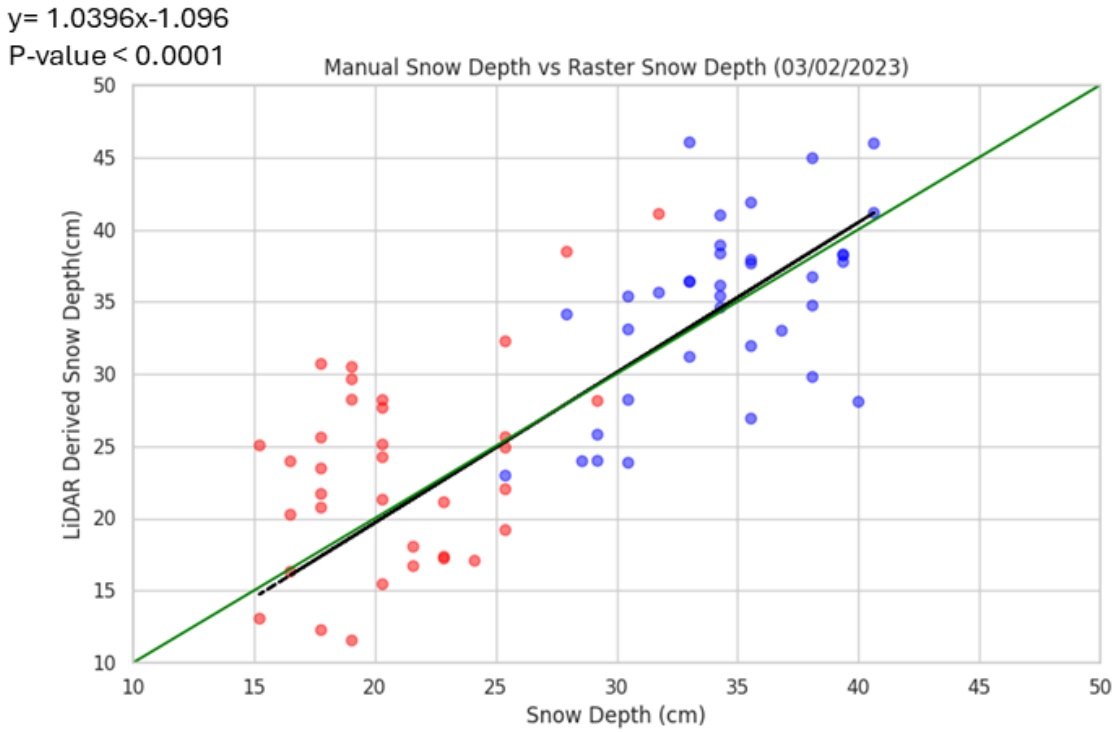


Figure 3.S2: Assessment of corrected LiDAR derived snow depth to on ground measured values, on 2 March 2023. Average difference between the observed snow depth samples and LiDAR derived snow depth was 8.8 cm, favoring higher snow depths in the manually observed points. This correction value was applied to all LiDAR derived snow depths. Red points indicate snow depth in short stubble plots and blue in tall stubble. Black line represents best fit and green line is 1:1.

APPENDIX F

CHAPTER THREE: SPATIAL DISTRIBUTION OF LIDAR DERIVED SNOW DEPTH AND SWE OBSERVATIONS

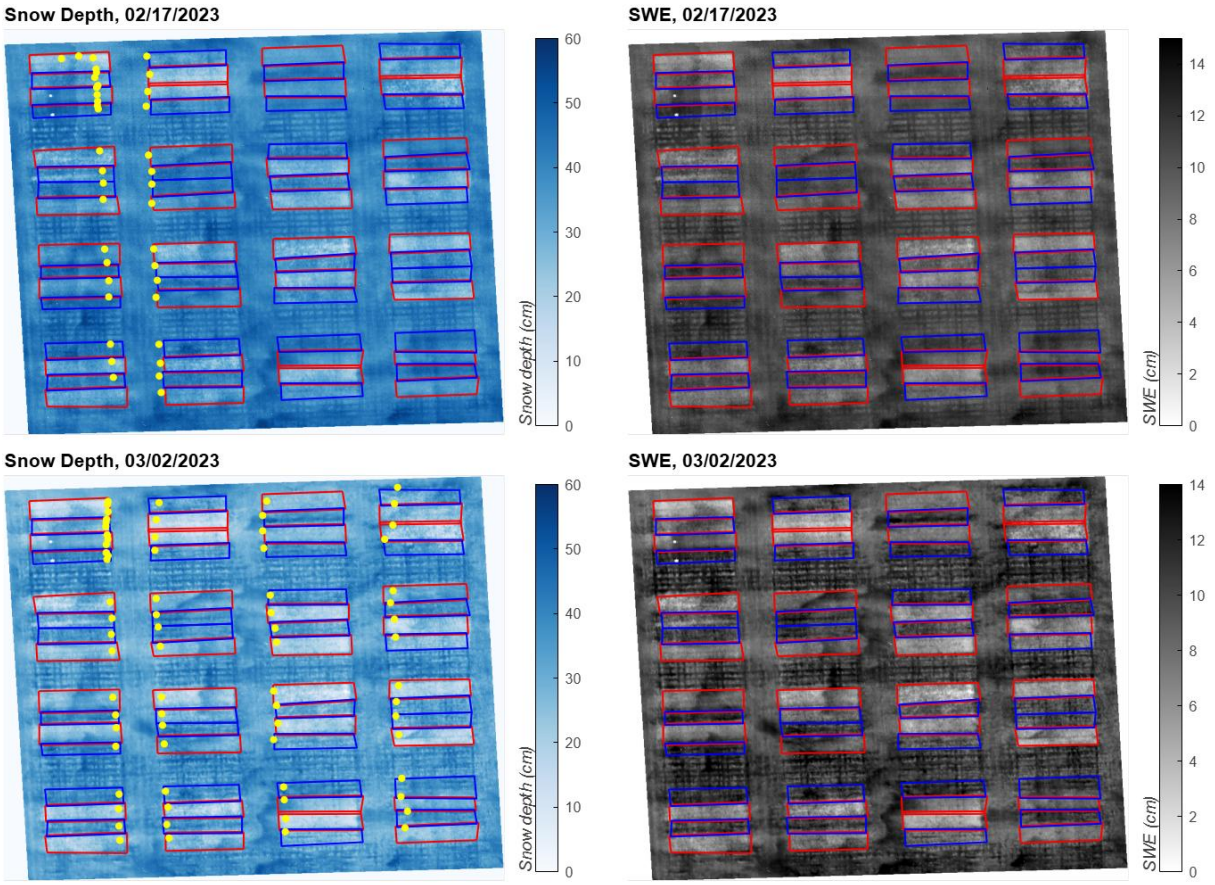


Figure 3.S3: Spatial distribution of LiDAR derived snow depth and SWE values, recorded at the Bozeman study site, during the winter of 2022-2023. Red polygons indicate short stubble and blue tall stubble plots. Yellow points in snow depth plots reflect manual observations of snow depth, recorded within 24-hr of flights.

APPENDIX G

CHAPTER THREE: MOCCASIN SOIL TEXTURE

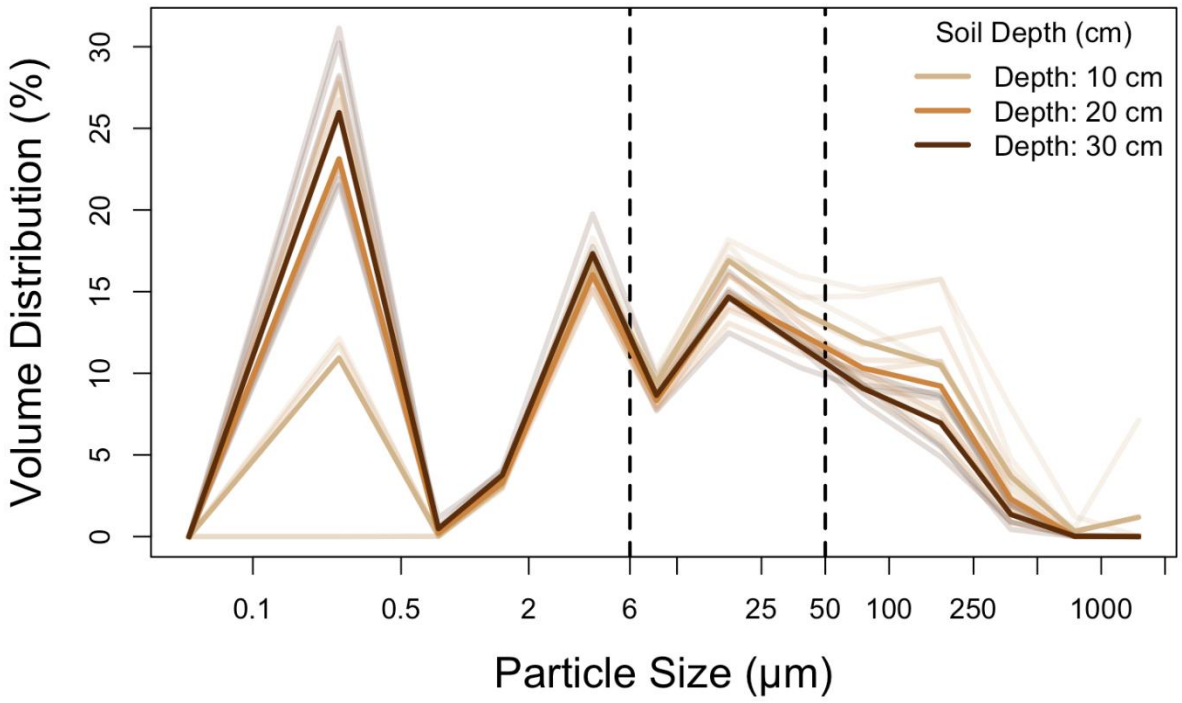


Figure 3.S4: Soil particle size analysis of soils at depth interval of 10, 20, and 30cm at the study site. Each line represents an average of six different samples collected at each depth, plotted as transparent background lines. We classify clay as particles between the size of 0-6 µm, silt as 6-50 µm, and sand as 50-200 µm (Schaetzl & Thomson, 2015).

Table 3.S1: Particle size percentages of clay, silt, and sand at each soil depth interval. Total percentages may not add up to 100% due to small number of particles not being classified by the machine. Soil texture class based on USDA standard practices(USDA NRCS, n.d.).

Soil Depth (cm)	**n**	**Clay (%)**	**Clay (SD%)**	**Silt (%)**	**Silt (SD%)**	**Sand (%)**	**Sand (SD%)**	**Soil Textural Class**
10	6	30.9	12.7	40.2	3.0	27.6	9.3	Clay Loam
20	6	42.7	5.4	35.5	2.5	21.9	4.5	Clay
30	6	47.5	3.1	35.0	2.6	17.4	2.9	Clay

APPENDIX H

CHAPTER THREE: EXPERIMENTAL ANALYSIS OF CRYOGENIC EXTRACTION EFFICIENCIES

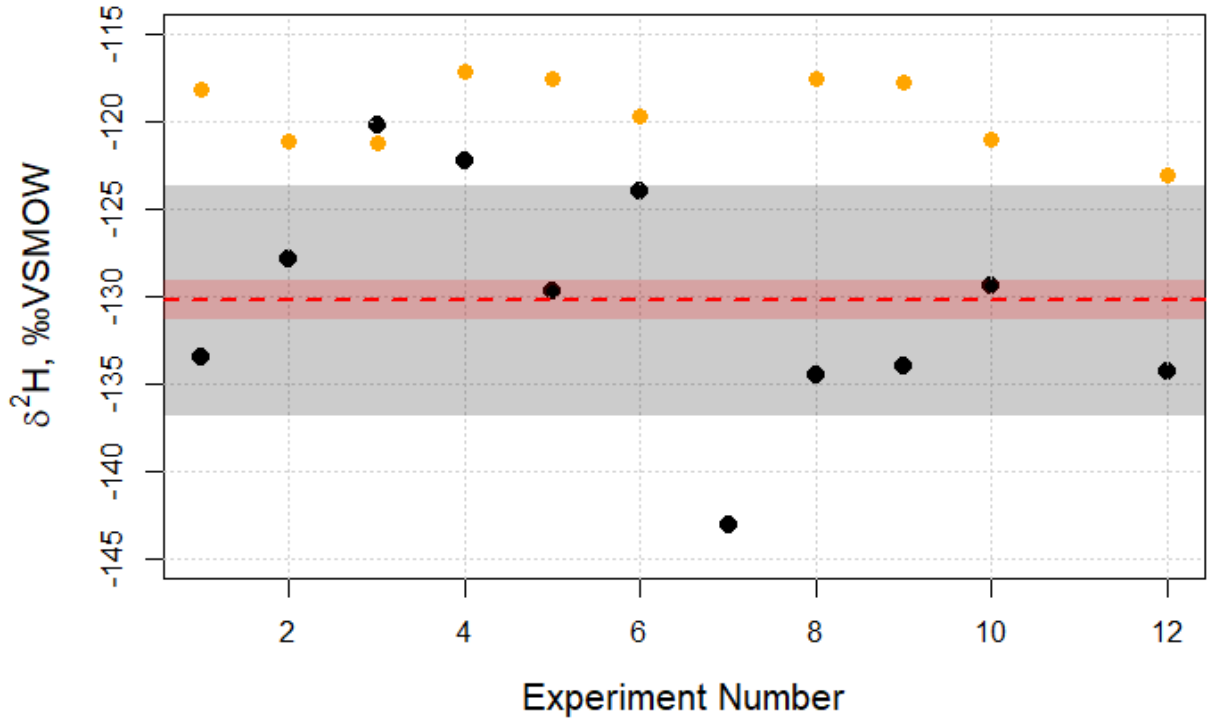


Figure 3.S5: Experimental analysis of spiked soil water. Black points reflect extracted soil water δ2H values (mean = -130.22) and the associated standard deviation (±6.60) (black shading). The red line represents the spiked soil waters known value (-130.15) and its associated analytical uncertainty (±1.12) (red shading). The known value of the spiked water was established over 31 observations, from 9 March 2024 to 7 March 2025, run amongst reported isotope values in this paper. Previously extracted waters isotopic composition for each soil sample is plotted in orange.

APPENDIX I

CHAPTER THREE: COMPARISON OF SOIL WATER LC EXCESS VALUES BETWEEN SHORT AND TALL STUBBLE AT THE END OF JUNE

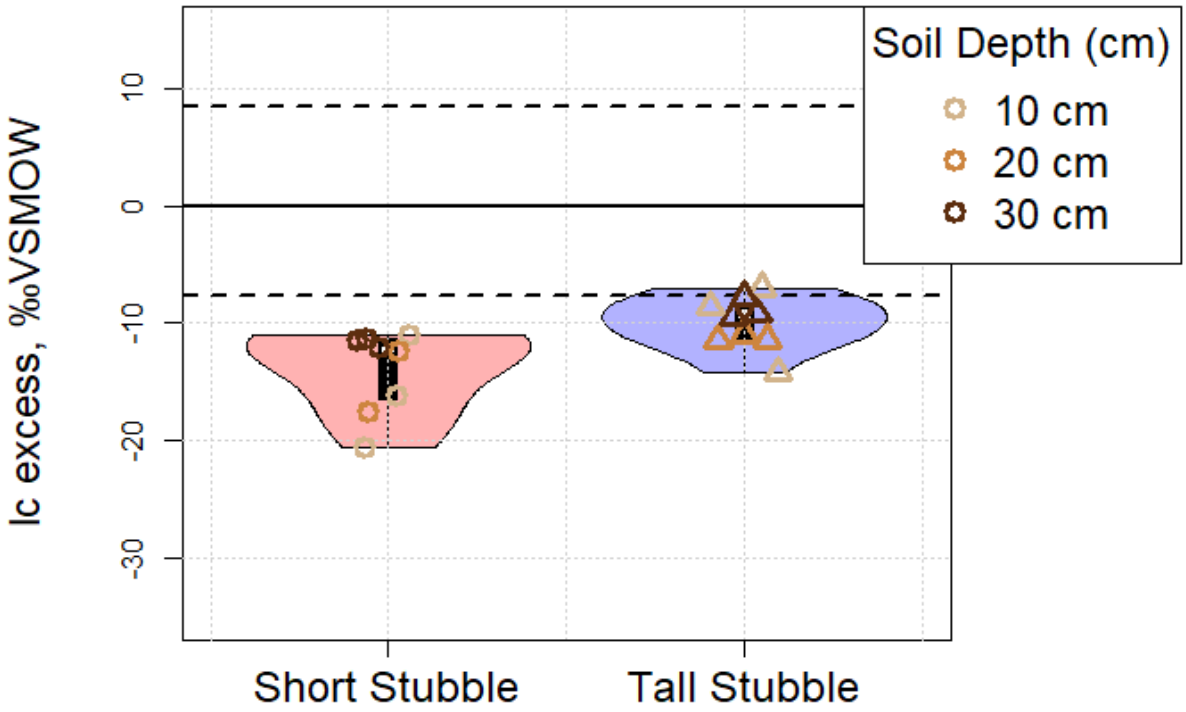


Figure 3.S6: Differences in lc excess values between short and tall stubble at all depth increments on 26 June 2024. We report high confidence that the mean lc excess value is different between short and tall stubble (t-test, p-value < 0.05). This is the only date with differences in lc excess values between the short and tall stubble across all depth increments.

APPENDIX J

CHAPTER THREE: SUMMARY STATISTICS OF SOIL WATER ISOTOPE VALUES

Table 3.S2: Summary statistics of soil water δ^2H, $\delta^{18}O$, and lc excess values. Summary statistics is grouped by collection date, then treatment type, and soil collection date.

Collection Date	Stubble Height	Depth (cm)	δ^2H				$\delta^{18}O$				lc excess				n
			Mean	SD	Min	Max	Mean	SD	Min	Max	Mean	SD	Min	Max	
1/23/2024	Short Stubble	10	-120.73	16.19	-139.31	-109.62	-15.94	1.89	-18.11	-14.65	3.45	4.21	0.37	8.25	3
		20	-107.19	18.74	-125.29	-87.88	-14.45	1.42	-15.95	-13.12	6.37	8.87	-1.04	16.20	3
		30	-103.14	10.64	-110.67	-95.62	-14.17	2.45	-15.89	-12.44	8.40	6.82	3.58	13.22	2
	Tall Stubble	10	-140.54	11.68	-153.78	-131.67	-18.20	1.77	-19.99	-16.45	-0.22	8.28	-8.29	8.26	3
		20	-95.58	12.73	-105.68	-81.28	-12.63	1.45	-13.60	-10.97	5.03	2.90	1.80	7.42	3
		30	-97.76	9.77	-105.60	-86.81	-12.61	1.09	-13.83	-11.72	2.65	9.02	-6.78	11.19	3
2/16/2024	Short Stubble	10	-133.01	10.59	-145.22	-126.27	-16.04	1.47	-17.71	-14.95	-8.08	1.21	-9.11	-6.75	3
		20	-117.33	13.13	-132.34	-107.94	-14.26	1.86	-16.41	-13.12	-5.09	1.41	-6.64	-3.87	3
		30	-105.03	2.41	-107.74	-103.13	-12.93	0.59	-13.30	-12.25	-2.33	3.25	-5.24	1.17	3
	Tall Stubble	10	-126.85	11.96	-140.52	-118.28	-14.85	2.00	-17.14	-13.45	-10.45	2.37	-11.85	-7.71	3
		20	-102.02	21.60	-124.66	-81.63	-11.60	3.31	-15.14	-8.57	-8.81	2.31	-10.26	-6.15	3
		30	-96.56	15.73	-114.38	-84.63	-11.35	2.72	-14.44	-9.30	-5.10	3.71	-7.81	-0.87	3
3/26/2024	Short Stubble	10	-118.55	4.57	-123.44	-114.41	-13.27	0.59	-13.94	-12.84	-13.43	1.06	-14.45	-12.34	3
		20	-106.96	9.14	-116.46	-98.22	-12.27	1.30	-13.52	-10.92	-8.92	1.32	-9.83	-7.40	3
		30	-101.84	15.67	-112.92	-90.76	-11.96	1.98	-13.36	-10.56	-6.05	1.52	-7.13	-4.97	2
	Tall Stubble	10	-134.34	13.15	-143.64	-125.04	-15.39	1.68	-16.58	-14.21	-14.02	1.17	-14.85	-13.20	2
		20	-122.94	9.26	-129.00	-112.28	-14.23	1.34	-15.07	-12.68	-10.96	1.27	-11.99	-9.54	3
		30	-105.12	20.91	-119.91	-90.34	-12.33	2.64	-14.19	-10.46	-6.72	2.09	-8.20	-5.23	2
4/5/2024		10	-124.04	5.19	-129.08	-118.72	-14.61	0.93	-15.59	-13.73	-9.34	1.68	-10.36	-7.40	3

Collection Date	Stubble Height	Depth (cm)	δ^2H				$\delta^{18}O$				lc excess				n
			Mean	SD	Min	Max	Mean	SD	Min	Max	Mean	SD	Min	Max	
	Short Stubble	20	-117.72	6.88	-124.03	-110.38	-14.07	1.15	-15.01	-12.79	-6.83	1.70	-8.67	-5.34	3
		30	-96.81	9.80	-105.67	-86.28	-11.98	1.26	-13.25	-10.72	-0.85	1.62	-2.55	0.68	3
	Tall Stubble	10	-129.23	7.93	-134.27	-120.10	-15.52	0.94	-16.16	-14.44	-8.00	1.70	-9.89	-6.59	3
		20	-118.76	15.55	-133.91	-102.85	-14.24	1.71	-15.80	-12.41	-6.69	3.59	-10.71	-3.83	3
		30	-110.41	5.76	-115.36	-104.09	-13.56	0.90	-14.26	-12.54	-3.18	0.98	-4.16	-2.21	3
4/14/2024	Short Stubble	10	-119.43	14.75	-134.73	-105.31	-12.87	2.10	-14.82	-10.65	-17.12	2.70	-18.83	-14.01	3
		20	-125.10	5.46	-131.31	-121.06	-14.22	0.93	-15.22	-13.37	-13.20	1.73	-15.19	-12.16	3
		30	-112.09	17.40	-131.69	-98.50	-13.34	2.14	-15.77	-11.75	-6.41	2.23	-8.68	-4.21	3
	Tall Stubble	10	-118.64	11.17	-129.30	-107.03	-13.04	2.10	-15.41	-11.40	-15.11	6.20	-21.26	-8.86	3
		20	-123.03	7.92	-129.84	-114.35	-13.87	0.68	-14.47	-13.14	-13.61	3.10	-16.13	-10.15	3
		30	-120.81	11.15	-132.27	-110.00	-13.94	1.21	-15.31	-13.05	-10.91	3.91	-13.73	-6.44	3
5/15/2024	Short Stubble	10	-121.44	16.04	-139.94	-111.46	-15.01	2.70	-18.03	-12.81	-3.87	4.94	-9.57	-0.83	3
		20	-123.13	0.70	-123.63	-122.64	-15.06	0.50	-15.42	-14.71	-5.18	2.86	-7.20	-3.16	2
		30	-119.85	8.83	-125.56	-109.68	-14.47	2.18	-15.80	-11.95	-6.13	6.86	-13.94	-1.07	3
	Tall Stubble	10	-120.85	7.30	-128.39	-113.82	-14.85	0.49	-15.38	-14.42	-4.40	3.84	-8.14	-0.47	3
		20	-133.13	26.11	-151.59	-114.67	-16.71	2.96	-18.80	-14.62	-3.45	5.01	-6.99	0.09	2
		30	-123.90	7.01	-128.86	-118.94	-14.80	0.89	-15.43	-14.17	-7.84	0.68	-8.32	-7.36	2
6/11/2024	Short Stubble	10	-89.43	7.53	-97.94	-83.60	-6.88	1.21	-8.24	-5.94	-29.95	1.09	-30.82	-28.72	3
		20	-109.95	6.98	-116.01	-102.32	-11.88	1.24	-12.97	-10.53	-14.69	1.90	-16.74	-12.98	3
		30	-121.50	2.56	-124.12	-119.00	-14.09	0.25	-14.28	-13.80	-10.53	1.06	-11.75	-9.78	3
		10	-96.88	5.40	-102.01	-91.24	-9.61	0.92	-10.60	-8.78	-17.89	1.83	-19.56	-15.93	3

Collection Date	Stubble Height	Depth (cm)	δ^2H				$\delta^{18}O$				lc excess				n
			Mean	SD	Min	Max	Mean	SD	Min	Max	Mean	SD	Min	Max	
	Tall Stubble	20	-108.23	6.11	-112.47	-101.22	-12.10	1.29	-13.58	-11.23	-11.43	6.73	-18.50	-5.11	3
		30	-116.30	19.20	-129.87	-102.72	-13.66	2.18	-15.20	-12.12	-8.37	3.63	-10.94	-5.81	2
6/26/2024	Short Stubble	10	-115.65	7.88	-122.01	-106.84	-12.51	1.44	-14.08	-11.24	-15.94	4.75	-20.58	-11.09	3
		20	-119.05	2.18	-120.59	-117.51	-13.12	0.82	-13.70	-12.54	-14.99	3.69	-17.60	-12.38	2
		30	-122.69	4.11	-126.05	-118.11	-14.10	0.63	-14.61	-13.40	-11.60	0.38	-12.05	-11.36	3
	Tall Stubble	10	-114.49	6.85	-119.61	-106.70	-13.18	0.85	-13.97	-12.29	-9.95	3.79	-14.24	-7.04	3
		20	-120.01	1.97	-121.21	-117.73	-13.77	0.29	-13.97	-13.44	-11.27	0.29	-11.48	-10.94	3
		30	-120.53	2.78	-123.06	-117.56	-14.19	0.27	-14.46	-13.92	-8.80	0.88	-9.40	-7.79	3

APPENDIX K

STATEMENT OF DATA AVAILABILITY

All data presented in this thesis is made publicly available at Hydroshare. Each data product is made up of four folders to make clear each data compilation process. The 01_input folder contains original result files. The 02_protocol contains coding language used to manipulate and compile the data. 03_incremental folder includes products not included in the final product. The 04_poduct folder contains the outcome of the workflow. Metadata information is included for each data product in an excel spreadsheet.

Data for chapter two was primarily analyzed by the Montana State Environmental Analytical Lab. Hydrological simulations were conducted using the Montana State University Tempest research cluster. The data have been compiled on Hydroshare (Poole & Ewing, 2025b). Chapter two link: https://www.hydroshare.org/resource/543c4c6793c5419fb472810e4a557558/

Data for chapter three was analyzed at the Montana State University Environmental Lab. All presented meteorological data was downloaded, and is publicly available, at the Montana Mesonet site. The data have been compiled on Hydroshare (Poole & Ewing, 2025a). Chapter three link: https://www.hydroshare.org/resource/91166359814f4b639c585723b8e5d965/